Use of relatively located microearthquakes to map fault patterns and estimate the thickness of the brittle crust in Southwest Iceland

Sigurlaug Hjaltadóttir

Use of relatively located microearthquakes to map fault patterns and estimate the thickness of the brittle crust in Southwest Iceland

Sigurlaug Hjaltadóttir

90 ECTS thesis submitted in partial fulfillment of a
Magister Scientiarum degree in Geophysics

Advisors
Kristín S. Vogfjörð,Icelandic Meteorological Office
Páll Einarsson, University of Iceland

Faculty Representative
Ingi Þorleifur Bjarnason

Faculty of Earth Sciences
School of Engineering and Natural Sciences
University of Iceland
Reykjavik, October 2009

Use of relatively located microearthquakes to map fault patterns and estimate the thickness of the brittle crust in Southwest Iceland
Sub-surface fault mapping in Southwest Iceland
90 ECTS thesis submitted in partial fulfilment of a *Magister Scientiarum* degree in Geophysics

Abstract

The two rift zones in southern Iceland, the western and the eastern volcanic zones, are connected by an approximately 70 km long and 15 km wide left lateral shear zone, the South Iceland seismic zone (SISZ). Approximately every 100 years a sequence of large earthquakes of magnitudes M 6-7 occurs in the zone and traces of many Holocene faults have been mapped on the surface. Although the trend of the zone is east-west, major earthquakes take place on north-south striking faults, which leads to "bookshelf" type faulting. In June 2000, two large earthquakes of magnitudes $M_L 6.4$ and $M_L 6.5$ struck in the SISZ, three and a half days and approximately 17 km apart. Seismicity greatly increased in all Southwest Iceland and during 2000, roughly nineteen thousand microearthquakes were recorded there. The aim of this research is to relocate the earthquakes using a double-difference relative location method and to map the faults that they occur on. Due to the high clock-accuracy of the Icelandic SIL seismic network, the method can, through cross-correlation, reduce the uncertainties in relative arrival times and thus increase relative location accuracy to as far as tens of meters. This enables fault mapping by grouping together relocated events that form apparent lineaments. A suite of possible mechanisms are calculated for each event based on polarities and spectral amplitudes. Through the joint interpretation of fault mechanisms with the event distribution defining the fault, the slip direction on the fault plane can be inferred. Using this kind of mapping, about 240 faults, fault segments and small clusters, which were active in year 2000, have been mapped during this research. A detailed image of the two large fault planes of the 17 June event (J17) and the 21 June event (J21) has been revealed. The aftershock activity on the 12.5 km long, 10 km wide, north-south striking, near vertical J17 fault is mainly confined to its margins and centre, and the fault is composed of three patches, each striking a few degrees east of the overall fault strike, which is N197°E. The J21 fault, on the other hand, is more linear but with varying dip. South of the epicentre the fault is vertical but north of it, dip changes to 77°. It is 15.5 km long, strikes N179°E and deepens to the south from 6 km to 9 km. Many other smaller faults in Southwest Iceland that were illuminated by the 2000 activity have also been mapped, including the fault planes of three M~5 events which were triggered within minutes of the J17 event. The depth distribution of the relocated seismicity shows shallower focal depths in geothermal areas. Generally the results indicate a 6-8 km thick brittle crust and abrupt thickening is observed between 20.8°W and 20.6°W in the central SISZ. The thickness of the brittle crust increases eastwards to 10 km near the 1912 Selsund fault, and southwards to 13 km south of the transform zone.

Útdráttur

Endurstaðsettir smáskjálftar frá 2000 notaðir til þess að kortleggja sprungufleti og meta þykkt brotgjörnu skorpunnar á Suðvesturlandi

Suðurlandsbrotabeltið er um 70 km langt og 15 km breitt þverbrotabelti sem tengir gliðnunarbeltin tvö á suðurhluta landsins, eystra og vestara gosbeltið. Á hér um bil 100 ára fresti gengur yfir röð stórra skjálfta af stærð M 6-7 í Suðurlandsbrotabeltinu og hafa yfirborðssprungur skjálfta á nútíma verið kortlagðar víða í brotabeltinu. Stefna þverbrotabeltisnis er A-V en þó sýnir yfirborðskortlagning, ásamt kortlögðum áhrifasvæðum, að sögulegir skjálftar hafi orðið á stórum N-S sprungum. Hefur aflögun á beltinu því verið lýst með svokallaðri bókahillutektónik, þar sem það brotnar upp í N-S blokkir sem aflagast eins og bækur í hillu sem renna lítið eitt til. Þann 17. júní 2000 reið yfir stór Suðurlandsskjálfti af stærð M_L 6,4 í Holtunum. Þremur og hálfum sólarhring síðar reið annar yfir af stærð M_L 6,5 sunnan Hestvatns. Í kjölfar skjálftanna jókst skjálftavirkni gríðarlega á öllu Suðvesturlandi og ríflega nítján þúsund skjálftar voru staðsettir þar fram til desemberloka sama ár. Marmið þessarar rannsóknar er að endurstaðsetja skjálftana með svokallaðri upptakagreiningu og að kortleggja þá sprungufleti sem þeir verða á. Upptakagreining byggir á þeirri staðreynd að bylgjuform tveggja skjálfta sem hafa ferðast nær sömu leið eru mjög lík og þá er hægt að nota víxlfylgniaðferð (*e. cross-correlation*) til þess að fá enn nákvæmari afstæðan komutíma skjálftanna. Þar af leiðandi er hægt að staðsetja nálæga skjálfta afstætt með mun meiri nákvæmni en ella. Hin aukna afstæða staðsetningarnákvæmni getur leitt í ljós þá sprungufleti sem skjálftarnir verða á. Þeir eru kortlagðir og hreyfistefna á þeim er metin með samtúlkun á brotlausnum skjálftanna og brotfletinum sem skjálftarnir verða á. Þessum aðferðum hefur nú verið beitt til þess að kortleggja nærri 240 sprungur, sprungubrot og þyrpingar sem voru virkar árið 2000. Sprungufletirnir tveir sem mynduðust 17. og 21. júní 2000 hafa m.a. verið kortlagðir. Holtasprungan er um 12,5 km löng, 10 km djúp, nær lóðrétt og með strikstefnu N197°A. Eftirskjálftavirknin raðast aðallega á jaðra hennar og í miðjuna og virðist sprungan vera gerð úr þremur skástígum bútum sem allir hafa strikstefnu aðeins austan við strik sprungunnar í heild, en þó er hún samhangandi við botninn. Hestvatnssprungan er einnig nær lóðrétt og um 15,5 km löng og með strikstefnu N179°A. Hún er ólík Holtasprungunni að því leyti að hún dýpkar til suðurs, úr 6 í 9 km en jafnframt virðist hún mynduð úr tveimur mishallandi flötum. Rétt sunnan skjálftamiðjunnar er sprungan nær lóðrétt (88° halli) en norðan upptakanna hallar henni um 77° til austurs. Fjöldamargar minni sprungur hafa einnig verið kortlagðar víða á Suðvesturlandi, þar á meðal brotfletir þriggja skjálfta af stærð um og yfir M_L 5 sem urðu innan nokkurra mínútna eftir stóra 17. júní skjálftann. Almennt bendir dýptardreifing skjálftanna til þess að brotgjarna skorpan sé 6-8 km þykk en hún þyknar þó verulega um miðbik brotabeltisins, eða á milli 20,8°V og 20,6°V. Austast í brotabeltinu er brotgjarna skorpan um 10 km þykk en sunnan brotabeltisins þyknar hún enn og er um 13 km þykk. Enn fremur sýnir rannsóknin að upptakadýpi skjálfta er áberandi grynnra á stærri jarðhitasvæðum.

Preface

The work published in this thesis was mostly carried out between 2003 and 2006. Although we have learnt a few more things since then, that could probably have improved the results, it was decided to leave them as they were processed originally, apart from a few minor changes. The main results have partly been published in two reports at Veðurstofan, Rit 21 (Hjaltadóttir and Vogfjörð, 2005) and report 05020 (Hjaltadóttir et al., 2005), but these reports are not nearly as extensive as the following text. The research has also been presented at several meetings, seminars and in the articles, that are listed in Appendix C.

Table of Contents

List of Figures

List of Tables

Abbreviations

CD	Characteristic depth
CFS	Coulomb failure stress
CMT	Centroid moment tensor
d	distance between group centres
DL	Dalvík lineament
EVZ	Eastern volcanic zone
fps	fault plane solution
GL	Grímsey lineament
GPS	Global Positioning System
HFF	Húsavík-Flatey fault
HM	Hreppar micro-plate
InSAR	Interferometric Synthetic Aperture Radar
J17	the 17 June large Holt earthquake
J21	the 21 June large Hestvatn earthquake
KR	Kolbeinsey Ridge
max48	maximum group size of 48 events
NVZ	Northern volcanic zone
r	group radius
RP	Reykjanes Peninsula
RR	Reykjanes Ridge
SIL	South Iceland Lowland; Iceland's national seismic network
SISZ	South Iceland seismic zone
TFZ	Tjörnes fracture zone
WVZ	Western volcanic zone
Δdist	residual of relative distance
δ	fault dip [°]
ϕ	fault strike [°]
λ	rake [°]
λ_{ave}	average rake [°]
λ_{wav}	weighted average rake [°](weighted with scalar moment)
μ	shear modulus [Pa]

Acknowledgements

1 Introduction

Iceland is situated on the mid-Atlantic plate boundary, between the Reykjanes ridge (RR) in the south and the Kolbeinsey ridge in the north. The plate boundary on the island is now expressed through four rift zones: The Reykjanes Peninsula (RP), which is the on-land continuation of the RR, the western volcanic zone (WVZ) which is a northward continuation of the RP rift zone, the eastern volcanic zone (EVZ) and the northern volcanic zone (NVZ) (Einarsson, 1991, 2008) (Figure 1.1). Two transform zones connect the above rift segments: the south Iceland seismic zone (SISZ) in southern Iceland, which connects the RP to the EVZ, and the Tjörnes fracture zone (TFZ), which connects the NVZ to the offshore Kolbeinsey ridge (KR). The block bounded by the WVZ, EVZ and SISZ is sometimes called the Hreppar micro-plate (HM). Seismicity is mainly confined to the two transform zones, the TFZ and the SISZ. This thesis focuses on seismicity in the SISZ, RP and WVZ.
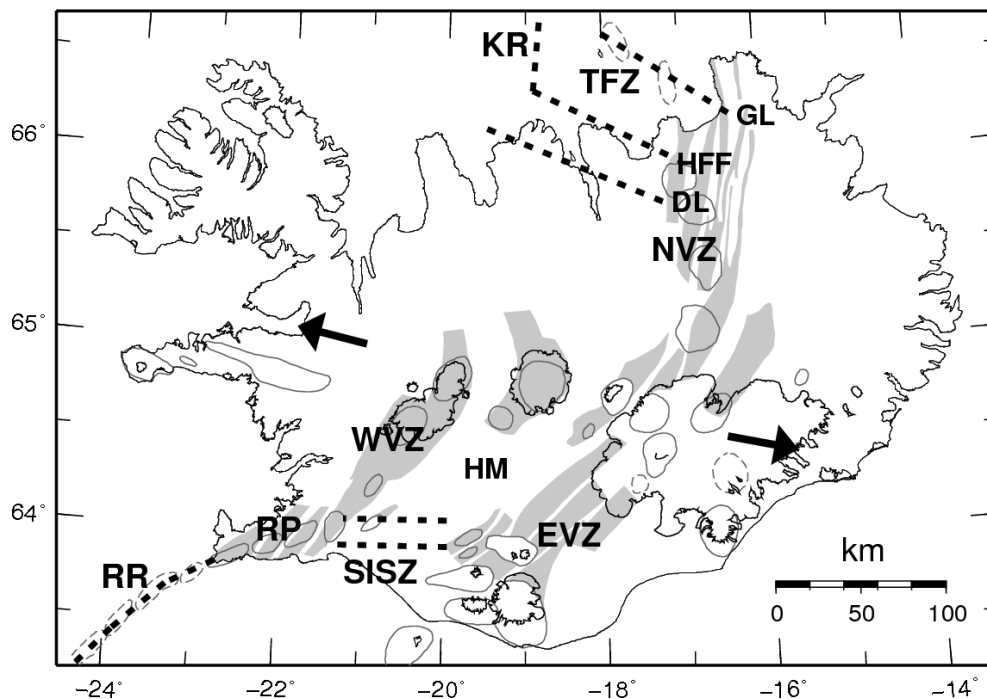
Figure 1.1. *The plate boundary in Iceland. Fissure swarms are shown as grey areas and central volcanoes outlined with black, thin lines (after Einarsson and Sæmundsson, 1987). The ridge segments offshore and the two transform zones are drawn as black broken lines. Abbreviations refer to main text. The Tjörnes fracture zone (TFZ) is composed of three lineaments: the Grímsey lineament (GL), the Húsavík-Flatey fault (HFF) and the less active Dalvík lineament (DL).*

Through centuries, large earthquakes have struck in the SISZ and caused damage to inhabited areas. Annals state that for the past 1000 years, at least 33 earthquakes have caused severe damage in the South Iceland lowland (SIL) (Einarsson et al., 1981). Based on this history, and that the last sequence of major earthquakes had occurred in 1896, Einarsson (1985) concluded that there was 80% probability that a major sequence would

recur in the next 25 years. By estimating strain release in historical earthquakes since 1700, Stefánsson and Halldórsson (1988) suggested that the next large earthquake in the SISZ would take place near to 20.3-20.4°W. Also, using data sampled by the digital seismic network in Iceland, **SIL**, from July 1991 to February 1992, Stefánsson et al. (1993) also discovered two concentrations of recent seismic activity where the historical records had shown low strain release; namely at -20.3°E and -20.7°E. These findings further pointed to the fact, that a sequence of large events in the SISZ was imminent.

In June 2000 two large earthquakes of magnitudes M_L 6.4 and M_L 6.5 (Pétursson and Vogfjörð, 2009) occurred in the SISZ. The former one occurred in the Holt district on 17 June. The seismic activity migrated westwards and the second major earthquake struck three and a half days later, on 21 June, south of lake Hestvatn (Figure 1.2). Following the earthquakes, seismicity greatly increased in all of Southwestern Iceland. Roughly nineteen thousand microearthquakes were recorded by the SIL network in Southwest Iceland between June and December 2000 (Figure 1.2) and a 90 km long section of the plate boundary was activated. The third and most recent large earthquake in the ongoing sequence took place in the SISZ on 29 May 2008. It originated about 18 km west of the Hestvatn fault but occurred on two parallel faults 4 km apart, with a combined magnitude of M_L 6.3 (Vogfjord et al., 2009) (Figure 1.2).

The goal of this study is to map sub-surface fault planes using the relocated aftershock distribution induced by the 17 June (J17) and 21 June (J21) 2000 earthquakes and determine the slip distribution on them. A multi-event, relative relocation method is used to relocate the interactively located events. This method can increase location accuracy to such a degree that fault patterns, defined by the microearthquake distribution, may become resolvable. Detailed surface fault patterns have been mapped in the SISZ (Einarsson et al., 1981, Einarsson and Eiríksson, 1982; Bjarnason et al., 1993; Bergerat and Angelier, 2000; Clifton and Einarsson 2005) but large sub-surface fault planes have not been mapped in such details before. The method has however been used to map smaller faults in many regions of Iceland, e.g. in the Tjörnes fracture zone (Rögnvaldsson et al., 1998a), in the Hengill area (Rögnvaldsson et al., 1999; Vogfjörð, 2000; Vogfjörd et al., 2005a), in the western volcanic zone (Hjaltadóttir and Vogfjörð, 2009) and on the Reykjanes Peninsula (Hjaltadóttir and Vogfjörð, 2006). A detailed map of sub-surface faults with slip directions can be of great value for stress-field evaluation in the seismic zone. It is also of great importance in the volcanic zones, as it can partly reveal the fault plumbing systems delivering fluid into the geothermal systems. Furthermore, the depth distribution of the relocated seismicity is compared to recent studies of crustal composition and used to estimate the thickness of the brittle crust in Southwest Iceland.

The area under study encompasses Southwestern Iceland, from the Reykjanes Peninsula to the eastern end of the South Iceland seismic zone, with the addition of the area surrounding the Geysir geothermal system in the north, located at the eastern margin of the western volcanic zone. The regions were divided into fifteen boxes, marked A-O in Figure 1.2, according to the clustering of activity. The hypocentres of the two J17 and J21 earthquakes are marked as large green stars in boxes N and O, respectively. The J17 earthquake triggered four additional events of magnitude M~5 (Vogfjord, 2003). The hypocenters of these are marked by smaller green stars in Figure 1.2.

2
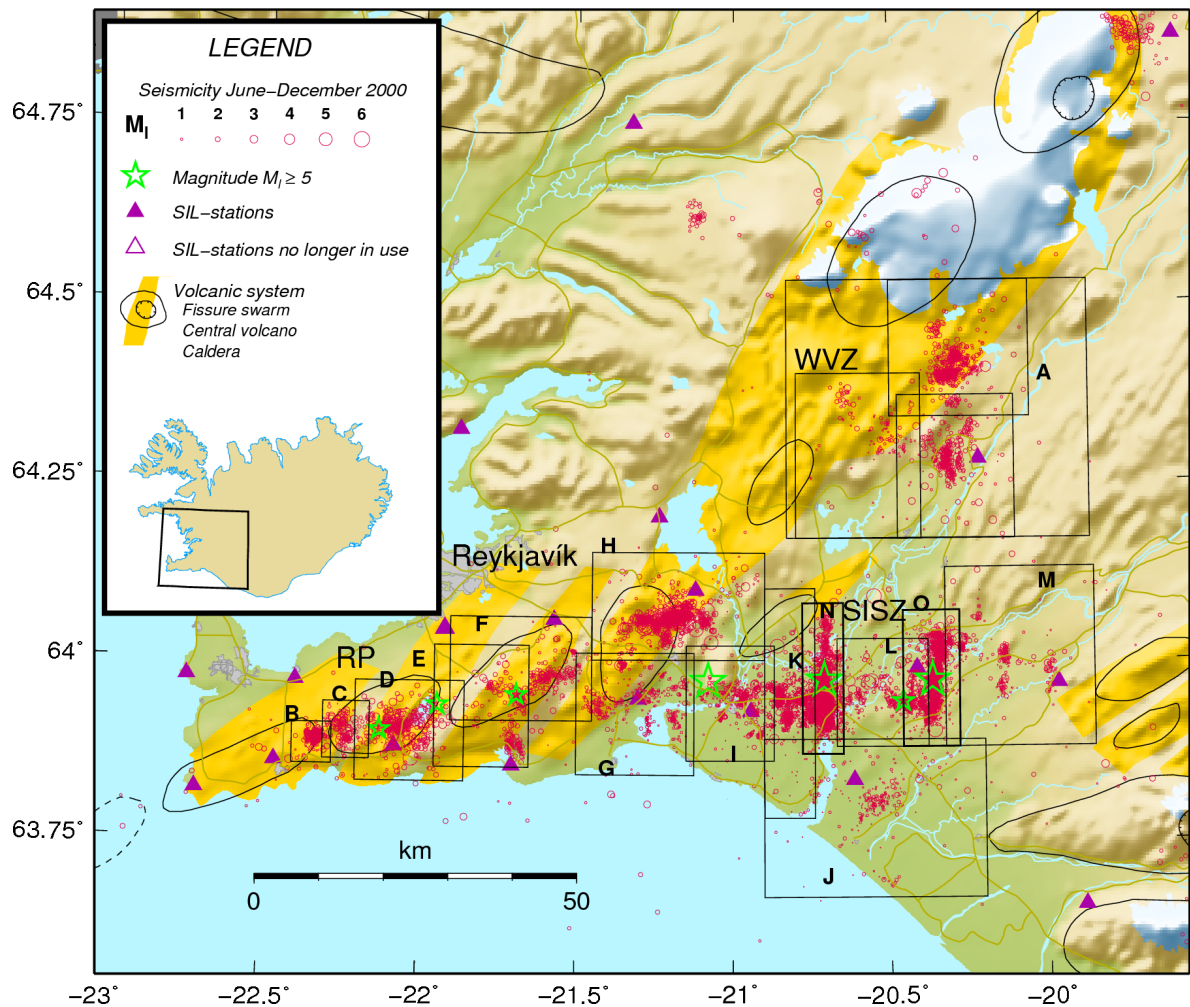
Figure 1.2. *Map of Southwestern Iceland showing the aftershock activity in June-December 2000, following the two M_L ~6.5 earthquakes on 17 June and 21 June. Their epicentres are plotted as large green stars in boxes O and N respectively. The epicentre of the 29 May 2008 earthquake is also marked in box I. The four smaller green stars show the hypocentres of four M~5 earthquakes, triggered by the J17 event. The study area was divided into fifteen boxes, outlined on the map and marked by A-O, for analysis. Roughly half of the nineteen thousand events displayed here, occurred outside the two main faults. Main tectonic features are also shown (after Einarsson and Sæmundsson, 1987).*

1.1 Tectonics of Southwest Iceland

The south Iceland seismic zone is a 70 to 80 km long and 10 to 15 km wide left-lateral shear zone which takes up the transform motion between the oblique Reykjanes Peninsula (RP) rift zone and the western volcanic zone and the eastern volcanic zone respectively. Several historical records of destruction resulting from earthquakes in the South Iceland lowlands exist, the oldest one from 1164 describing damage, most likely caused by an earthquake that same year (Thoroddsen, 1899 and 1905). Major sequences recur at intervals between 45 and 112 years. They often begin with a large earthquake in the easternmost part, which is then followed by a set of earthquakes migrating westwards (Einarsson et al., 1981).

Although the trend of the zone is east, the historical data show that destruction zones of individual earthquakes tend to be elongated in a northerly direction (Einarsson et al., 1981). Mapped surface faults from these historical events also show the same trend in strike (Einarsson and Eiríksson, 1982; Clifton and Einarsson, 2005), further supporting that the transform motion has taken place mostly on a series of parallel north-trending faults, instead of a single large E-W fault. This type of faulting has been termed "bookshelf" faulting, as the blocks are thought to be slowly rotating counter clockwise when the northern block (i.e. the Hreppar micro-plate) moves left relative to the southern block (the Eurasian plate). This rotation leads to a relative right-lateral motion on north-striking blocks, representing the nascent stage of a transform zone (Einarsson and Eiríksson, 1982; Bjarnason et al., 1993). The SISZ is thus thought to be a relatively young transform zone which has been prevented from stabilizing by the gradual southwest propagation of the EVZ during the past 3 million years (Einarsson and Eiríksson, 1982; Guðmundsson and Brynjólfsson, 1993; Hackman et al., 1990). Bjarnason et al. (1993) suggest that a partial explanation for the formation of these rotation blocks, may lie in pre-existing weaknesses in the crust as a controlling factor in their formation, but north of the SISZ, in the so-called Hreppar district (situated on the HM between WVZ and EVZ, Figure 1.1), the rocks show an abundance of normal faults with average strike close to N36°E. These were probably formed in connection with rifting. Bergeret and Angelier (2000) also reasoned that some of the normal faults they examined in the region were probably produced in a rift-type regime. The present day (Holocene) stress-field inferred from their analysis of earthquake focal mechanisms is consistent with the behaviour of the zone as a left-lateral transform zone, but the recent (Pliocene-Quaternary) stress-field inferred from geological observations, presumably reflects both previous behaviour of the area, at the time it was located inside the rift zone, and its present location. These conclusions may also support the idea of the evolution from rift kinematics to transform motion.

The mapped surface fault patterns in the SISZ are normally arranged in left stepping, *en echelon* arrays (Einarsson et al., 1981; Einarsson and Eiríksson, 1982; Bjarnason et al., 1993; Clifton and Einarsson 2005). The *en echelon* patterns are often superimposed on each other in different scales and are made up of open fissures and small mounds of soil or shattered rocks, which are usually located between the tips of two side stepping ruptures (Einarsson and Eiríksson, 1982). Individual fissures can be tens of centimetres to tens of metres long and rarely exceed 100 metres. The appearance of surface fractures strongly depends on the nature of the surface material which the faults are exposed in and in some areas it is very difficult to trace faults, such as in the sand-filled *aa* lavas covering large parts of the Land district (Einarsson and Eiríksson, 1982). It is thus likely that the mapped surface traces of major faults in the zone do not show the total length of the faults. Hackman et al. (1990) used boundary element modelling to study the N-S trending faults. They discovered that the system of northerly striking faults can in fact act as a transform fault between the rifting segments east and west of the zone, and that it can accommodate most of the moment release expected for a through-going single fault if the N-S faults are longer and more spatially frequent than already mapped and a 14 km thickness of the brittle crust is assumed. Bjarnason et al. (1993) made a detailed map of the surface ruptures of the 1912 M7 earthquake, which was the first instrumentally measured major earthquake in the SISZ. The total length of the mapped fault trace was only 9 km, but they note that according to eyewitnesses other faults were also formed. These faults are not presently visible, but extended 12 km south of the mapped end of the fault, thus suggesting that the total length of the fault was at least 20 km.

4

The Hengill volcanic area lies at the triple junction, where the western end of the SISZ meets the RP rift zone and the WVZ (Figure 1.2, box H). It hosts three volcanic systems, along with their associated fissure swarms: the presently active Hengill and Hrómundartindur volcanic systems and the extinct Hveragerði or Grændalur system (Sæmundsson, 1992) Mapped surface fissures and fractures in the region predominantly strike N to NE (Sæmundsson, 1995) but fault planes, mapped using relocated earthquakes from 1993-2000, show greater varieties in strikes (Rögnvaldsson et al., 1999; Vogfjörd et al., 2005a). These observations reflect the fact that the Hengill region experiences a mix of complex stresses resulting from both the transform motion to the east and from the rifting zones in southwest and north of the triple junction. Foulger (1988) hypothesized that the continuous microseismicity observed in the Hengill area is caused by thermal crack formation due to active heat sources in the geothermal area. On the other hand, the infrequent and intense seismic episodes release tectonic stress accumulated by plate motion. A period of enhanced seismic activity was observed between 1947 and 1955, and culminated in a magnitude 5.5 event 1 April 1955, approximately 8 km WSW of the town of Hveragerði (Ármannsdóttir, 2008). The most recent seismic episode occurred during the period 1994-1998 when magma is believed to have intruded into the Hengill region and caused 8 cm uplift and heightened seismic activity (Sigmundsson et al., 1997; Feigl et al., 2000). The seismicity was clustered around the centre of the Hrómundartindur-system and culminated in 1998 when two M_L 5.5 and M_L 5.2 (Pétursson and Vogfjörð, 2009) events occurred in June and November respectively. (Rögnvaldsson et al., 1998c; Árnadóttir et al., 1999; Vogfjörd et al., 2005a). Sigmundsson et al. (1997) observed that the majority of the recorded earthquakes between 1994 and 1995 represented strike-slip faulting on sub-vertical planes. They showed that a magmatic pressure source, which was located at 6.5±0.3 km depth beneath the centre of uplift, could trigger the seismicity in the area, which was then close to failure. Surface effects, discovered in the region following the episode, were largely concentrated in the area between the June 1998 earthquake epicentre and the centre of uplift as well as north of the uplift. The surface features trend N or NNE, and short lineaments even trend E. Two N-S striking segments were also mapped farther south, along the November 1998 fault (Clifton et al., 2002).

North of the Hengill triple junction, the rifting takes place in the WVZ. GPS data gathered between 1986 and 1992 showed that only 15% of the spreading takes place on the WVZ, whilst about 85% takes place on the EVZ (Sigmundsson et al., 1995). More recent studies, based on GPS observations between 1994 and 2003 (LaFemina, 2005) and continuous GPS observations spanning 5 years between 1999 and 2004 (Geirsson et al., 2006) additionally infer that rifting across the WVZ increases north to south, whereas rifting conversely decreases southwards in the EVZ. The Geysir region (Figure 1.2, box A) is situated on the boundary of the deactivating WVZ and the Hreppar micro plate (HM, Figure 1.1). The region has not been active volcanically for the past 10 thousand years, but the buried roots of the former central volcano emit heat to the high-temperature geothermal area. Compared to the seismic zone, the region is normally not very seismically active, but it has been known through history, that major earthquake sequences in the SISZ affect the activity of the Geysir-geothermal area (Torfason and Davíðsson, 1985). The geysers in the area have either reawakened and started to erupt more frequently or have become dormant. Thus it seems that major seismicity in the seismic zone activates old faults north of the zone. From 3D-mapping of the bedrock resistivity in the Geysir region with transient electro-magnetic resistivity measurements, two faults can been inferred, one of which intersects the surface in the location of the geysers (Karlsdóttir, 2004). Surface faults however have not been

observed in the nearest vicinity of the geothermal area. To the south the surface is largely covered by wetland, hiding possible faults traces, but the lava to the north has been eroded by glaciers. There, a few faults, striking NE have been mapped near Sandvatn (Figure 3.13), and one NNE-striking fault crossing the northeast slopes of the lava shield Sandfell (Jóhannesson et al., 1990).

West of the SISZ and Hengill region, plate spreading takes place on the Reykjanes Peninsula, which is the landward continuation of the Reykjanes ridge. The plate boundary in this region is highly oblique to the average plate spreading motion, according to the NUVEL-1A plate motion model (DeMets et al., 1990, 1994). Using a simple screw dislocation model to interpret GPS campaign measurements on the RP from 1993 and 1998, Hreinsdóttir et al. (2001) suggested that rifting on the peninsula occurred in pulses, since their research indicated present accumulation of left-lateral shear strain parallel to the peninsula and a lacking rifting component. However, more recent studies based on GPS data collected between 1992 and 2004 by Árnadóttir et al. (2006), and data from 2000-2006 by Keiding et al. (2007), indicate about 7-9 mm/yr opening across the peninsula. In contrast to Hreinsdóttir et al. (2001), these findings point to a constant oblique spreading across the rift zone, although recent major earthquakes of magnitudes up to M6-6.2 (Tryggvason, 1973; Árnadóttir et al., 2004) seem to occur by strike-slip on N-S faults, analogous to farther east in the SISZ (Clifton et al., 2003; Pagli et al., 2003; Vogfjord, 2003; Árnadóttir et. al., 2004). The most recent one was a M_L 5.0 (Pétursson and Vogfjörð, 2009) event which occurred near to Krýsuvík on 23 August 2003. The aftershock activity also revealed a conjugate fault which extends eastwards from the fault, beneath lake Kleifarvatn (Vogfjörð et al., 2004). Sub-surface fault mapping near Fagradalsfjall (Hjaltadóttir and Vogfjörð, 2006) and extensive surface fault mapping has been carried out on the Reykjanes Peninsula, where SW-NE-striking to N-S-striking fauls and fissures have been identified (for example Sæmundsson and Einarsson, 1980; Erlendsson and Einarsson, 1996; Clifton et al., 2003).

1.2 Historic earthquakes in the SISZ

Historical records of earthquake damage in Southwestern Iceland date as far back as to the late twelfth century. The record of large, destructive earthquakes is considered complete for the past three centuries (Einarsson et al., 1981; Thoroddsen, 1899, 1905). Figure 1.3 shows the locations of major earthquakes in the seismic zone between 1706 and 2008. The estimated epicentres of the historical events are marked with white, filled circles and the fault planes drawn with thick, white lines, extending equally long north and south from the epicentres (Einarsson et al., 1981; Halldórsson, 2004; Roth, 2004). They extend N-S according to the shape of the destrucive zones, drawn from historical records (Einarsson et al., 1981). Epicentres of earthquakes in 1998 and 2008 are also marked by circles but their fault planes, as they are inferred from relocated aftershocks, are drawn with thinner white lines (Vogfjörd et al., 2005a, Vogfjord et al., 2009). The epicentre of an event on 21 February 1630 is not marked in Figure 1.3, but the surface ruptures mapped ~2.5 km east of the 1896b fault were active during the 1630 event (see Fig. 5 in Einarsson et al., 1981; Einarsson and Eiríksson, 1982).

The magnitudes of the historical earthquakes have been estimated from the size of their destruction zones (Einarsson et al., 1981). According to this, the earthquake on 14 August

in 1784 is the largest event which has occurred in the SISZ for the past three hundred years (M 7.1), but the event on 6 May 1912, at the eastern margin of the seismic zone, is of similar magnitude (M 7.0) (Stefánsson, 1979; Halldórsson, 2004). The sequence of major destructive events which occurred in the 1700's (1706, 1732, 1734 and two in 1784) was very scattered compared to the next sequence in 1896, when 5 large events occurred within the time span of 12 days (between 26 August and 6 September). The easternmost large earthquake recorded in the area is the M_w=5.9 1987 Vatnafjöll event (Bjarnason and Einarsson, 1991). This event occurred at the western margin of the EVZ and seems to have been caused by strike-slip faulting with no relation to magmatic activity in the volcanic zone.

Historical records do not document as many large, destructive earthquakes on the Reykjanes Peninsula as in the South Iceland lowland. Annals report a destructive event in August 1724 (Thoroddsen, 1899, 1905). The earthquake (M~6) probably took place near to mountain Geitafell (at ~21.5°W, see Figure 3.17) (Halldórsson, 2004). A M~6 event took place near to Hvalhnúkur (see also Figure 3.17) on 23 July 1929. Its exact location is unknown but another event of magnitude M 5.4-6, took place in the same area on 5 December in 1968 (Tryggvason, 1973; Erlendsson and Einarsson, 1996; Halldórsson, 2004). A quite large event also occurred on the RP on 10 June 1933. Its best known location is near to Fagradalsfjall, at 63.9°N and 22.2°W, and it was probably of magnitude M 5.5 (Tryggvason, 1973; Halldórsson, 2004).
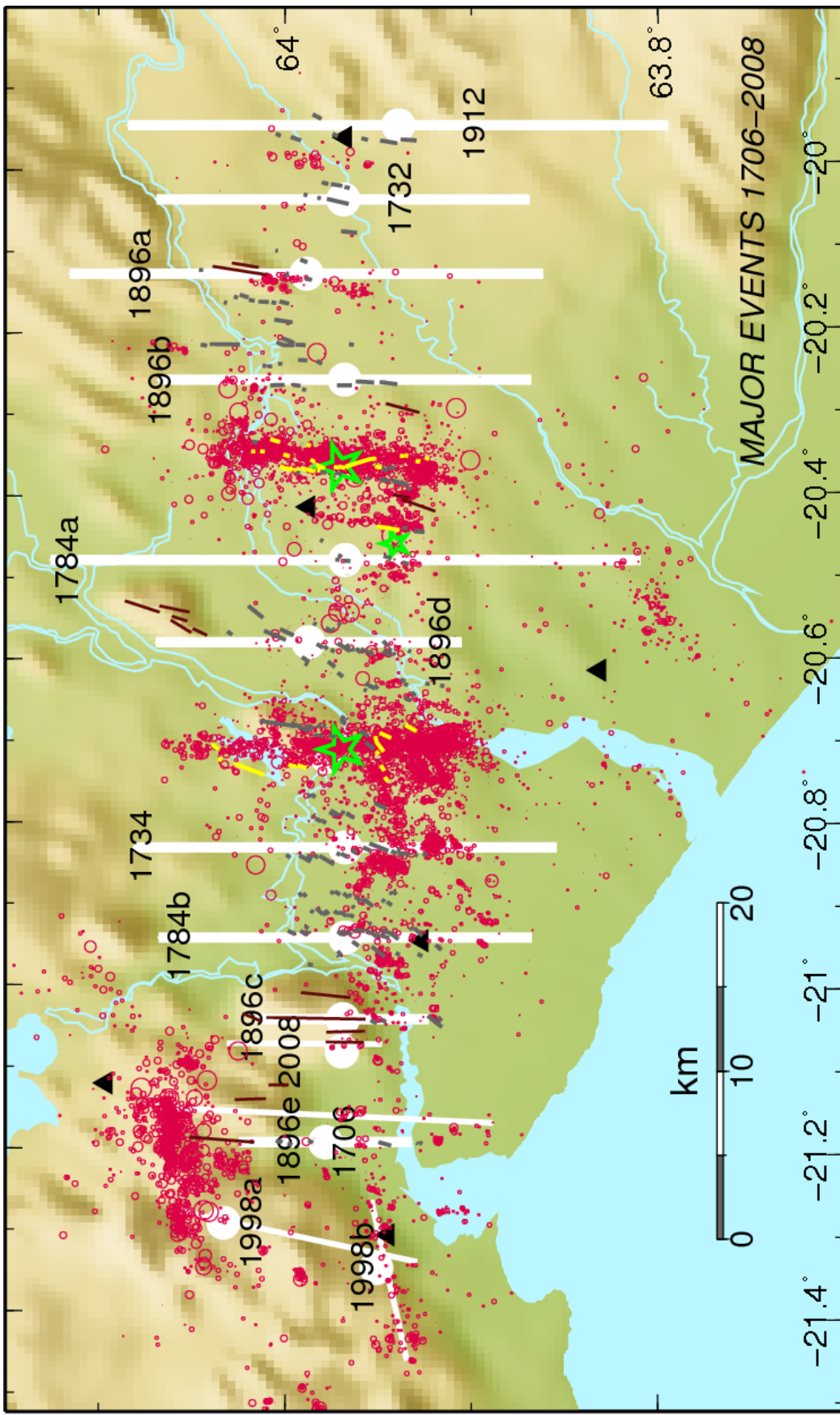
Figure 1.3. *A map showing epicentre locations for the largest earthquakes within the SISZ between 1706 and 2008 denoted by white filled circles. Estimated fault planes of historical earthquakes are shown as white, thick lines (from Roth, 2004). Fault planes from 1998 (Vogfjörd et al., 2005a) and 2008 (Vogfjörd et al., 2009), as mapped with relocated aftershocks, are drawn with thinner white lines. Green stars show J17 and J21 2000 epicentres and red circles the 2000 seismicity.*

1.3 The June 2000 earthquakes

The large M_L 6.4 earthquake on 17 June occurred at 15:40:40.9 GMT. The hypocentre was located at 63.97°N and 20.37°W and a depth of 6.3 km. A preliminary estimation of the fault plane based on the location of aftershocks, indicated a 16 km long and 10 km wide fault plane, striking 9° and with a dip of 86°. (Stefánsson et al., 2000). According to the Global CMT catalogue it has a moment magnitude of M_w 6.5 and a fault plane with 4° strike, 85° dip and -167° rake. Within minutes of the J17 event, four M~5 events occurred (see location of smaller green stars in Figure 1.2). One M_L=5.7 (Pétursson and Vogfjörð, 2009) event occurred near the south end of the J17 fault after 2 minutes (Kvíarholt fault), the other three on Reykjanes Peninsula. Two of these, which triggered slip on the so called Kleifarvatn fault and on the Hvalhnúkur fault, were dynamically triggered by shear waves from the main event after 30 and 26 seconds respectively (Vogfjord, 2003; Antonioli et al., 2006). The third and westernmost event, at Núpshlíðarháls, was however probably caused by static stress changes after 5 minutes, caused by the 30 s Kleifarvatn event (Árnadóttir et al., 2004). The earthquakes' exact location and mechanism determination have proven problematic because their waveforms are clipped and mixed in with the shear waves from the main event (Vogfjord, 2003; Antonioli et al., 2006). Thus, the Kleifarvatn event was not recognized until InSAR results had revealed a large deformation signal between October 1999 and September 2000 (Pagli et al., 2003). Modelling of InSAR and GPS data gives a geodetic moment equivalent to a M_w 5.8-5.9 earthquake for Kleifarvatn (Pagli et al. 2003; Árnadóttir et al., 2004), 5.5 for the Hvalhnúkur event and 5.3 for the Núpshlíðarháls event (Árnadóttir et al., 2004). These magnitudes are comparable to a seismic magnitude estimate of around M 5.5 for the Núpshlíðarháls and Kleifarvatn events (K. S. Vogfjörð, personal communication 2009).

Soon after the J17 mainshock the grouping of microearthquake activity south of lake Hestvatn gave strong indications of where the next large earthquake would occur. A formal warning was issued to the National Civil Protection Agency 26 hours prior to the M_L 6.5 event which occurred on 21 June at 00:51:46.95 GMT. Its hypocentre was located at 63.98°N and 20.71°W and at a depth of 5.1 km. A preliminary estimation of the fault plane based on the location of aftershocks, indicated a near vertical 18 km long and 8 km wide fault plane. (Stefánsson et al., 2000). The Global CMT moment magnitude is M_w 6.4 and the N-S fault plane has a 2° strike, 87° dip and -164° rake.

Extensive surface ruptures were formed during both of the main events and have been mapped (Clifton and Einarsson, 2005; Angelier and Bergerat, 2002) (see also section 3.1.3). The slip distribution on the two large June 2000 faults has also been estimated through different methods. Inversion of strong motion data for the seismic moment distribution on the J17 fault, gives the largest moment release near the fault centre, with a peak below the hypocentre, extending ~8 km northwards along the fault and down to ~8 km depth near the centre (Sandron, 2006) (Figure 1.4). A second but smaller maximum was located at shallow depth (3 km) roughly 6 km south of the hypocentre. Inversion results from combined GPS and InSAR data, show that displacement reaches a maximum south of and above the hypocentre (Pedersen et al., 2003). The peak is between 3 and 4 km depth, roughly 2 km south of the hypocentre, which is both shallower and south of the maximum obtained from the strong motion inversion. The Coulomb failure stress changes, calculated from this same slip model, show an increase in CFS in the area of the J21

hypocentre between 17 and 21 June, as well as correlation between aftershock distribution and areas of increased CFS (Árnadóttir et al., 2003). A second mechanical model based on InSAR and GPS data, which accounts for decreasing stiffness with depth, gives a very similar location for the slip maximum, but also indicates a second maximum north of the hypocentre (Dubois et al., 2008).

Strong motion moment distribution on the Hestfjall-fault (Sandron, 2006) shows maximum moment release just below the surface 3 km north of the hypocentre. The second largest maximum is however located at 5 km depth approximately 1 km south of the hypocentre. According to joint inversion of GPS and InSAR data (Pedersen et al., 2003) maximum slip is obtained 3-4 km north of the hypocentre, at approximately 4 km depth. Similar maxima are observed when assuming varying stiffness in the crust, except that relatively larger slip is attained near the surface (Dubois et al., 2008). This does not agree with the strong motion results but a smaller maximum seen at the same depth 1-3 km south of the hypocentre agrees rather well with the strong motion results. The difference in the slip models obtained from the geodetic and strong motion data respectively could be explained by the fact that the strong motion data record coseismic changes, whereas the geodetic data span a longer period, approximately 2 weeks for the GPS data and 1 month for the InSAR data and thus contain both coseismic as well as any post-seismic deformation occurring during that time (Hjaltadóttir et al., 2005).

The post seismic deformation which was observed the following 1-2 months near the faults was caused by poro-elastic rebound due to pore pressure changes during the earthquakes. Water-level changes recorded in wells in the epicentral area of the J17 and J21 faults are in good agreement with the expected pore pressure changes (Jónsson et al., 2003).
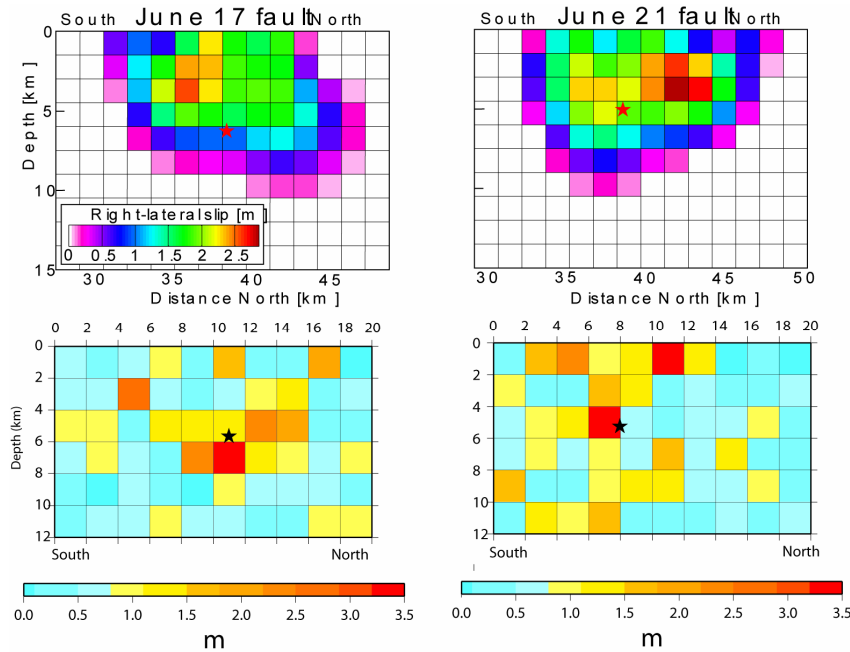
Figure 1.4. *Slip models for the J17 (left) and J21 (right) faults. Upper: slip model estimated from combined GPS and InSAR (from Pedersen et al., 2003). The size of each grid cell in 1.5 km × 1.5 km. Lower: slip models estimated from inversion of strong motion data (from Sandron, 2006). The size of each grid cell is 2 km × 2 km.*

1.4 Crustal structure of Southwest Iceland

The accuracy of earthquake locations is dependent on the knowledge of crustal structure since crustal velocities affect travel times and wave propagation. For the past decades, crustal P- and S-wave velocities and thickness of the Icelandic crust have been determined by various methods. Earlier models, based on data gathered in the 1960s and 1970s, of a hot, thin crust (10-15 km) underlain by an upper mantle with rather low velocity of 7.0-7.4 (Flóvenz and Gunnarsson, 1991), differ from the latest models of a cooler and thicker crust, which reaches a maximum thickness of 35-46 km below northwestern Vatnajökull (Menke et al., 1996; Staples et al., 1997; Darbyshire et al., 2000; Du and Foulger, 2001; Allen et al., 2002). Because this thesis focuses on seismicity in SW-Iceland, a selection of crustal models obtained for that area are compared, as shown in Figure 1.5. Three velocity models are plotted for the RP and four for the SISZ.

The *P1*-model (red) (Vogfjörð et al., 2002) is derived for both P- and S-waves propagating from a relatively relocated microearthquake swarm in the Hengill area, westwards along the RP. The model has a crust-mantle boundary at 17 km depth, based on a Moho reflection at the centre of the RP. The *Allen-RP* model (orange, dotted) is retrieved at location 63.9°N and 22°W from the HOTSPOT-crustal model (Allen et al., 2002), where the crust is also 17 km thick. The HOTSPOT model is based on S- and surface waves and the P-velocity is derived from the S-velocity using a varying V_P/V_S ratio. The *Weir-A*-model is P-velocity profile A along the RP, from the RISE -project (Weir et al., 2001). It has a crustal thickness of 15 km beneath the western part of the RP, and 16 km west of the Hengill area. The S-velocity is derived from the P-velocity using their mean value of $V_P/V_S=1.78\pm0.02$. The velocity models for the *P1*- and *Weir-A* profiles along the RP are very similar but the *Allen-RP* model shows a lower near surface velocity and a larger range for the Moho boundary, probably because of its lower resolution since it is derived from surface and S-waves (with longer periods than P-waves).

The *P2*-profile (Vogfjörð et al., 2002) extends from Hengill to the east along the SISZ, crossing the EVZ. Another velocity profile, P3, extends to southeast along the south coast. Its velocity model is very similar to that of P2 and therefore not plotted separately in Figure 1.5. The crustal thickness, 22 km, of models *P2* and P3 are based on a Moho reflection observation at Fljótshlíð, south of the eastern margin of the SISZ. The *Bjarnas* P-velocity model is derived at the 690 km location on the SIST-profile (Bjarnason et al., 1993), i.e. at the eastern end of the SISZ, and has a similar crustal thickness, 21 km. It has rather slower velocities and an upper crustal low velocity layer not seen in other models for the area. The *Allen-SISZ* model (derived from the HOTSPOT-model at 63.95°N and 20.8°W) has a crustal thickness of 18 km in the western part of the SISZ. This difference from the *P2* and *Bjarnas* models might be because of the location of the profile in the western part of the SISZ and a 3-4 km thickening of the crust might well occur eastwards through the SISZ.

In general, the crust in SW-Iceland thickens eastwards from the Reykjanes Peninsula along the SISZ to its eastern end (i.e. Weir et al., 2001) and in agreement with this observed thickening of the crust hypocentral depths generally increase eastwards in the seismic zone (Stefánsson et al., 1993; G. B. Guðmundsson and R. Stefánsson, unpublished manuscript, 2000). The velocity models in Figure 1.5 also show that below approximately 6 km depth velocity is higher on the RP than in the SISZ.

The *SIL*-crustal model is an average model which is based on the western part of the SIST-profile and is used in the daily analysis of the *SIL*-data. It has lower velocity between 2-3 and 6 km depth but below 6 km it is slower than the RP models (*Weir-A* and *P1*) but faster than the SISZ-models. Furthermore, it has no Moho boundary and merges with the *P2* and *Weir-A* profiles below 22 km depth. The SIL-velocity model was used in this study since it is used in all routine and daily manual analysis of SIL data in SW-Iceland.
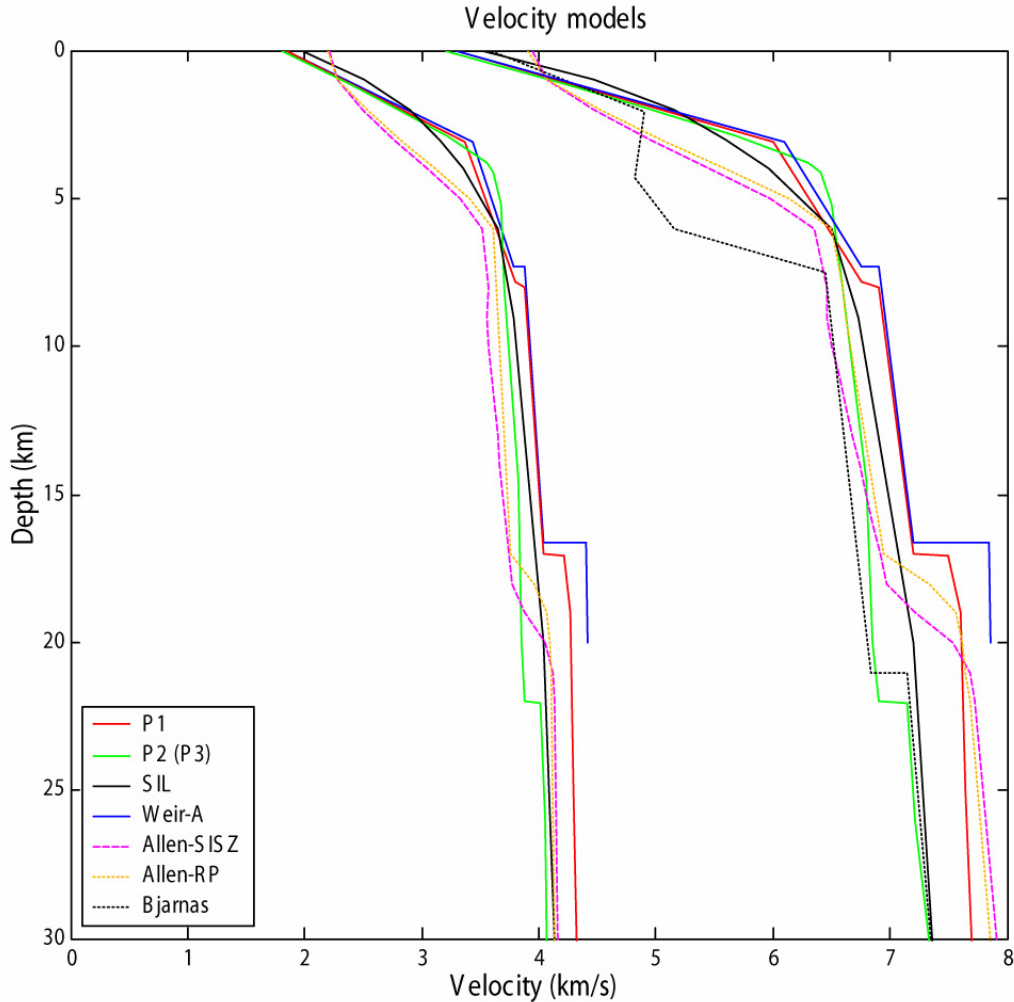
Figure 1.5. *Various velocity models from SW-Iceland. P1 and P2 (P3) (from Vogfjörð et al., 2002, and SIL (from Stefánsson et al., 1993) for both P-and S-waves. Weir-A: Velocity profile A along RP at 120 km, just west of Hengill (from Figure 2d in Weir et al., 2001). Allen-SISZ: Derived from the crustal model in Figure 7d in Allen et al. (2002) at 63.95°N and 20.8°W and Allen-RP derived at 63.9°N and 22°W. P-velocity is derived from S-velocity structure. Bjarnas: P-velocity for one-dimensional profile at 690 km, at Eystri-Rangá, eastern end of the SISZ (from Figure 7 in Bjarnason et al., 1993).*

1.5 The SIL seismic network

The **SIL** (South Iceland lowland) seismic network was originally planned as an earthquake prediction tool for the SISZ (Stefánsson et al., 1993). The first eight stations were installed in 1989 and 1990; of these seven were located in the SIL-area, but one was located west of the volcano Eyjafjallajökull in the EVZ. The system has been collecting real-time data since it became fully operational in automatic mode in June 1991 (Jakobsdóttir et al., 2002). Hypocentral locations are calculated automatically but the locations are also manually checked and corrected daily and source parameters found, such as fault-plane solutions, magnitudes and stress drop (Stefánsson et al., 1993; Rögnvaldsson and Slunga, 1993 and 1994; Böðvarsson et al., 1996). At present, the **SIL**-system comprises 55 three-component, digital, velocity stations, which are mostly distributed around the plate boundary (Figure 1.6). The SIL-network is aimed at monitoring local microseismicity and most of the stations are equipped with short period (0.2 or 1 Hz corner frequency) Lennartz seismometers. For the purpose of monitoring volcanic activity and estimating source parameters for larger events, a wider range of (lower) frequencies is required. The network includes therefore also includes several broad-band stations (Figure 1.6), which in year 2000 were of types STS-2, CMG-3T and -3ESP. The data are sampled at 100 samples per second, but the station clocks have a time accuracy of a 1 ms (Böðvarsson et al., 1998).
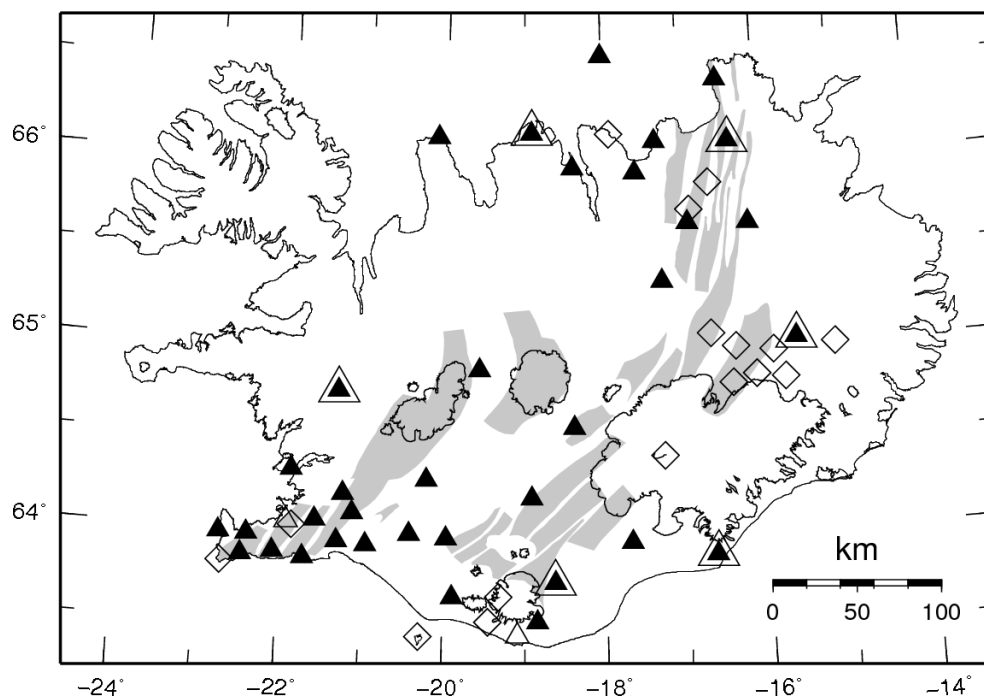
Figure 1.6. *The SIL-network in Iceland. Triangles denote stations in use in year 2000, filled triangles are stations still in operation but open triangles show discontinued stations. Open diamonds denote stations which were installed 2001 and later. Stations outlined by a larger triangle denote broad-band stations in year 2000.*

The detection limit of the system varies in different regions. It depends on station density, different localized background noise at each station, crustal structure and weather conditions. In general events down to M 0, and somewhat lower are detected in the SISZ

and eastwards to the Mýrdalsjökll glacier, where the threshold becomes higher, or close to M 0.7. The sensitivity is greatest in the Hengill area and in distinct parts of the RP, where events down to M-0.75 are detected (Ágústsson, 2006). Based on data between 1991 and 17 June 2000, Wyss and Stefánsson (2006) obtained a threshold of completeness of about 0 in the SISZ but higher (~0.7) in the western RP. The sensitivity is also fairly good on the northern coast, where the TFZ meets the NVZ, and the same applies to north of the Vatnajökull ice cap.

2 Methods

Among the things that affect the accuracy of hypocenter locations are network geometry and density, available phases, arrival time reading accuracy and knowledge of crustal structure (Waldhauser et al., 1999). Within the Icelandic digital seismic network, **SIL** (Figure 1.6), the estimate for reading accuracy for the first arrival is 0.1 s, which corresponds to a distance of roughly 650 m for P-waves (Slunga and Rögnvaldsson, 1995) and therefore earthquake locations have formal estimates of location accuracy in the range 500-700 m for the horizontal coordinates and about 1000 m in depth. Using cross-correlation and double-difference techniques on similar waveforms, it is possible to reduce the error of reading the first arrival down to sub-sample accuracy (<10 ms) as well as minimize the effect of errors in structure and hence reduce location error as far down as tens of meters. Additionally, when similar events occur on the same fault or similar structures, the increased location accuracy can reveal fault patterns and thus enable sub-surface fault mapping.

2.1 Relative locations

Relative location techniques take advantage of the fact that seismic waveforms from microearthquakes occurring in a cluster are often very similar, especially if they originate on the same fault and by the same faulting mechanism. If the inter-event distance is small compared to the distance from the cluster to a receiver, then the seismic ray paths from the events to the station will be almost the same and the small difference in travel time will be primarily due to the relatively short distance between the events. In these cases cross-correlation techniques can be used to determine the differential P- and S-wave travel times with sub-sample accuracy. This can further improve the accuracy of arrival time readings and thus improve the absolute locations.

Different algorithms have been developed to improve locations in this manner. For example Got et al. (1994) developed a relative location algorithm and used it to acquire accurate relative locations of microearthquake hypocentres in a small area beneath the southern flank of Kilauea volcano in Hawaii with an average precision of about 50 m horizontally and 75 m vertically. The method, multiplet relative location method, used cross spectral analysis for vertical component seismograms to find a group of similar events, called multiplets, and to perform time delay computation. Multiplets were then relocated from the set of time delays computed for each doublet (a pair of similar-appearing events) in it. Another algorithm by Waldhauser and Ellsworth (1999, 2000, and 2002) also made use of residuals between the observed and calculated travel-time difference for a pair of events. Their double-difference algorithm was applied to earthquakes on the northern Hayward fault in California, where routinely determined locations were poor, with errors of several hundred meters. After relocation, a much sharper picture of seismicity was obtained with average horizontal and vertical 2σ relative location errors of 15 m and 34 m, respectively. In this method, P- and S-wave differential

travel times, derived from waveform cross-correlation, were combined with equal weights to P-wave catalogue travel –time differences into a system of linear equations, which is solved by means of weighted least-squares. Catalogue data were typically weighted down by a factor of 100 but they were also assigned relative a priori weights of 0.25, 0.75 or 1.0, depending of the quality of the picks.

Like the two aforementioned methods, most relocation algorithms are based on accurate arrival time differences obtained by cross-correlation of waveforms. The algorithm used in this research is based on a double-difference method, i.e. the residuals between observed and calculated arrival time differences for different events, applied to both P- and S-waves, but differs from the method by Waldhauser and Ellsworth (2000) in that it also includes a residual term for the double-difference of the S-P times of the events (last term in equation (3)) (Slunga et al., 1995). For arrival time residuals, e_a, and residual of arrival time differences, e_d, we have

$$e_a(i,j,k) = t_a^{obs}(i,j,k) - T(i,j,k) \tag{1}$$

$$e_d(i,j,k_1,k_2) = t_d^{obs}(i,j,k_1,k_2) - \left[T(i,j,k_2) - T(i,j,k_1) \right] \tag{2}$$

where t_a^{obs} is the observed arrival time, t_d^{obs} is the observed time differences between two events and T is the theoretical arrival time. The subscript i denotes station, j denotes phase, and k, k_1 and k_2 denote events. Here, the t_d^{obs} values are estimated directly from the cross-correlation of similar signals, independent of arrival time observations t_a^{obs}.
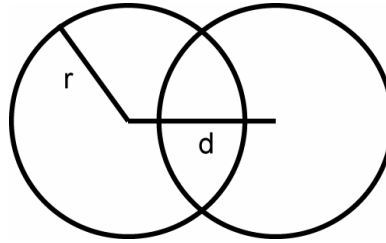
Figure 2.1. *The spatial extent of each group is defined by its radius, r, and the overlap by the distance between the groups' centres, d.*

The software can handle up to 1800 events at a time. Before correlation, events are ordered into groups of predefined minimum and maximum numbers. The division of events into groups also depends on the predefined spatial extent of each group and the allowed distance between the groups centres (Figure 2.1). These two parameters decide the overlap between groups. Each pair of events within a group is then correlated and the events located relative to each other. An event is thus usually relatively located within more than one group - the number of groups depending on the overlap - and the final location is based on a weighted average of the event's locations from all the groups it belongs to. Using cross-correlation the arrival time differences are estimated at each station and for each phase (P and S) for all pairs of events within the group. The internal consistency of the data is checked before starting the location procedure. All timing data are compiled: absolute arrival time observations, the differences in absolute arrival times, all consistent relative arrival time differences and the differences in the relative arrival times of P and S

16

waves between similar events. Then the total weighted square sum of residuals, Q, is minimized using iteration:

$$Q = \sum_{i=1}^{m} \sum_{j=1}^{2} \sum_{k=1}^{n} w_a(i,j,k) e_a^2(i,j,k)$$

$$+ \sum_{i=1}^{m} \sum_{j=1}^{2} \sum_{k_1=1}^{n-1} \sum_{k_2=k_1+1}^{n} w_c(i,j) [e_a(i,j,k_1) - e_a(i,j,k_2)]^2$$

$$+ \sum_{i=1}^{m} \sum_{j=1}^{2} \sum_{k_1=1}^{n-1} \sum_{k_2=k_1+1}^{n} w_d(i,j,k_1,k_2) e_d^2(i,j,k_1,k_2)$$

$$+ \sum_{i=1}^{m} \sum_{k_1=1}^{n-1} \sum_{k_2=k_1+1}^{n} w_{ps}(i,k_1,k_2) [e_d(i,P,k_1,k_2) - e_d(i,S,k_1,k_2)]^2$$

(3)

Here w_a, w_c, w_d and w_{ps} denote weights of absolute arrival times, of differences in absolute arrival times, of relative arrival time differences and of relative differences in the P to S interval, respectively. Retaining only the first term in the sum corresponds to a standard single event location. Including the second term is equivalent to a simple joint hypocentre determination with constant station corrections. The last two terms include arrival time differences determined by cross-correlation for a group of similar events. The theoretical travel times are computed for an earth model consisting of horizontal layers with constant velocity gradients. Finally an average location is found for each event, using location results from all the groups it is in.

2.2 Fault plane solutions for microearthquakes, fault mapping and estimation of slip directions

The mechanism of each event recorded by the SIL seismic network is obtained through a grid search, with a 4° angular interval, over all possible combinations of strike, dip and rake (Rögnvaldsson and Slunga, 1993 and 1994). The radiation pattern at each grid point is calculated and compared to the measured amplitudes at each station and first-motion polarities, where they have been specified. Only those solutions having amplitude error within certain limits and fulfilling the polarity requirements, with a few exceptions, are stored as possible fault-plane solutions for the event.

When fault patterns that are revealed by the relocated event distribution are mapped, events that are considered belonging to the same fault are manually selected. Plotting only events having low relative error often helps to distinguish/identify fault patterns, as well as comparing the relocated event distribution to previously mapped surface ruptures. The best fitting plane through the events defining the fault is found by least-squares-method and its dip and strike defines the mapped or common fault plane. Joint interpretation of the relocated event distribution with the focal mechanisms of the events allows the determination of slip directions on common fault planes. Figure 2.2 shows two examples of this joint interpretation: (A) fault A2-03 beneath Sandfell lava shield (Figure 2.3) and (B)

Centre: 64.359N -20.292E 32 events.
Time period 00 06 24 21 24 36. - 00 08 02 11 32 35.

5.9
6.0
6.1
6.2
6.3
6.4
6.5
6.6

Depth (km)

N
E
200 m

Acceptable FPS, best fitting planes

A

Centre: 63.924N -20.826E 67 events.
Time period 00 06 20 14 54 4. - 00 12 01 14 35 45.

4.0
5.0

Depth (km)

N
E
700 m

Acceptable FPS, best fitting planes

B
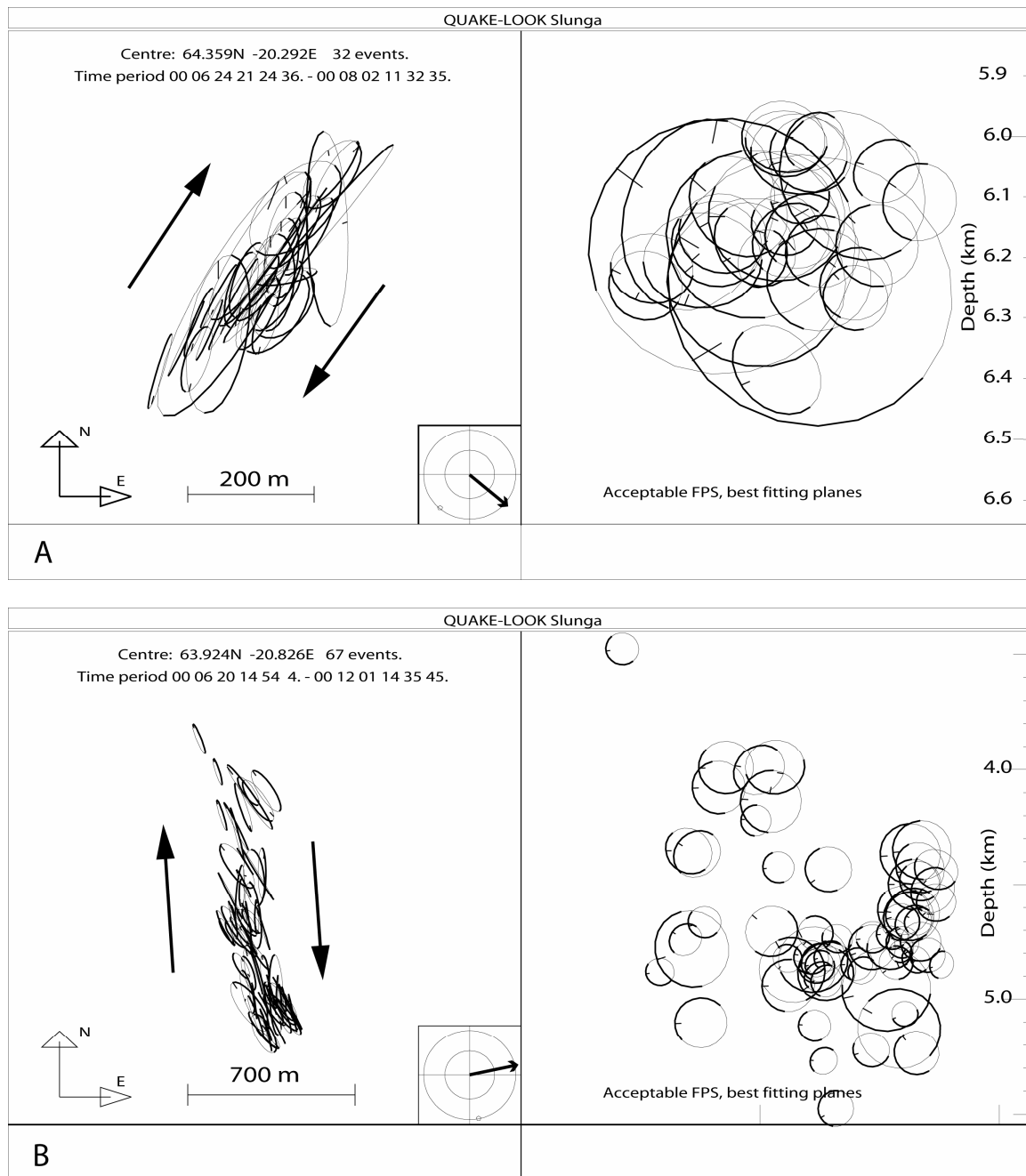
Figure 2.2. *Two examples of joint interpretation of event distributions and focal mechanisms. A) Fault A2-03 in box A2 (Figure 2.3) in map view (left) and vertical view perpendicular to strike (right). Each earthquake is represented by a disk which is oriented according to the focal mechanism that best fits the strike and dip of the common fault plane. Furthermore, the size of the disk is scaled according to the event's magnitude and the tick mark indicates the direction of slip. The angle of view for the vertical section is shown by the arrow in the small boxed circle in the centre of the figure. Here, we look at motion on the western wall from NW and the slip directions on the discs show that it is moving to the NE and slightly downwards, indicating an overall right-lateral motion with a smaller normal component. B) Same scheme as in a). Here we see fault segment K-08 in the SISZ (its location is shown in Figure 3.24, left). On the vertical view we look at the western block from the west. The tick marks show the block moves northwards (to the left), which means a predominant right-lateral motion on this northwards striking fault.*

18

fault K-08 in the SISZ. The faults are shown in both map view (left) and vertical view perpendicular to strike (right). The angle of view for the vertical section is shown by the small arrow in the boxed circle. The fault plane solution (fps) used for each event is the one which is within certain error limits and best fits the strike and dip of the common fault plane defined by the event distribution. The fps is represented by a disk, which is scaled to the event's magnitude. The direction of slip is indicated by a tick mark on each circle. In these cases the fault planes are viewed from the NW (A) or the W (B). The slip directions on these western walls are fairly consistent on both faults (A and B) and mainly to the left (i.e. western blocks moving northwards), showing predominantly right-lateral slip. The figures also show that the best fault plane solutions are fairly close to the strike and dip of the overall fault planes.

2.3 Tests for suitable parameters selection

Since the relocation software, which has been under constant development since 1999, had not been rigorously tested, extensive tests were performed to determine its robustness and reliability, as well as the quality of the data. These tests were performed on earthquakes in the Geysir region (box A, Figure 1.2, and Figure 2.3) and entailed: 1) varying the spatial dimension of groups and their overlap, 2) varying the maximum number of events in a group, 3) relocating only the best events to see if they remained stable, 4) rearranging the input data to see if there were any noticeable changes in the results, 5) varying the time-duration of the correlation windows, 6) varying the weights of absolute and relative time differences in the inversion and 7) eliminating data from the station **haf** that was only operating for the first few days following June 17. In general these tests showed the method to be reliable and stable and will now be discussed in more detail.

2.3.1 Varying spatial dimension and overlap

As previously mentioned two parameters control the amount of overlap between groups, i.e. the group radius (r) and the distance between the group centres (d). After dividing the box into three sub-areas, A1-A3 (Figure 2.3), the earthquakes were first relocated in each area using a group radius of 3 km and distance of 3 km. In order to allow more overlap of groups distance was decreased down to 2.2 km and group radius down to 2.8 km. This caused fewer events in different structures to be correlated together. For the first parameter set (r=3.0; d=3.0) most earthquakes were in 2-4 groups but the number increased to 4-8 using the second set (r=2.8; d=2.2). Although the results from the second parameter set are expected to be better constrained, no significant changes were noticed, probably since the values of r and d were not changed significantly. Same fault patterns were observed but many smaller clusters or faults moved, by up to several hundred meters. In other areas however results have been seen to improve when more overlap is used and therefore the values of 2.8 and 2.2 were chosen hereafter.
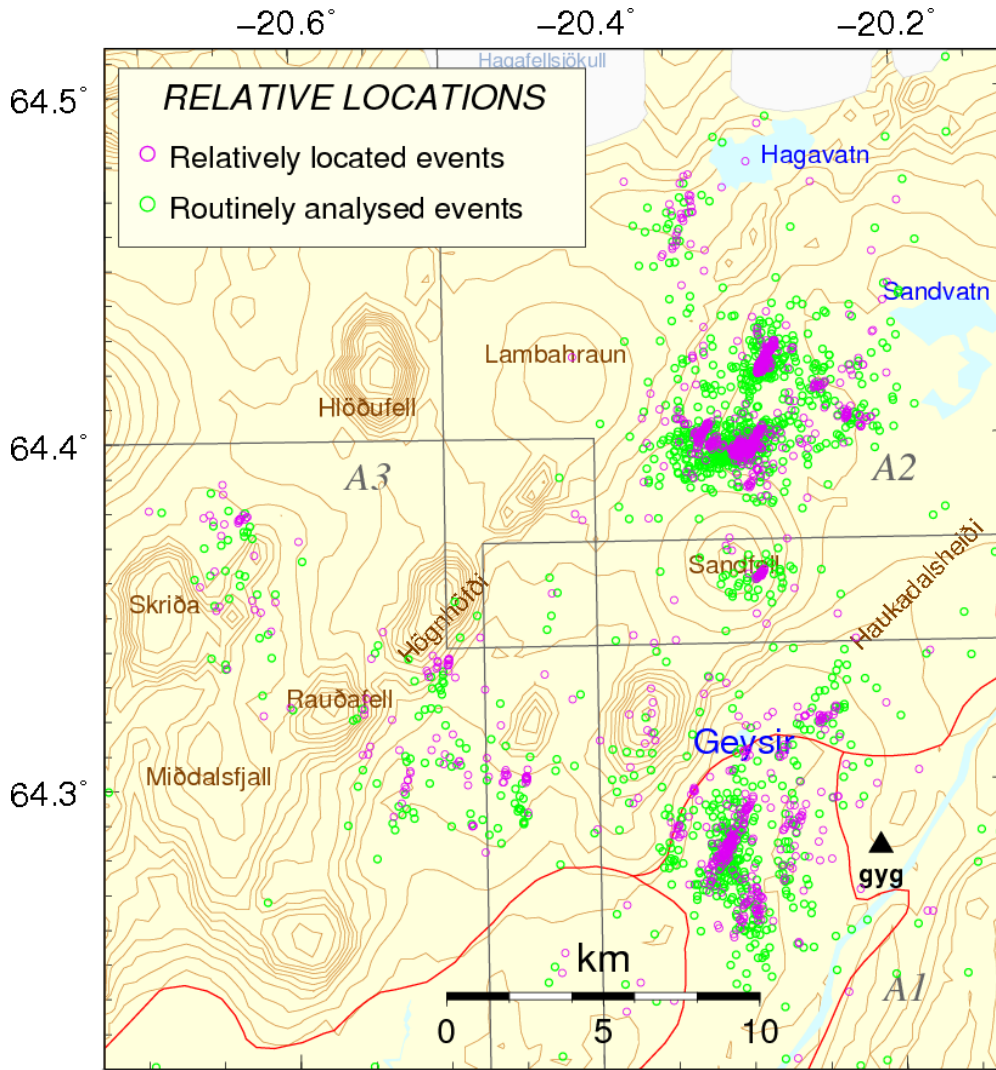
Figure 2.3. *An overview of the Geysir region. The area was divided into three sub-boxes A1-A3, according to clustering of activity. Green circles show the original single-event locations and the purple show significant improvement obtained with relative locations.*

2.3.2 Changing the maximum number of events in a group

The software limit for the maximum number of events per group is 48. By decreasing this number it is possible to reduce the processing time since fewer events are being correlated within each group and the size of the inverted matrixes decreases. Using the minimum number of 6 events per group, the maximum number was varied in small steps, from 48 to 44 and 40. Figure 2.4 shows the resulting locations in the southern part of box A (sub-area A1 in Figure 2.3). Clear fault lineaments can be seen and the main features seem to be stable between the three cases. The shape of the clusters did not change significantly but some of them moved up to several hundred meters. An example is a cluster of earthquakes located below the southern slopes of mount Miðfell. Relative to the *max48* locations the cluster moved 160 m for the *max44* case and 200 m for the *max40* case. Similarly a fault located below the south-eastern slopes of Sandfell moved 150 and 600 m respectively, showing greater difference between cases *max48* and *max44*. To get a numerical estimate for the difference between two test cases, the distance residual was estimated for the change in latitude, and analogously for longitude and depth according to:

$$\Delta dist_{lat} = lat_r(P1) - lat_i(P1) - \left[lat_r(P2) - lat_i(P2) \right] \tag{4}$$

for i=1,…,n and where $r \in [1,...,n]$ is the reference event and P1 and P2 represent the two different sets of parameters whose results are being compared. This residual of relative distances measures the change in distance between the reference event and all other events in the data set for two test cases. If the average value of the function is close to zero, the reference event is well constrained. Figures 2.5a and 2.5b show the distance residuals in latitude, longitude and depth between group sizes of 48 and 40 and 48 and 44 respectively in sub-area A1, where the first event in this dataset is used for reference (P=group-size; r=1). Many events are obviously not well constrained in this area. For example, the residuals in latitude for P1=48 and P2=40 can be as high as 3 km and only 58% of the events have residuals within 200 m from the average value. The difference between the worst located events seems to be less between P1=48 and P2=44. This suggests that a maximum group size of 40 is probably too small, and that larger group sizes give better results. Additionally, since it was not necessary to limit processing time during this research, a maximum group size of 48 was used for all relocations.

In order to find the source of the location instability for some of the events, the relation between the distance residual error and the spatial distribution was examined. The residual plot in Figure 2.5a was divided into five intervals based on the degree of change in distance, i.e. the size of the residual. The earthquakes in interval I, occurring during the first 24 hours after the J17 mainshock, have large residuals and are rather scattered, except for a few which line up on the largest fault south of the geothermal area (Figure 2.6). In interval II (June 18-20), where the residuals are somewhat lower, the events also mostly occur on the largest fault but a few are also scattered outside the fault. In interval III (June 20-23) the residuals increase again and the activity is distributed on various faults and, as in interval I, there are several outliers spread around the area. Interval IV (June 23-30) is more stable where earthquakes mostly form small clusters, apart from several outliers east of the main fault. In the last interval, V (July 1- December 28) more events occur on the largest fault, two small clusters are formed and a swarm occurs below the south-eastern flank of Sandfell. A nearly constant offset for the Sandfell earthquakes can be seen in Figure 2.5a and 2.5b. This change in absolute location of the fault is also clearly seen on the map (Figure 2.4), as mentioned earlier. Equivalent tests were performed in sub-area A2, where comparatively fewer outliers are found and the shift in location of faults between test cases is even smaller. In general one can state that those earthquakes that are more scattered and do not occur on any distinctive faults do not correlate well with other events in the data set. Their location is therefore not as well constrained and differs more between test cases. Exceptions to this are events that have high residuals and occur on faults. When the waveforms of the worst located events were examined, they proved in most cases to be disturbed by other events, occurring close in time. This partly explains why the residuals between test cases is largest in the periods including the J17 and J21 mainshocks, when the induced seismicity peaked and waveforms were often mixed in with waveforms of near events. In other cases, first arrivals had only been picked for a few recording stations. Another reason for the greater location uncertainty for the first 50-100 events in each data set could be that these events are not in as many groups as events in the middle of the data sets, but we have seen that it can take up to roughly 70 events to reach the average number of groups desired for each event to be in, which is 4-8 groups. A larger number seldom improves results but only lengthens the processing time.

2.3.3 Rearrange order of input

In order to test the possibility of diminishing the "end effects" by changing the order of events in the input file, the events in both test areas were rearranged. Although the number of groups increased for the first 40-50 events, hardly any improvement was seen, since the residuals remained very similar. Thus, increasing the number of groups each event is in, does not diminish the "end effects" significantly, probably because of poor quality of the first events in the data set, as mentioned above.

2.3.4 Relocate only the best events

Next it was decided to test how stable the best events (i.e. events with low residuals between test cases *max48* and *max40*) in sub-area A2 were. Events with latitude residuals within 100 m from the average value were relocated again using the same group sizes. Most of the best events remained stable, but not all. This particularly occurred for the first 70-80 events which occurred shortly after the J17 mainshock, and similar effects were observed for the last events. Looking at the number of groups each event was in, it was apparent that many of the first events were only in 1-3 groups. This might well explain the increased residuals. Another likely explanation is that many of the removed events were in the first part of the data set and the remaining events, showing larger relative error, had earlier correlated with them.

2.3.5 Other tests

More tests included weighting down absolute times compared to the relative times, changing the length of the longer correlation window and eliminating data from one station (**haf**, Figure 3.1). Changing the weights had little effect on the results, by default the absolute times are already weighted down by 1/10 in the programs. In the cross-correlation process, two signal windows of different length are compared, containing either a P or S-phase from each event. The length of 2 s instead of 3 s for the longer correlation window, while keeping the shorter at duration of 1 s, had no noticeable effects on the results. The station **haf** was only operating until June 20. Adding waveforms from this station, which was located on the Reykjanes Peninsula, at 80-90 km distance from the test area, made no significant difference, but the waveforms were included in the final relocations for all areas to make use of all available data.
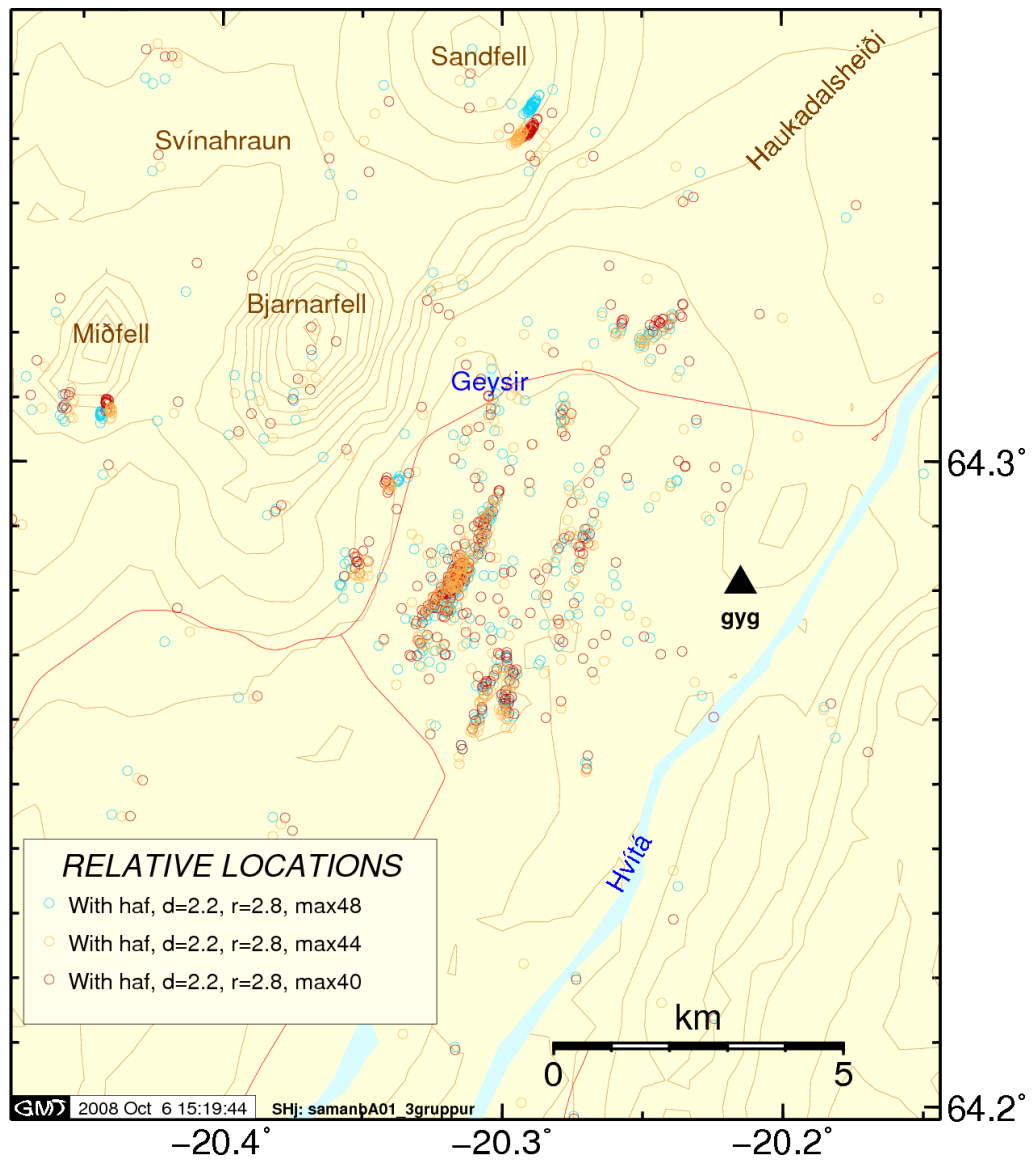
Figure 2.4 *Testing different values for maximum group size in area A1. (a) Relative locations plotted in different colours for different maximum group size of 48 (blue), 44 (orange) and 40 (red).*
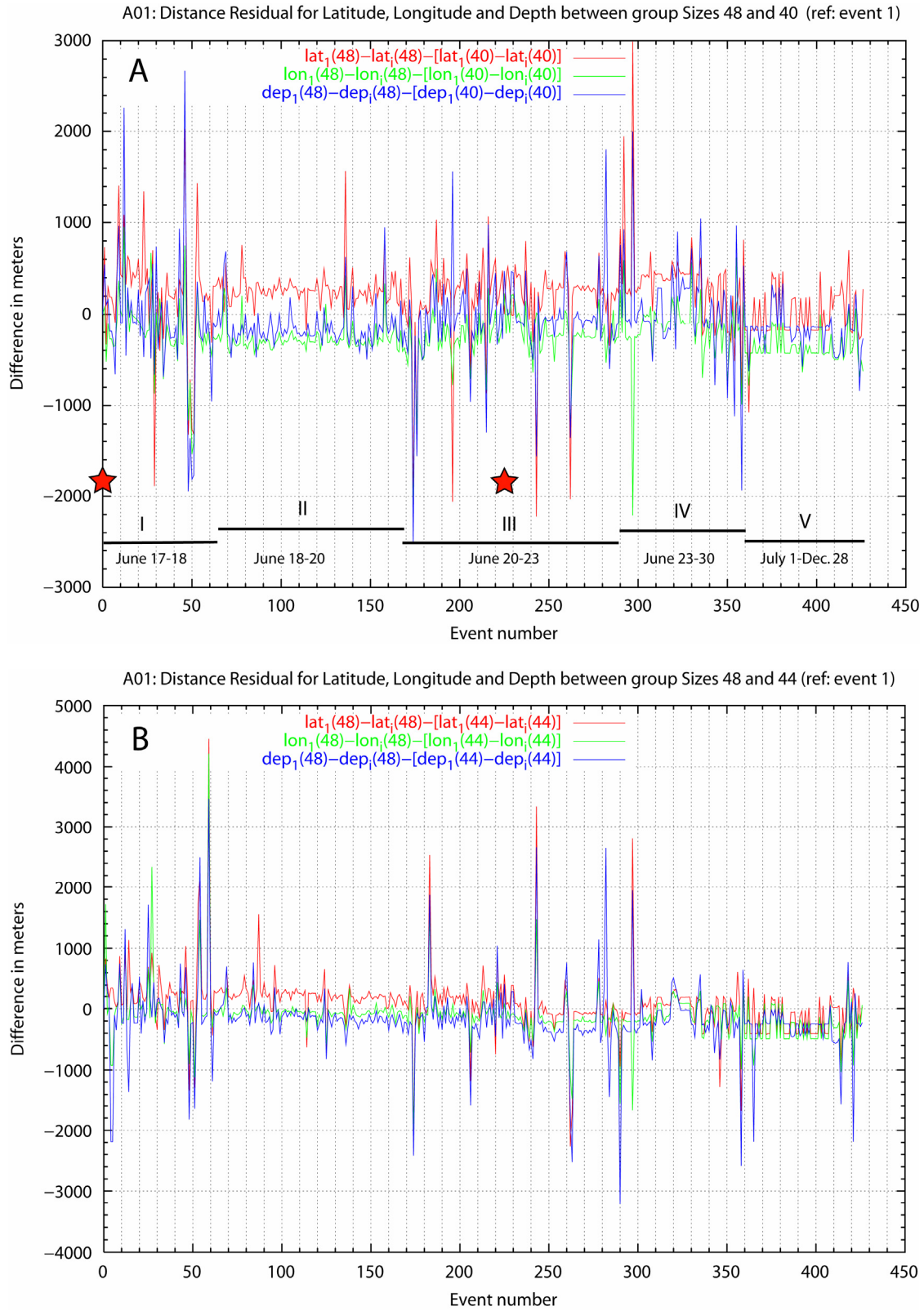
Figure 2.5. *Testing different values for maximum group size in area A1. (a) Distance residuals between test cases max48 and max40 and (b) between max48 and max44. The residual measures the change in distance between the reference event and every other event in the test area in latitude (red), longitude (green) and depth (blue) respectively. The events were divided into five intervals, marked I-V in plot (a), according to the size of residuals between test cases max40 and max48. Events in these five intervals are plotted with different colours and symbols in Figure 2.6. Red stars mark timing of J17 and J21 main shocks.*

24
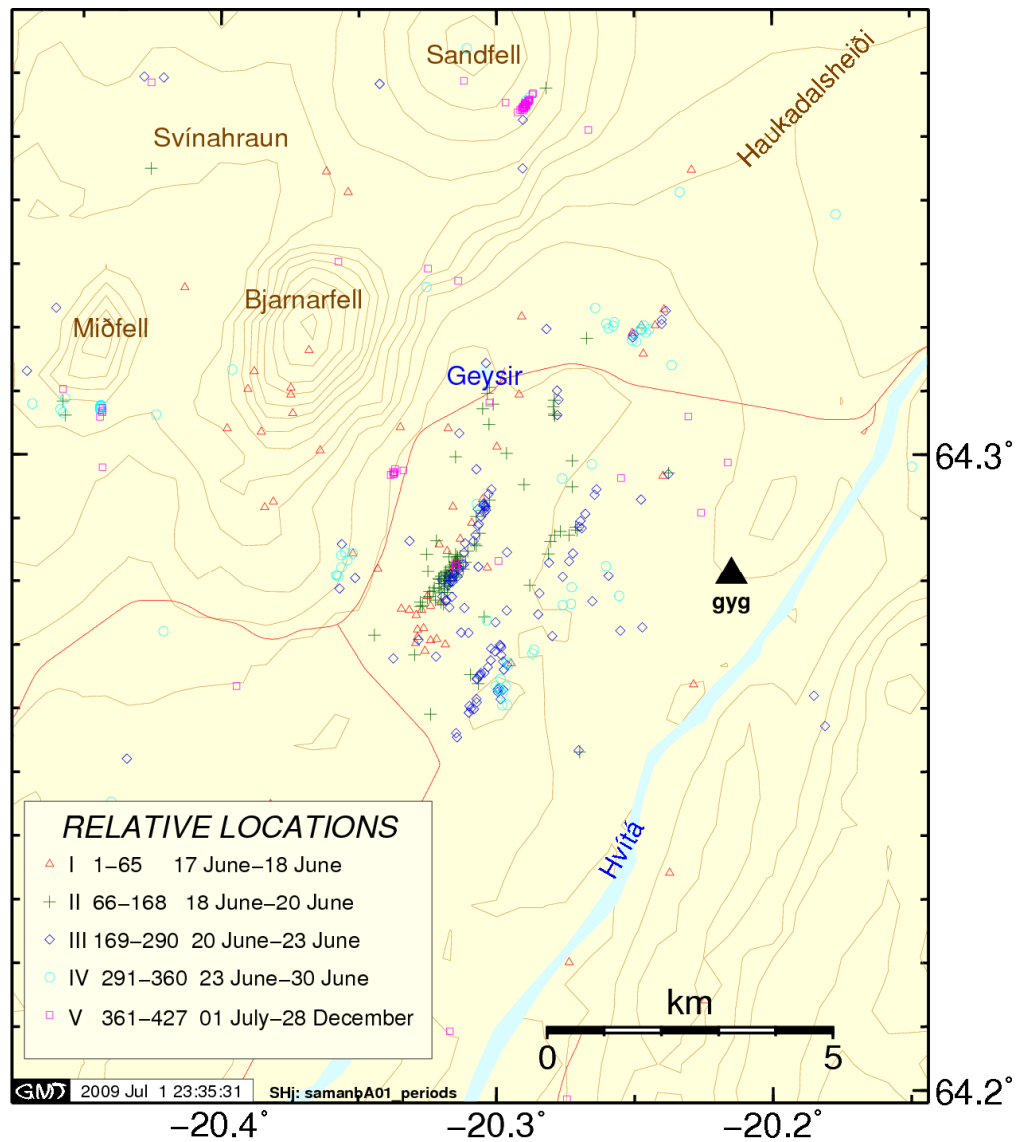
Figure 2.6. *A map showing relative locations in box A1 for maximum group size of 48 plotted using different symbols and colours for different time intervals as discussed in the main text and also shown in Figure 2.5a with respect to event number.*

2.4 Summary

The tests described earlier show that by varying the values of different parameters in the relocation software within reasonable limits, the results do in general remain stable. The absolute locations of faults defined by the relocated events do change slightly between test cases but the majority of the faults have a well defined shape and strike that do not alter significantly, so the fault pattern is stable and relative uncertainty is small. The fault which showed the largest absolute location difference between test cases is situated at a depth of approximately 6 km below the south-eastern flanks of Sandfell, an old basaltic lava shield north of Geysir. As shown in Figure 2.7 the fault has a well defined length and strike, but the horizontal distance between tests in sub-areas A1 and A2 respectively can vary by up to a kilometre. The depth distribution, on the other hand, hardly changes. The reason for this rather large absolute, horizontal location uncertainty may be the complex structure of

the area which the fault lies in. Also, the relative location error of this fault may be higher because of its greater distance from the rest of the activity (Got et al. ,1994 and references therein). But additionally, the seismic stations are not evenly distributed around the area. The closest station, **gyg**, is located at 9-10 km distance to the SSE, which is probably close enough to stabilize the depth, and several stations are located from within 50 km distance to the south and southwest (Figure 1.2). But the azimuthal coverage of the closest stations is poorer in other directions (see station map in Figure 1.6 and in Figure 3.1). The event locations would probably improve with only 2-3 additional stations evenly distributed within tens of kilometres distance from the test area. However, even though the testing of the robustness of the relocation software should preferably have taken place in an area with more densely spaced stations, the tests in the Geysir area have shown that the method can also work excellently in other areas and give stable and reliable results.
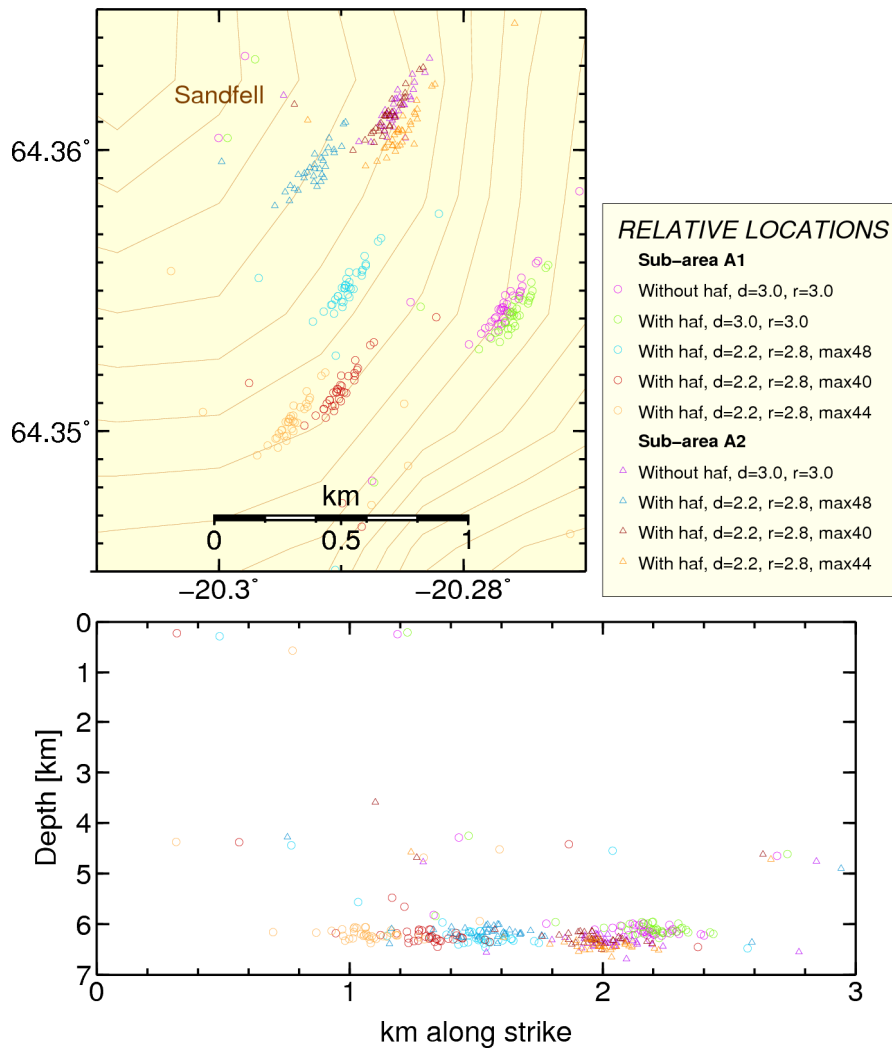
Figure 2.7. *Relative locations for the Sandfell-fault using different sets of parameters (different maximum number in a group and overlap) and correlated with events either in sub-area A1 (circles) or A2 (triangles) Above: map view; below vertical view perpendicular to strike, viewed from N121°E. The events defining the fault are relatively well located but the absolute location of the fault is uncertain.*

26

3 Results and interpretation

In the weeks after the June 2000 earthquakes, intense seismicity occurred in Southwest Iceland. In the Ölfus district however, the seismicity was ongoing throughout the year and until November southwest of Sandvatn (box A2). Furthermore, the main swarm at Fagradalsfjall (box B) occurred in November. Roughly nineteen thousand earthquakes were recorded between January and December 2000 within the boxed areas in Figure 1.2. These were all relocated. In several boxes (C, D, F, H, N, O), events from January - May were also included in the relocation process. As stated earlier (in section 1.4) the SIL velocity-model (Figure 1.5) is used for relocating the seismicity since it is used in the daily, routine analysis of seismicity in SW-Iceland. The method is applied to each box separately. The results of all the relocations are shown in Figure 3.1. The relocated earthquake distribution forms a denser pattern than the initial distribution and many small clusters and lineaments become visible (e.g. Figure 2.3). The fault patterns which have been identified and mapped are discussed in following subchapters as follows: first the fault planes of the two main M_L 6.4 17 June and M_L 6.5 21 June earthquakes, then the largest events occurring within 5 minutes of the 17 June mainshock. Smaller fault planes and fault sections which became active in SW-Iceland during the months following the large events are then discussed within each box, following alphabetical order. Details of the mapped sub-surface faults and fault sections are listed in tables in Appendix A and plots showing the slip distribution of the earthquakes on each fault segment are found in Appendix B. The detailed mapping of the two major faults is summarised in section 3.1.3 and shown in Figure 3.9.

Surface ruptures, also referred to as surface traces of faults in this text, have been mapped widely in Southwest Iceland and their comparison them with the relocated event distribution helps identifying many of the subsurface fault planes. These data are displayed on the maps in following subchapters, where yellow lines show the most recent ruptures which have been mapped and were formed during the 17 and 21 June events (Clifton and Einarsson, 2005) and during the June 1998 Hengill event (Þorbergsson and Vigfússon, 1998). Brown lines show mapped faults in Holocene rock and olive green lines denote faults in older formations (Einarsson and Eiríksson, 1982; Einarsson et al., 2002; Clifton and Einarsson, 2005; P. Einarsson, personal communication 2009). Other mapped surface fractures, fissures and faults are drawn with thin, red lines (Sæmundsson, 1995; Clifton and Kattenhorn, 2006).
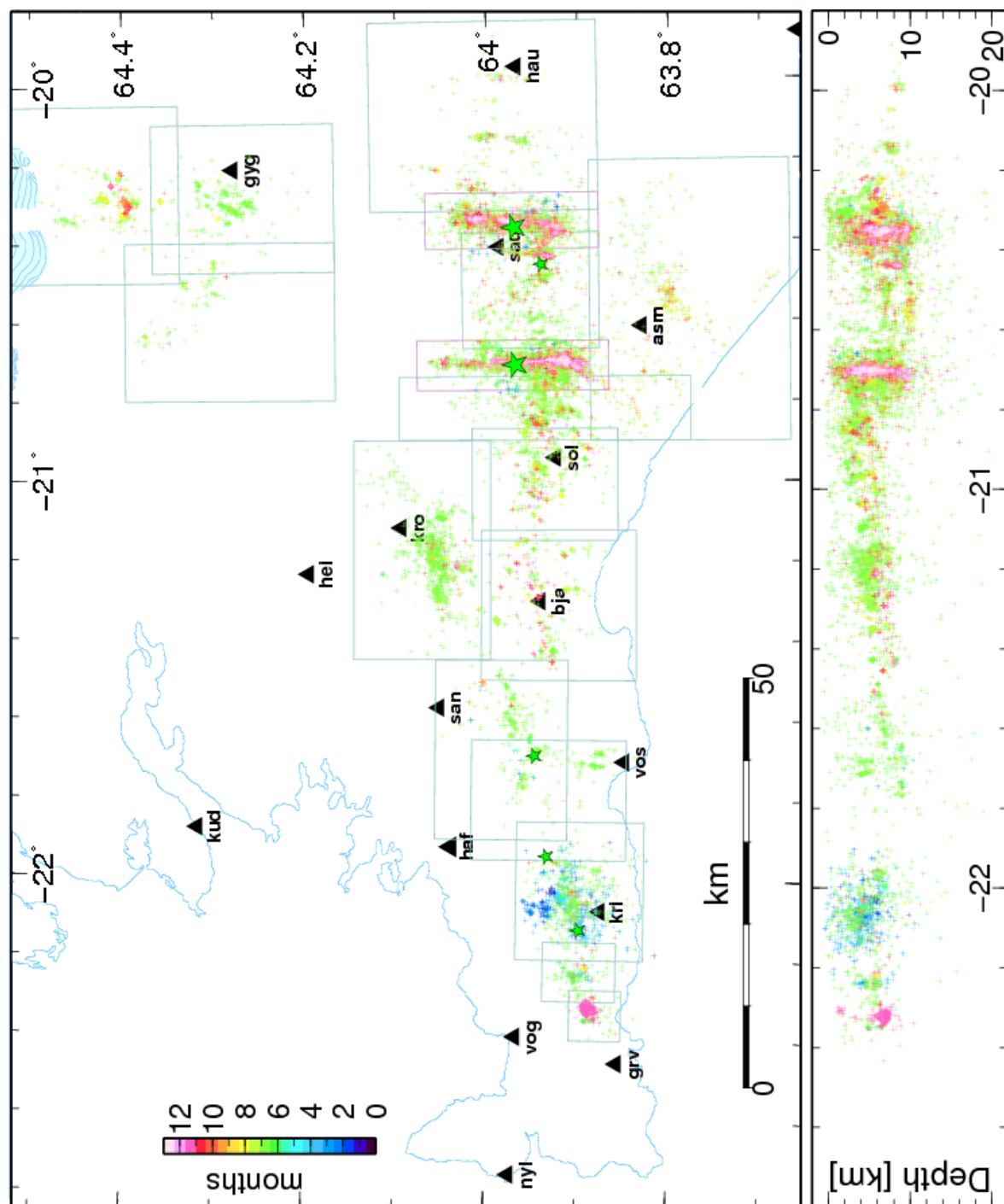
Figure 3.1. A map of all relocated earthquakes in SW-Iceland in year 2000, coloured according to when they occurred. Green stars show locations of events of magnitude 5 and larger. Black triangles denote SIL-seismic stations. Below is a vertical cross section, viewed from the south.

3.1 The two large June 2000 faults and triggered events

3.1.1 The 17 June Holt-fault and the 2 minutes Kvíarholt fault (box O)

The 17 June earthquake in the Holt district ruptured a 12.5 km long and 10 km wide fault. Two minutes after the earthquake occurred, an M_L 5.7 event took place roughly 5 km southwest of the epicentre (Figure 3.1), on the so called Kvíarholt fault. More than 5000 aftershocks were recorded on the two faults between January and December in 2000 (box O in Figure 1.2). Since the number of earthquakes exceeded the maximum number of events the software can handle, the fault was divided into 5 sections for relocation: Osub1 including the northern part of the Holt-fault, Osub2 containing the central patch, Osub3 the southern part, Osub4 including the fault bottom, which are earthquakes below 8.3 km depth, and Osub5 including the Kvíarholt-fault. Details of each fault section are listed in Table A.5 and slip distributions are shown in Figure B.15.

The distribution of aftershocks on the main fault is displayed in Figure 3.2. The aftershocks are mainly confined to the fault margins, mostly below 3 km, and a cluster in the centre of the fault, around the hypocentre. During the first 24 hours however, aftershocks were distributed over the entire fault (Figure 3.2A). The aftershock region is approximately covered by the fault dimension, derived from geodetic data, but aftershock activity is very sparse south of and above the hypocentre where geodetic slip reaches a maximum (Figure 1.4). The aftershock activity shows no increase in depth below the northern patch of the fault where maximum depth of the slip model was attained. The maximum coseismic displacement derived from the strong motion data had a peak below the hypocentre, where the seismicity is sparser than above the hypocentre. A peak in displacement was also found between 4 and 6 km depth in the seismic gap between the north and central segments (around 64°N). With a seismic moment of 7.1×10^{18} Nm, corresponding to the CMT M_w 6.5 magnitude and assuming μ=30 GPa, the fault area defined by the aftershock distribution constrains the average fault slip to be 1.9 m which is in agreement with the geodetic (Árnadóttir et al., 2001; Pedersen et al., 2003) and strong motion (Sandron, 2006) results.

As shown in Figure 3.3, the fault is near vertical with an overall strike of N7°E, but it is composed of many smaller sections with differing strikes (Table A.5). The bottom of the fault (below 8.3 km) and the plane above it were examined separately, see Figure 3.3 A and B. Above ~8 km depth the aftershocks display a rather discontinuous pattern composed of three main sections, each approximately 2-3.5 km long (Figure 3.3B). The central patch is very planar and was active throughout the year. Its strike, N11°E, is slightly east of the overall strike of the fault. Activity on the northernmost fault section is mostly near its northern edge, where it branches into several short N-striking planes. The southernmost section is more continuous and bends westwards with decreasing latitude. At the southern tip the fault jumps half a kilometre to the west and continues on a ~2-km-long segment, which is mostly active between 6 and 8 km depth (Figure 3.3C). West of the southern fault section, a few small faults were also activated, mainly between 3 and 7.5 km depth. Their strikes are generally west of north.

Below 8 km depth the aftershocks define a continuous fault trace, but with kinks at the intersections of the main sections above (Figure 3.3A). Below the northernmost fault section, the bottom appears to be composed of a few smaller en-echelon faults and then breaks up into separate parallel branches farther north. Activity on the southernmost part of the fault, on the other hand, appears to be continuous and more linear, bending slightly westward towards the southern end.
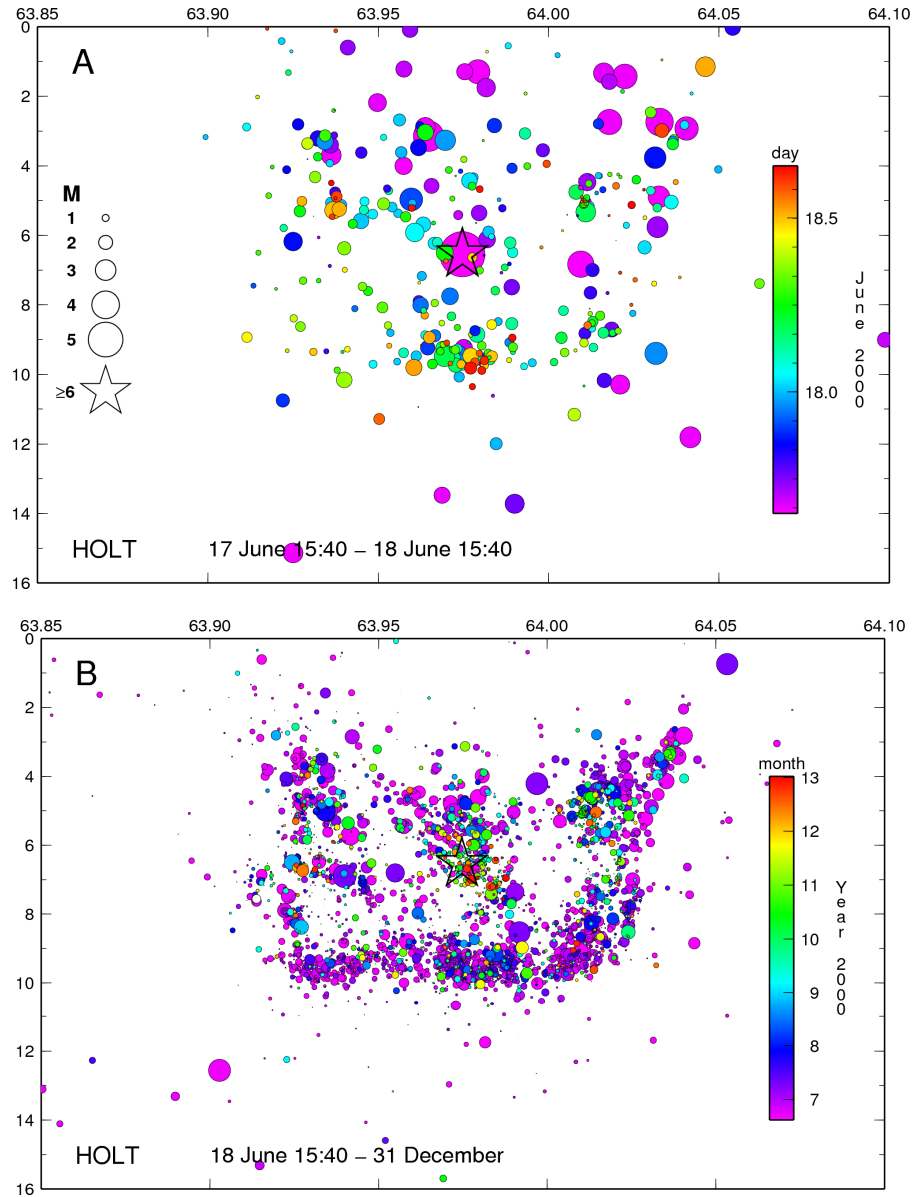
Figure 3.2. *Aftershocks on the J17-fault colour coded according to age. (A) The first 24 hours showing activity distributed across the entire fault. (B) Aftershocks after the first 24 hours and throughout the year showing activity mostly confined to the edges and the central part near the hypocenter, here marked by a star.*

Figure 3.3. *Aftershocks on the Holt fault. (A) and (B): Map view with all events shown in the background in grey. Events on identified faults are colour coded according to age (from 17 June to 31 December). The hypocentre of the main event is shown as a star. The star on the smaller fault, Kvíarholt fault 4 km west of the J17 fault, marks the hypocentre of the second Holt event (M_L 5.7), occurring 2 minutes later. Events below 8 km depth are shown on map (A) and above 8 km on map (B). Events on the second Holt fault, however, even though reaching 9.2 km depth, are all shown on the right. Mapped surface faults are displayed as yellow lines, brown and green lines denote older surface faults which have been mapped previously. (C) E-W section viewed from south showing the coloured events from (A) and (B).*

Fault plane solutions on the different sub-sections of the fault show some variation. Solutions for the events at the bottom of the fault (Osub4-03 in Figure B.15) predominantly show a combination of right-lateral and normal motion, i.e. the eastern block moving slightly downwards. Mechanisms for events in the vertical centre also

indicate a combination of right-lateral and normal motion (λ_{ave}=-151°), but the eastern block moving slightly upwards in addition to the dominant right-lateral slip (ϕ=192°) (Figure B.15, Osub2-11). The major double-couple of the teleseismic Global CMT mechanism, with a -164° rake, agrees well with the bottom mechanisms, which have a similar average rake (-151 for Osub4-03 and -153 for Osub4-05, see Table A.5) and thus shows right-lateral slip and a smaller downwards motion of the eastern block, relative to the western block. Rake angle distribution of the westerly striking faults at the southern end shows a left-lateral motion along with a vertical component, but the overall motion of the group of faults is left-lateral strike slip (section Osub3-06, Figure B.15).
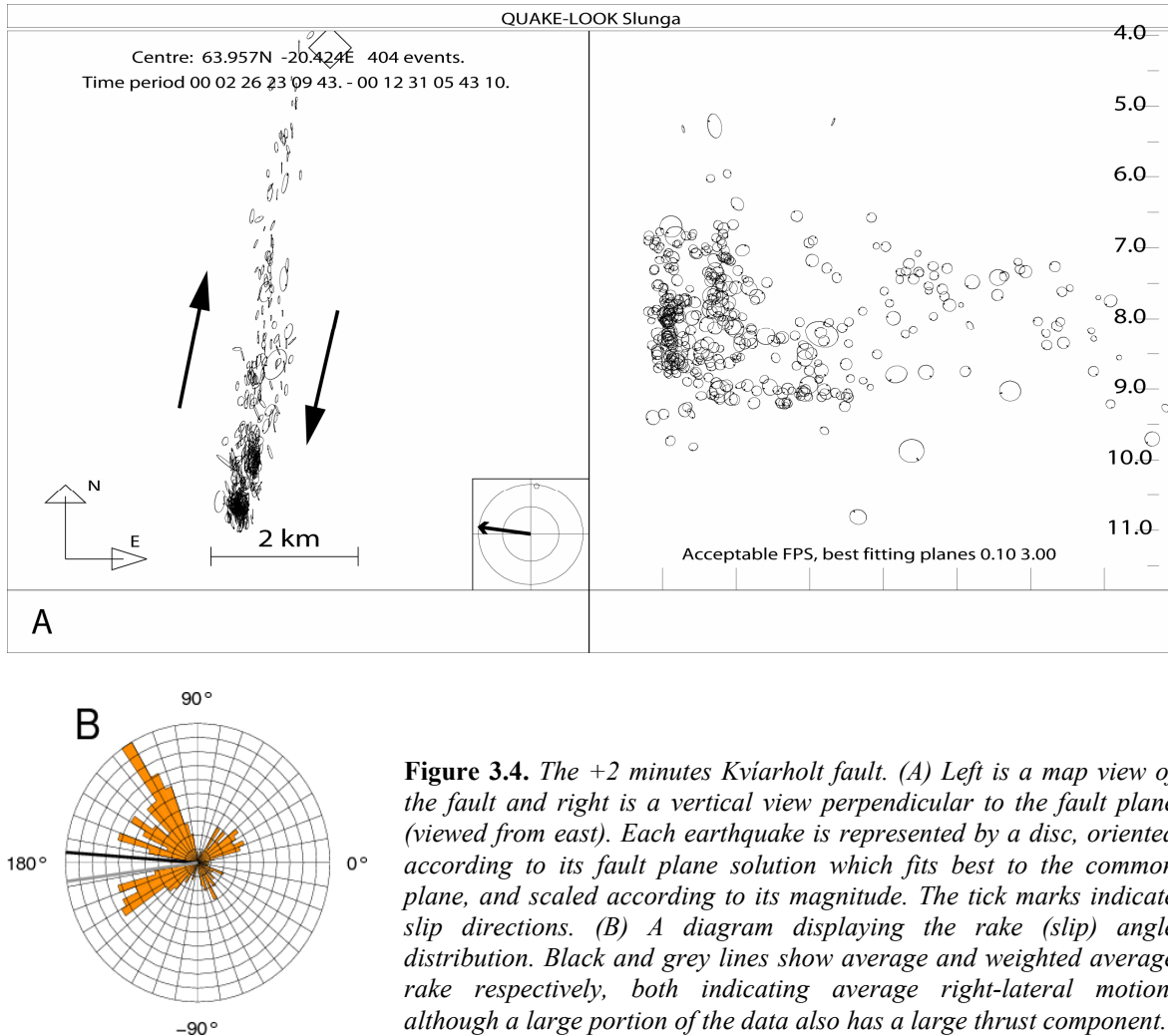
Figure 3.4. *The +2 minutes Kvíarholt fault. (A) Left is a map view of the fault and right is a vertical view perpendicular to the fault plane (viewed from east). Each earthquake is represented by a disc, oriented according to its fault plane solution which fits best to the common plane, and scaled according to its magnitude. The tick marks indicate slip directions. (B) A diagram displaying the rake (slip) angle distribution. Black and grey lines show average and weighted average rake respectively, both indicating average right-lateral motion, although a large portion of the data also has a large thrust component.*

The M_L 5.7 earthquake, which was triggered approximately 4 km west of the Holt fault two minutes after the mainshock on 17 June, ruptured a 6.5 km long fault plane (Figure 3.3B). The roughly 400 aftershocks, are located down to a depth of 9.2 km and define a nearly vertical fault plane (δ=89°, Figure 3.3C) which strikes N187°E. The event distribution on the fault displayed in Figure 3.4A shows that, similar to the Hestvatn fault (discussed in next section), a large part of the activity is concentrated at the fault's southern end. Distribution of rake angles for the aftershocks, shown in Figure 3.4B, shows predominantly right-lateral motion, but a large part of the events have a significant thrust component, moving the western block north and upwards relative to the eastern block, similar to what mechanisms indicate for the bottom of the Holt-fault.

32

3.1.2 The 21 June Hestvatn-fault

The second large earthquake occurred on 21 June south of lake Hestvatn but during the interval between the two main shocks (17-21 June), seismic activity in the epicentral area of the J21 oncoming earthquake was mainly along the bottom of the eventual fault and along the trace of the mapped conjugate surface faults at ~63.95°N, the Bitra segment, which extends westward from the main fault (Figure 3.5). Additionally, seismicity also occurred along a second N-S lineament, located 2 km east of the main fault (at approximately 21.66°W, Nallt-02 in Figure 3.9B).

The 21 June earthquake ruptured an overall 15.5 km long fault plane with an overall strike of N179°E. It also ruptured large conjugate faults to the west of the main fault. The depth of the main fault increases southward, from ~7 km on the northern half to ~10 km at the southern margin (Figure 3.6B). Roughly 6000 earthquakes were located on the fault plane, its conjugate faults and nearest smaller faults which fall within box N. Since the number of earthquakes exceeded the number of which the software can handle at a time, they were divided up into 5 sections before relocation: Nsub1 includes the conjugate faults extending westwards from the main fault, the southern part was split in two sections, Nsub2 and Nsub3, Nsub4 includes events above the bottom, north of sub2 and -3, and Nsub5 includes the bottom of the fault, also north of sub2 and -3. Details of each fault section are listed in Table A.4 and displayed in Figure B.14.

During the first 24 hours following the J21 mainshock, the aftershocks were distributed over the entire main fault up to about 1 km depth (Figure 3.6A). After that, activity concentrated along the bottom, except at the southern end, where it was distributed over the whole depth range and continued throughout the year, much more intensely than on the northern section of the fault (Figure 3.6B). South of the hypocentre, aftershocks are therefore evenly distributed over the fault, while north of the hypocentre the activity is sparser and mostly concentrated near the bottom. South of the hypocentre, but north of the densest activity on the southern half of the fault, is the location of peak slip in the strong motion displacement model (Sandron , 2006) (Figure 1.4). No seismicity is located where the second peak slip is situated at the surface, north of the hypocentre. The plane defined by the aftershocks is mostly covered by the geodetic slip model (Pedersen et al., 2003), except that no slip occurs where the southernmost events are located between 7.5 and 10 km depth. Sparse seismicity is located north of the hypocentre where the geodetic model attains peak. With a seismic moment of 5.4×10^{18} Nm, corresponding to the CMT M_w 6.4 magnitude and assuming $\mu=30$ GPa, the fault area defined by the aftershock distribution constrains the average fault slip to be 1.4 m which is rather smaller than the average slip (1.5-1.8 m) indicated by the geodetic observations (Árnadóttir et al., 2001; Pedersen et al., 2003).

The event distribution is displayed in Figure 3.7. It shows that near the hypocentre the fault branches into two fault sections with different dips. The southern half is vertical and extends north to latitude 64°, terminating at the southern shore of lake Hestvatn (Figure 3.7A). The northern half dips 77° east and extends from the hypocentre to the northern margin of the fault, at 64.05°N (Figure 3.7B). Both branches have the same northerly strike and follow approximately the same trace at the bottom, creating an approximately 3 km long wedge north of the hypocentre. The intersection of the dipping segment with the surface, approximately matches the mapped surface ruptures west of lake Hestvatn. The

faint trace of the dipping part can be seen in Figure 3.7C. At the southern terminus, the fault is broken up into many small, 1-2 km long fault segments with varying strikes.
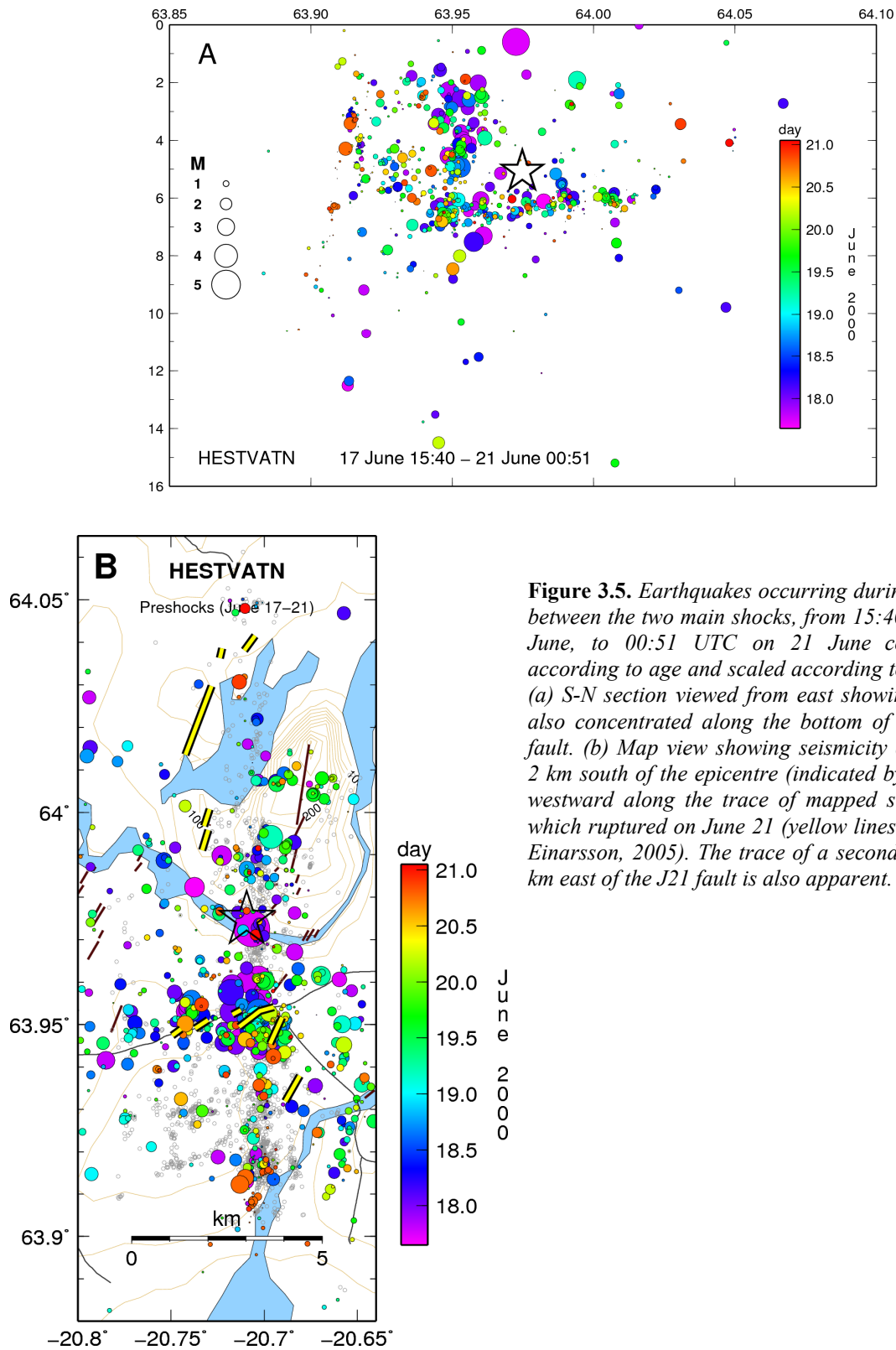
Figure 3.5. *Earthquakes occurring during the period between the two main shocks, from 15:40 UTC on 17 June, to 00:51 UTC on 21 June colour coded according to age and scaled according to magnitude. (a) S-N section viewed from east showing seismicity also concentrated along the bottom of the eventual fault. (b) Map view showing seismicity concentrated 2 km south of the epicentre (indicated by a star) and westward along the trace of mapped surface faults which ruptured on June 21 (yellow lines; Clifton and Einarsson, 2005). The trace of a second N-S fault, 2 km east of the J21 fault is also apparent.*
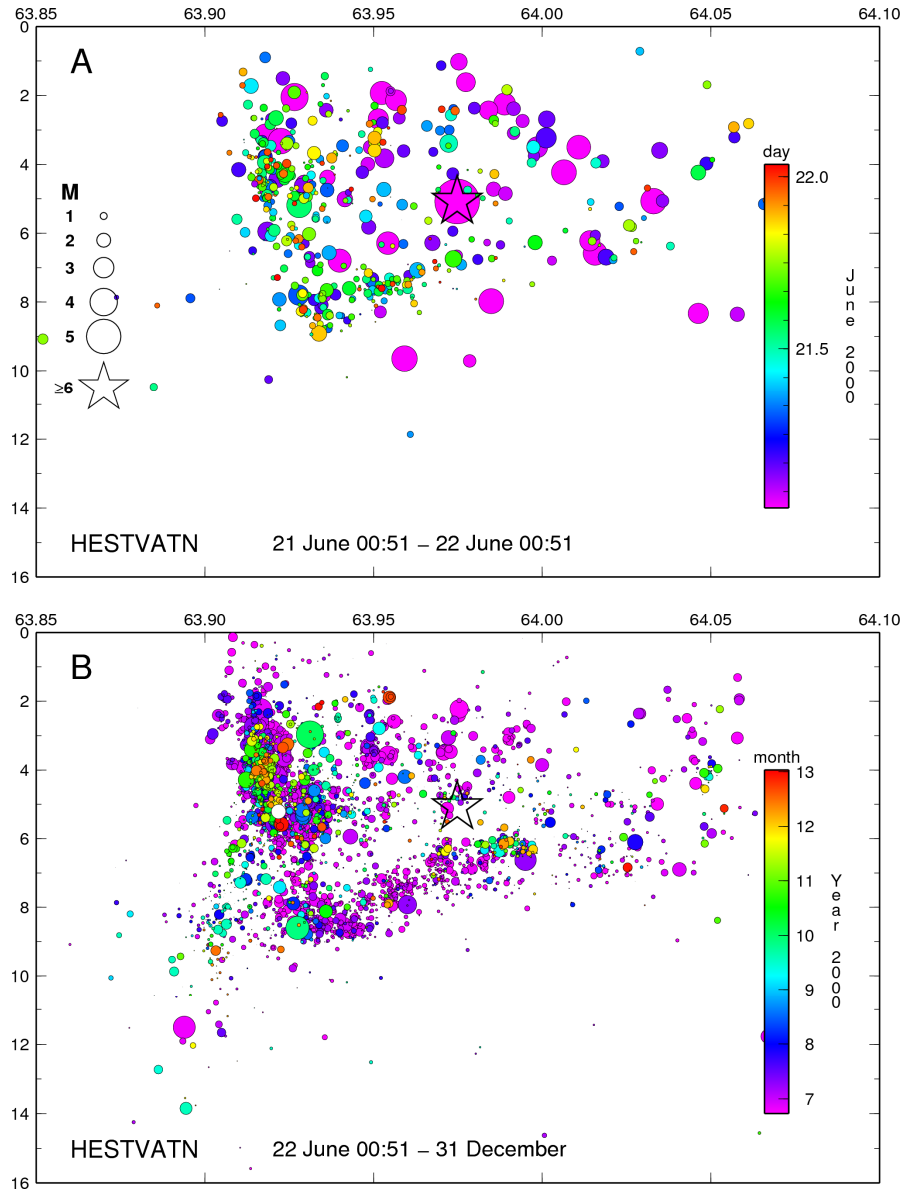
Figure 3.6. *Aftershocks on the J21-fault colour coded according to age. (a) The first 24 hours showing activity distributed across the entire fault, similar to the J17 fault. (b) Aftershocks after the first 24 hours and until December showing activity mostly confined to the bottom and the southern end, where seismicity was persistent throughout the year. The hypocentre is marked by a star.*

Slip directions on the southern end of the fault show predominantly right-lateral motion, with a slightly smaller vertical component, either normal or thrust (i.e. sections Nsub2-3-5-08, Nsub2-04 in Table A.4 and Figure B.14). Dominant right-lateral motion can also be seen on some smaller N-S striking fault sections outside the main fault (i.e. sections Nsub1-03, Nsub1-10, Nsub2-03), while other have very scattered mechanisms (i.e. Nsuballt-02, Nsub2-3-5-06) or show predominantly normal motion (Nsub2-3-5-04, Nsub5-06). Slip directions along the fault bottom have both thrust and normal components accompanying the dominant right-lateral motion, also similar to the bottom layer of the Holt fault (see i.e. Figure B.14, Nsub4-5-10) but the average rake is approximately -170°. The fault section Nsub4-5-05, around the hypocentre, strikes N1°E, dips 85° and the mechanism distribution has an average rake of λ_{ave}=-165° and λ_{wav}=-175°. These results agree well with the major double couple of the global CMT solution with a strike of N2°E,
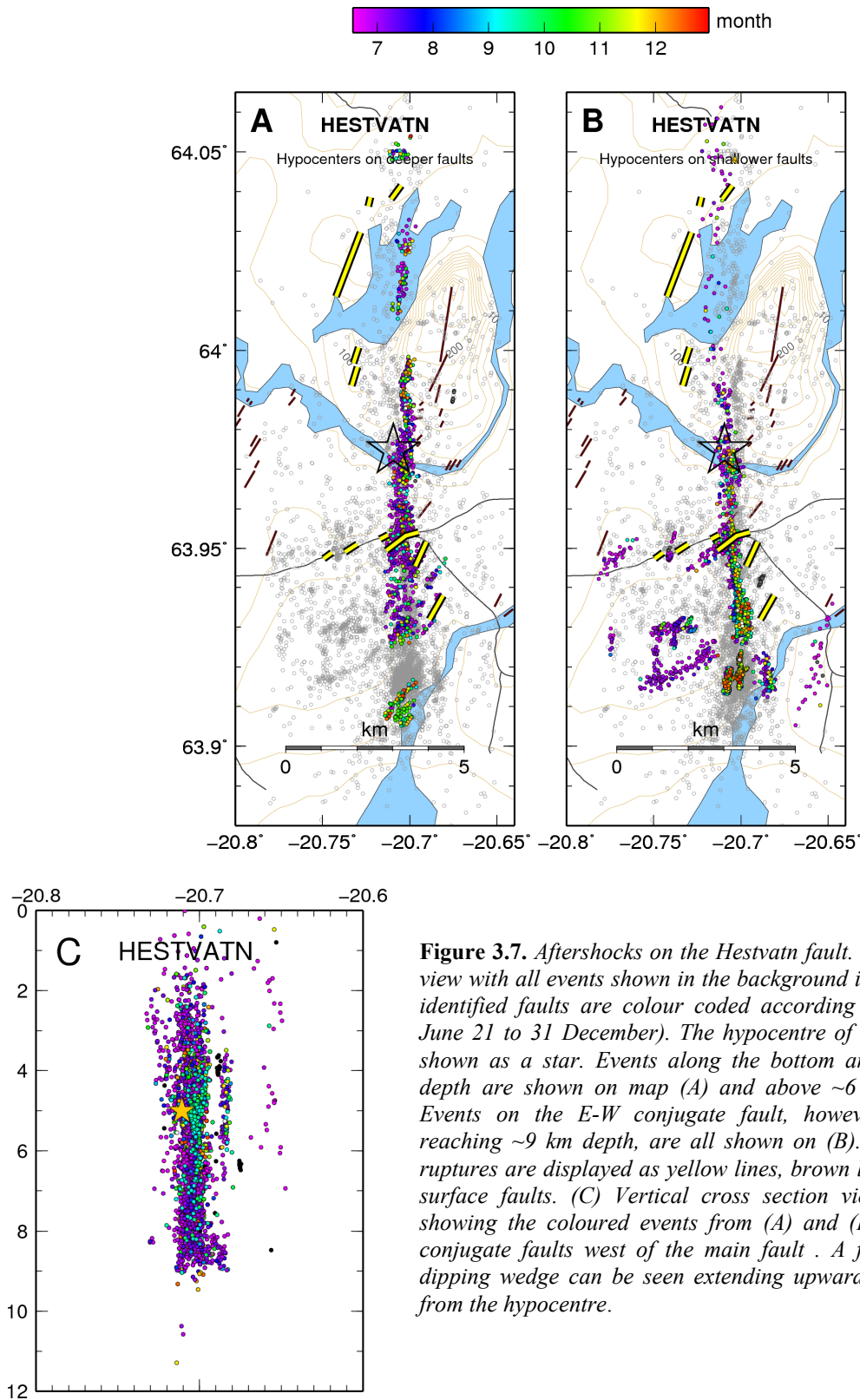
Figure 3.7. *Aftershocks on the Hestvatn fault. (A) and (B) Map view with all events shown in the background in grey. Events on identified faults are colour coded according to age (from 21 June 21 to 31 December). The hypocentre of the main event is shown as a star. Events along the bottom and below 6-7 km depth are shown on map (A) and above ~6 km on map (B). Events on the E-W conjugate fault, however, even though reaching ~9 km depth, are all shown on (B). Mapped surface ruptures are displayed as yellow lines, brown lines denote older surface faults. (C) Vertical cross section viewed from south showing the coloured events from (A) and (B) except for the conjugate faults west of the main fault . A faint trace of the dipping wedge can be seen extending upwards and westwards from the hypocentre.*

dip of 85°and -167° rake.The mechanisms on the 77°- and 74°-dipping segments north of the hypocentre show different average rake of -156° and 178° respectively, whereas the 79°-dipping section at the northernmost end of the fault has a rake of 160°. That is, a thrust component but not a normal component.

Near the location of the mapped conjugate surface-rupture, the Bitra segment (Clifton and Einarsson, 2005), the earthquake distribution is denser and extends westward, mostly on short easterly striking segments (Figure 3.7B). About 3 km farther south, a second set of arc-shaped conjugate faults, facing north and extending over a wide depth range (2-9 km) is also defined by the seismicity. Their overall strike is close to N60°E. The seismicity on the southernmost conjugate fault (Nsub1-02) is displayed in Figure 3.8. Most of the earthquakes on this 2.4 km long fault occurred during a short period following the J21 mainshock and are concentrated at depths between 2 and 5.5 km, except for a few events which extend down to 9 km. The slip distribution is homogeneous and shows pure left-lateral strike-slip motion, in agreement with the motion observed by Clifton and Einarsson (2005) 3-4 km farther north on the surface Bitra segment. The average motion on the smaller WSW-ENE striking segments also shows predominantly left-lateral motion (Nsub1-04, Nsub1-05, Nsub1-08, Nsub1-09 in Figure B.14).

Figure 3.8. *The largest and southernmost conjugate fault extending westwards from the Hestvatn-fault. (A)The events which define the fault are shown in map view on the left and on the right on a vertical cross section viewed perpendicular to the fault plane (from south-east). The disks are scaled according to the earthquake magnitudes (fault radius). The tick marks indicate slip directions and show the southern block move eastwards. (B) A rake angle diagram showing the uniform left-lateral slip distribution observed on this fault. Average rake and weighted average rake (weighted with seismic moment) are shown with a black and a grey line respectively.*

3.1.3 Fault structure of the two June 2000 earthquakes

The approximately 30 fault sections which have been mapped on each of the two J17 and J21 faults are all numbered in Figure 3.9 and listed in Table A.4 and Table A.5. The main fault parameters for the two faults are also summarized in Table 3.1. The chief difference found in the structure of the two faults is that the J17 event ruptured a fault made of three

left-stepping, *en echelon* sections, with each section striking east of the overall fault strike, whereas the J21 event ruptured a fault which is more linear but made of two overlapping sections with different dip. Another striking difference is the aftershock distribution located on the two faults, where seismicity on the J17 fault is rather evenly distributed along the fault, while seismicity on the J21 fault is much more intense on the southern part of the fault than on the northern part, where it is very sparse. Similar to the J21 fault, the aftershock distribution on the M_L 5.7 Kvíarholt fault is mainly concentrated at the southern part of the fault plane. The J21 fault is accompanied by several conjugate faults. Westerly striking conjugate surface ruptures have however not been observed at the J17 fault, although a group of NNW-striking faults extend northwest-wards from the southern tip of the fault (Osub3-04 – 11) and together they form a N319°E striking lineament (Osub3-06) with an average left-lateral strike-slip motion.

The different structure of the two large faults is also reflected by the different teleseismic waveforms observed at the seismic station College in Alaska at a distance of $\Delta=46°$. The comparison reveals a more impulsive and simpler signal for the more linear Hestvatn fault. The more complicated signal for the Holt fault, made of three left-stepping *en echelon* patches which are continuous at depth, has an overall slower rise time made up of three pulses, which may reflect rupturing of the three patches (K. Vogfjörð, personal communication, 2005).

Table 3.1. *Fault* parameters for the two major faults, J17 and J21.

Holt 17 June	**Overall strike: N7°E**	**Width: 10 km**	**Length: 12.5 km**
Osub2-11 central part	ϕ=N192°E	δ=90°	λ_{ave}=-151
Osub4-03 bottom	ϕ=N6°E	(δ=75°)*	λ_{ave}=-152
Global CMT– major double couple	ϕ=N4°E	δ=87°	λ=-164°
Hestfjall 21 June	**Overall strike: N179°E**	**Width: 7-10 km**	**Length: 15.5 km**
Nsub4-5-05 centre	ϕ=N1°E	δ=85°	λ_{ave}=-165
Global CMT– major double couple	ϕ=N2°E	δ=85°	λ=-167°

* Dip estimated for the bottom of the fault is not reliable, since the vertical distribution is very small compared to its length and width.

Mapped surfaces rupture from 17 June (yellow lines in Figure 3.9; Clifton and Einarsson, 2005) show a discontinuous pattern distributed asymmetrically along the Holt-fault as it is defined by the relocated event distribution. Most surface ruptures formed along NNE-striking left stepping *en echelon* segments within a 2 km wide zone, approximately centred on the fault at depth, though the majority occurred on the western edge. When compared to the geodetic (Pedersen et al., 2003) and strong motion (Sandron, 2006) slip models, the distribution and intensity of surface rupture agree well with the geodetic maximum slip, south of the hypocentre, and with the maximum moment, just below the hypocentre. There, a 2.5 km long continuous fracture was observed, west of the event distribution on the centre fault patch (Osub2-11, Osub4-06). Another 3-km-long segment extends northwards approximately 1 km west of the fault, but the northernmost segments lie approximately parallel above and just east of the event distribution, which also shows parallel segments at

depth (for example Osub1-02, Osub1-07, Osub1-03). To the south, the surface ruptures fall just east of and along the southernmost fault section (Osub4-05, Osub3-12, -13 and -14).

Surface rupture from 21 June (Clifton and Einarsson, 2005) shows a discontinuous pattern distributed asymmetrically along the relocated event distribution on the Hestfjall fault. The pattern is more complex than for the June 17 fault. At the southern end of the fault, where the clustering of aftershocks is the densest, no surface rupture has been observed, but 2-3 km farther north, above segment Nsub2-3-5-06, a NNE trending segment lies east of the fault, almost in continuation of the largest left-lateral conjugate fault mapped at depth (Nsub1-02). Another NNE trending segment of similar length is observed 1.5 km farther north, above segment Nsub2-3-5-01. The large conjugate surface ruptures, extend westwards from the fault 2.5-3 km south of the hypocentre. Together, these surface ruptures define a 2.5 km long fault trace, which is, on the other hand, not as clearly seen by the aftershock distribution. Still, at least four segments with different strikes have been identified (Nsub2-3-5-03, Nsub1-4-01, Nsub1-06, Nsub1-11). One of them, Nsub1-4-04, extends from the main fault and is located below the Bitra segment, which strikes N80°E and experienced left-lateral slip of about 0.5 m (Angelier and Bergerat, 2002). The results from the strong motion data show a maximum just below the surface at the location of the conjugate fault. No surface rupture has been observed above the epicentre, but 1.5-2 km further north segments are mapped well west of the linear event distribution, approximately where the 74°-77°-dipping fault intersects the surface (Nsub4-5-04 and Nsub4-5-02).
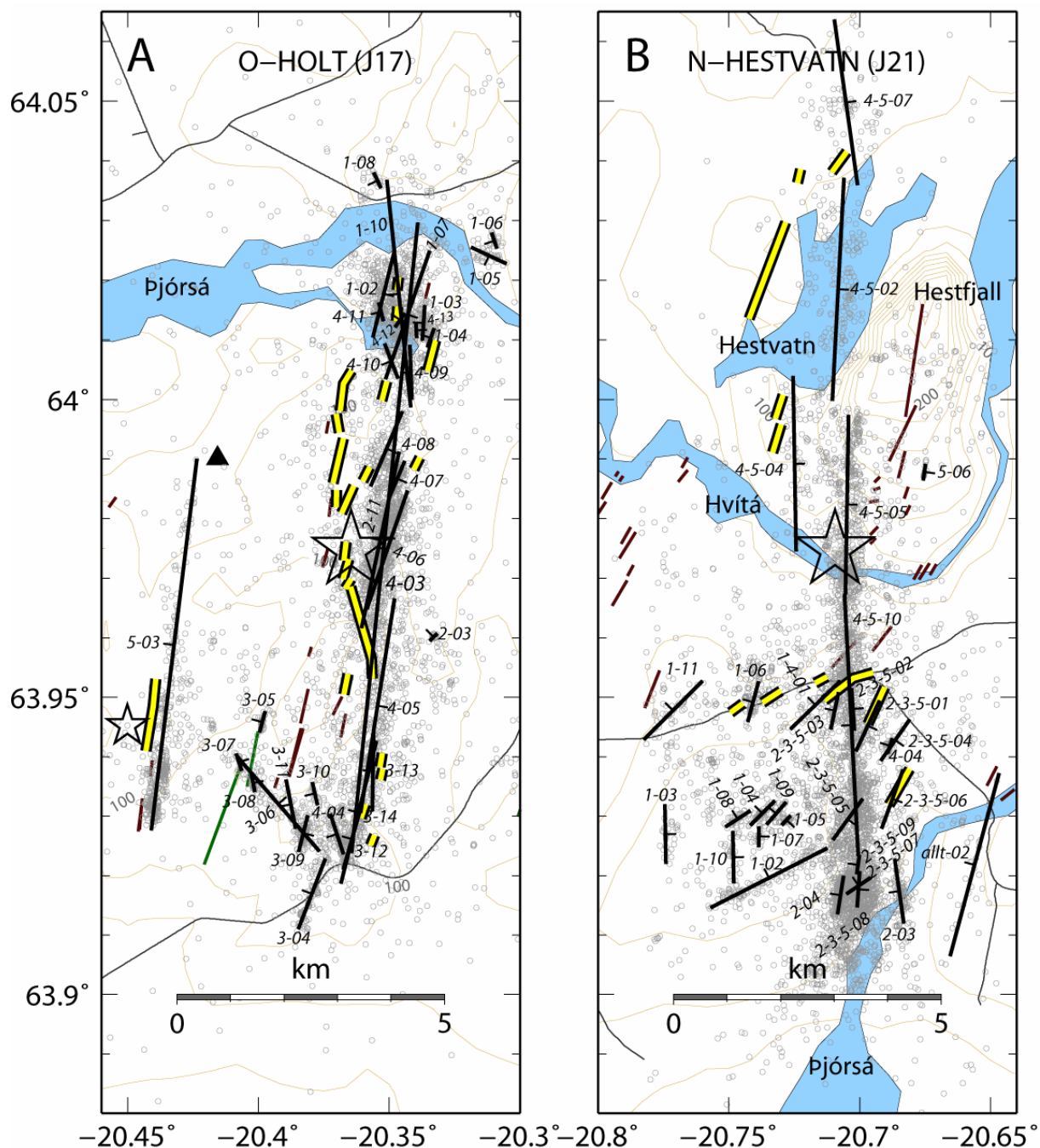
Figure 3.9. *Mapped fault segments in boxes O (A) and N (B), on the Holt and Kvíarholt faults and the Hestvatn fault respectively, drawn as black lines. Tick on either side of line denotes direction of dip. Earthquakes are shown as grey circles. Fault segments are listed in Table A.4 and Table A.5.*

3.2 Triggered earthquakes on the Reykjanes Peninsula on 17 June

The shear waves from the J17 event triggered two M~5.5 events on Reykjanes Peninsula and a third M~5 event occurred there after 5 minutes (Vogfjord , 2003; Antonioli et al., 2006). The fault planes of these three triggered events were not immediately detected within the seismicity on the Reykjanes Peninsula. However, when only relocated aftershocks with low relative error are plotted, as shown in Figure 3.10, indications of lineaments are revealed for the S-wave triggered events; one along the eastern shore of lake Kleifarvatn, the other north of lake Hlíðarvatn (shown as thick grey lines in Figure 3.10). In both cases the hypocentres are located at the northern tip of the fault planes (marked by green stars in Figure 3.10, Figure 3.16 and Figure 3.17). Figure 3.11 shows map view and a vertical cross section along strike of the Kleifarvatn fault. The rather distributed events lie on a 6-km-long fault plane, with most of them occurring in the depth interval 5.4-6.8 km. The fault strikes N10°E, dips 87° and rake-angle distribution of the fps's indicate dominant right-lateral slip with a much smaller thrust component (λ_{ave}=165-170°, see Table A.2). The models derived from InSAR and GPS modelling (Pagli et al., 2003; Árnadóttir et al., 2004) agree quite well with our observations, although the relatively located events indicate a slightly wider fault with greater dip (i.e. closer to vertical) and a combined interpretation of mechanisms and the event distribution show an accompanying thrust component instead of dip slip. Surface effects of the fault slip follow mainly the eastern and southern shore of lake Kleifarvatn (Clifton et al., 2003).
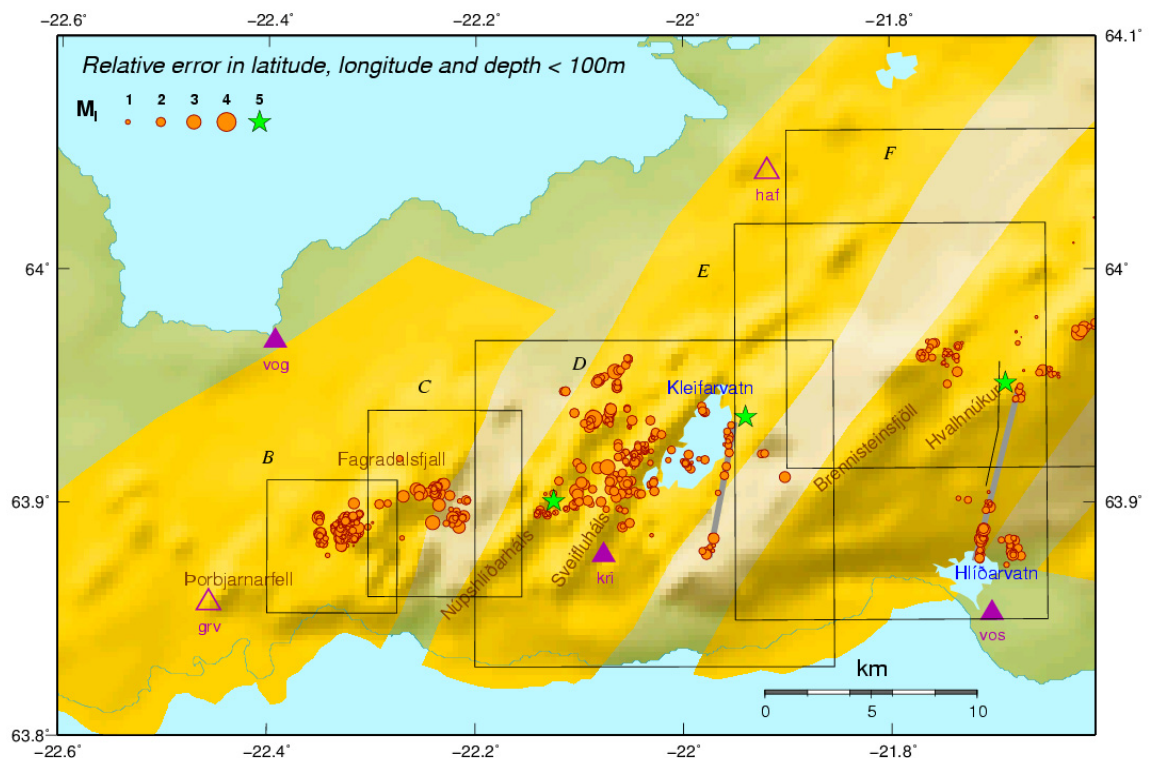
Figure 3.10. *Map of Reykjanes Peninsula. Earthquakes with relative-error median less than 100 m in latitude, longitude and depth are shown in orange, scaled according to magnitude. The hypocentres of the three triggered M~5.5 earthquakes on RP on 17 June are plotted as green stars. The thick grey lines indicate approximate locations of the fault planes for the Kleifarvatn and Hvalhnúkur events.*

The aftershock distribution on the Hvalhnúkur fault is even sparser than on the Kleifarvatn fault (Figure 3.10 and Figure 3.17). Figure 3.12 shows a vertical cross section of the events, along fault strike. The hypocentre of the main event is located at the bottom of the fault at approximately 9 km depth. The aftershocks at the northern end extend from the hypocentral depth up to 3 km. Above them a N-S surface trace of a fault striking N10°E has been mapped earlier (Erlendsson and Einarsson, 1996) (Figure 3.17). This fault probably ruptured in the M_S 6.0 earthquake of December 1968, but a M 6.2 earthquake also occurred in this area in 1929 (Tryggvason, 1973), its exact location is unknown though. A clear fault is also seen at shallower depths (3.5-5.5 km) at the southern end. Only a few events have yet been found between these two clusters. Although not contiguous, the aftershock distribution on the Hvalhnúkur fault and the Kleifarvatn fault provides valuable constraints on the fault areas of the two triggered events and their magnitudes (Vogfjörd et al., 2005b).
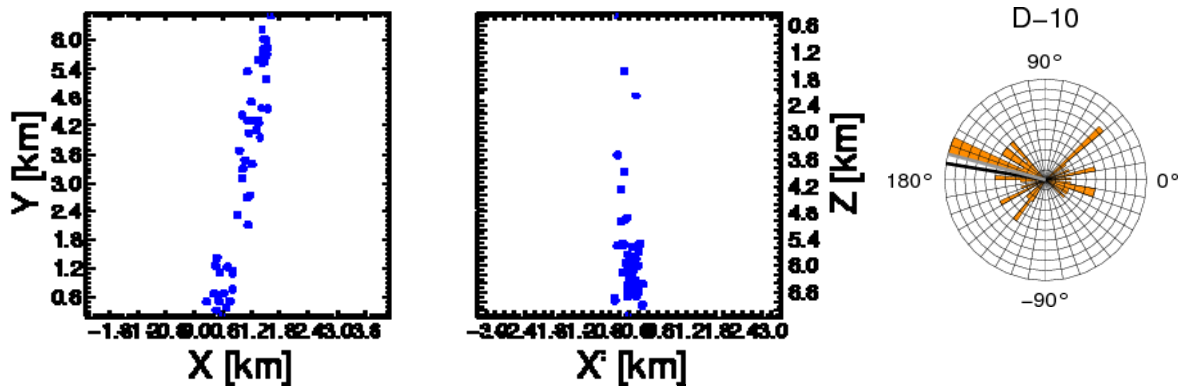
Figure 3.11. *Left: Aftershocks mapped on the Kleifarvatn fault. The dimensions of the fault in map view(X,Y) and vertical view along strike (X',Z). The 50 events define a 6-km-long, vertical fault plane. Right: rake-angle distribution for the fault. Black line denotes direction of average slip (λ_{ave}) and grey line the weighted average slip (λ_{wav}).*

The third triggered event on 17 June on the Reykjanes Peninsula occurred at Núpshlíðarháls (green star in Figure 3.10 and Figure 3.16) 5 minutes after the mainshock at 87 km distance. Its magnitude estimated from geodetic moment is Mw 5.3 (Árnadóttir et al., 2004), and thus smaller than the Kleifarvatn event (Vogfjord 2003). However, hardly any aftershocks were recorded on the fault. Surface manifestations of this event are located along the Núpshlíðarháls hyaloclastic ridge (Clifton et al., 2003), which strikes N30-35°E, and these features, as well as a geodetic model (Árnadóttir et al., 2004) indicate that the event occurred on a N-S striking fault. Furthermore, the Núpshlíðarháls event was probably triggered by the static stress changes caused by the Kleifarvatn event 4.5 minutes earlier (Árnadóttir et al., 2004).

42
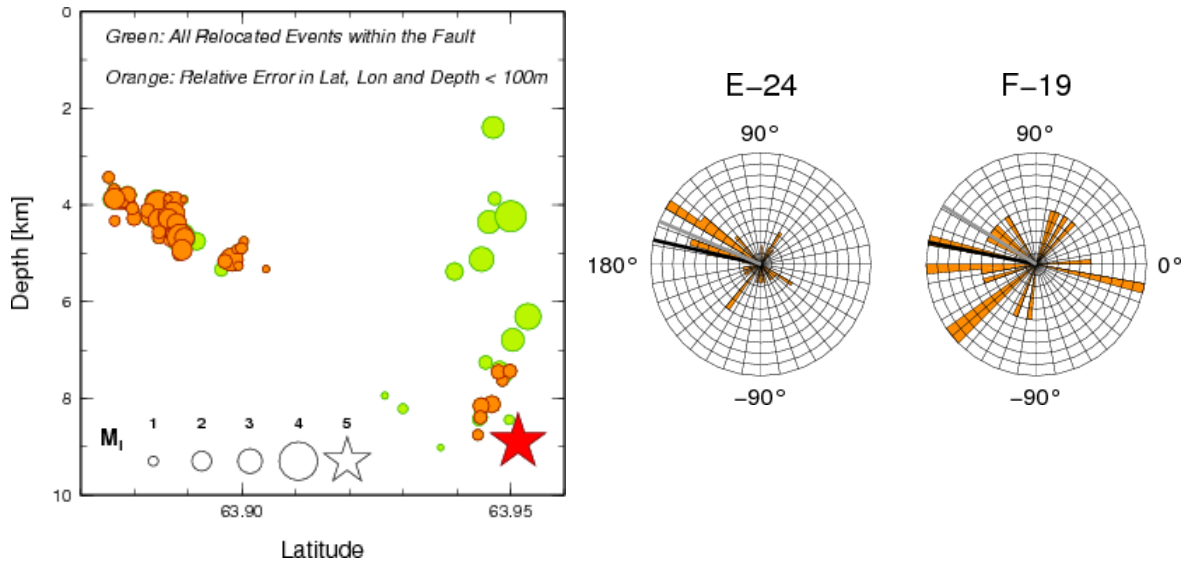
Figure 3.12. *Left: A S-N vertical cross section viewed from east, showing the aftershocks defining the dimensions of the Hvalhnúkur fault. The hypocentres of all events are shown in green, while hypocentres with relative-error-median less than 100 m in latitude, longitude and depth are shown on top in orange. Red star shows the hypocenter of the M~5.5 event at 9 km depth. Right: Rake angle distribution for the southern (E-24) and the northern (F-19) end. The location of these two segments is shown on map in Figure 3.16).*

3.3 Other faults in SW-Iceland

Numerous smaller faults in Southwest Iceland were illuminated by the increased activity in 2000 (Table A.1-Table A.3). These mapped fault segments will now be discussed in more details in alphabetical order of the areas they are mapped in (as shown in Figure 1.2), starting in the Geysir area, then from the Reykjanes Peninsula eastwards through the SISZ. A map of all sub-surface faults, fault-segments and clusters is displayed in Figure 3.26.

3.3.1 Geysir region (box A)

Immediately following the J17 earthquake, seismicity increased in the Geysir region and between June and December 2000 around 1300 earthquakes were located. This is significantly higher activity than during the preceding months, when less than 20 events were detected. Before further analysis, box A was divided into three sub-areas, A1-A3, according to the clustering of the activity. These areas are outlined in Figure 3.13 and on the overview map in Figure 2.3 which shows both routine locations (green) and relative locations (purple). The relative locations are significantly better than the routine locations and most events line up on faults instead of the former fuzzy clusters. The majority of the seismicity in A1 (350 events) and A3 (120 events) occurred in June and July, whereas heightened activity was ongoing until November in A2 (790 events). The 33 fault segments mapped in this region are shown in Figure 3.13 and fault parameters are listed in Table A.1 in appendix A and distribution of rake angles is displayed in Figure B.1.

Box A is located at the margin of the western volcanic zone, and generally the faults strike SW-NE, similar to the hyaloclastic ridges in the volcanic zone and mapped surface

fractures. An example of a fault (A2-3) was shown in Figure 2.2A. It is situated beneath the Sandfell lava shield, strikes N224°E and dips 76° to the NW, which is slightly less than the commonly observed 80°-90°-dip. A normal fault has been mapped on the surface on Sandfell (Jóhannesson et al., 1990), extending about 2.5 km north from the crater, but none in the southwestern slopes where the fault is located. The motion on the fault is mainly right-lateral, with a smaller normal component (λ_{ave}=-160°, λ_{wav}=-170°). The depth of the fault, 6.-6.5 km, is similar to the other faults located in the northern region (A2). A surface fracture has also been mapped west of lake Sandvatn, with approximately the same strike as the group of faults mapped south of the fracture.
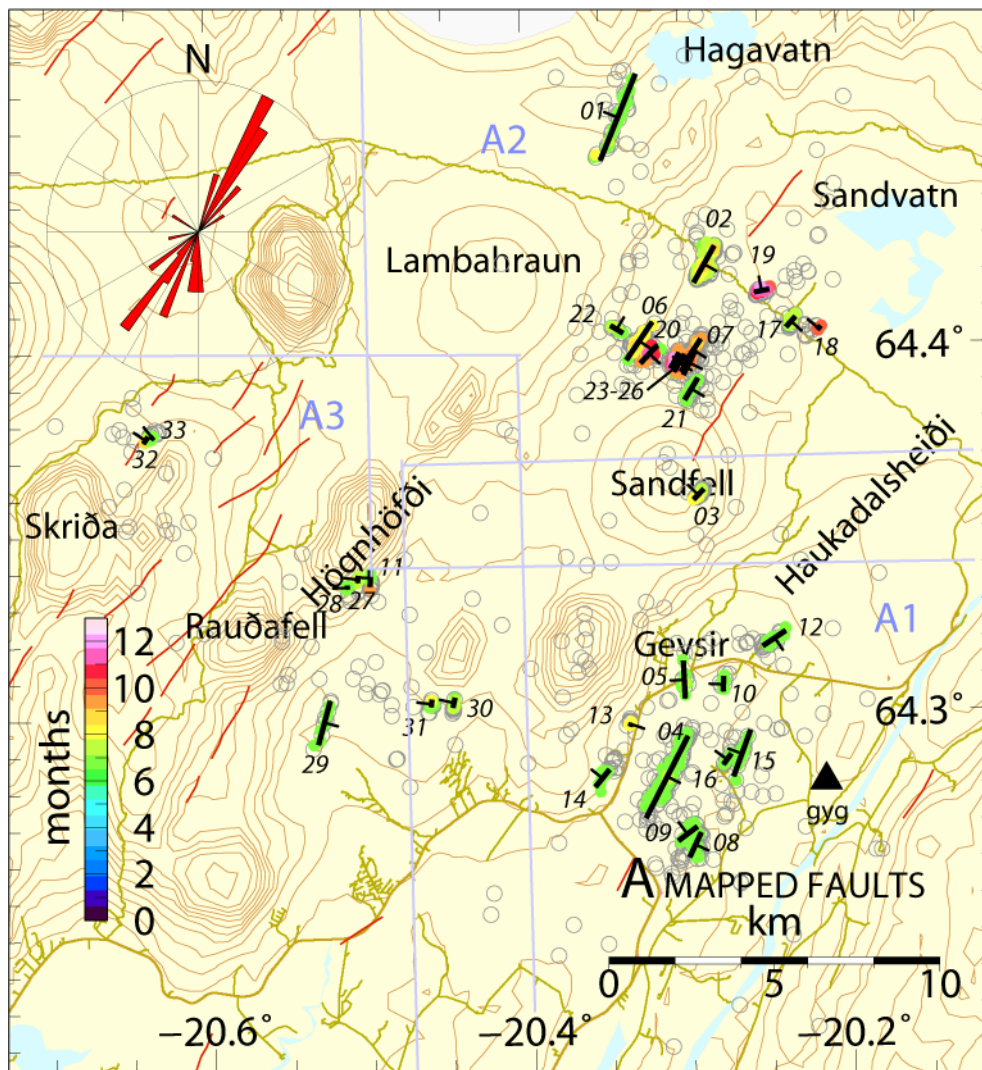
Figure 3.13. *Seismicity in box A (grey circles) and mapped faults displayed as black lines. Direction of dip is also shown. Earthquakes which define the mapped fault planes/clusters are coloured according to when they occurred. Rose diagram in upper left corner shows strike distribution. Blue lines show sub-area division. Thin, red lines display Holocene faults (from Jóhannesson and Saemundsson, 1998). The location of the Geysir geothermal area is labelled.*

No surface fractures have been mapped in the immediate vicinity of the geysers. The fault or cluster nearest to the geysers, A1-05, is only defined by seven events between 0 and 2.5 km depth. It strikes N-S and extends south from the geothermal area. Through the 3D-mapping of bedrock resistivity, a fault which intersects the surface in the location of the geysers, and extends about 4 km north-northeast-wards, has though been found. This fault, which is indicated by a low resistivity anomaly and extends from the surface down to several hundred metres depth, deepens towards the south-southwest-end. Furthermore, resistivity estimates for the depth range 600-700 m indicates a second fault striking in the same direction at the eastern margin of the high-temperature geothermal area (Karlsdóttir, 2004). These resistivity anomalies have similar strikes as the longest fault mapped in the area, A1-04, 3 km south of Geysir, and the majority of the faults in box A.

A significant difference in depth was observed between the three sub-areas, as shown in Figure 3.14. Focal depths in the immediate vicinity of the Geysir-geothermal system are well constrained, since the nearest station, **gyg**, is situated at only a few kilometres distance. Earthquakes there are very shallow or around 1-4 km, but the activity deepens farther north, to 5 -7 km in A2 and to the west in A3 (4-6 km near to mount Högnhöfði and Rauðafell). The deepest seismicity (8-11 km) is observed in the westernmost region, near to mount Skriða, where only two very short segments or clusters were observed (A-32 and 33). South-east of Rauðafell nine shallow earthquakes (2-4 km) define a 1.3 km long fault plane (A-29) which strikes north of the strike of the surface features mapped farther west, south of Rauðafell. The two small clusters 3 km farther east (A-30 and 31) are probably only a manifestation of larger faults, which do not show further activity during the observation period, as is most likely also the case for the other 100-300 m long fragments mapped in box A. Approximately 75% of faults defined by ten or more events show mainly right-lateral motion, often accompanied by a significant normal component. Pure thrust (A1-08) and pure left-lateral motion (A2-22) is also observed, but not commonly (Figure B.1).
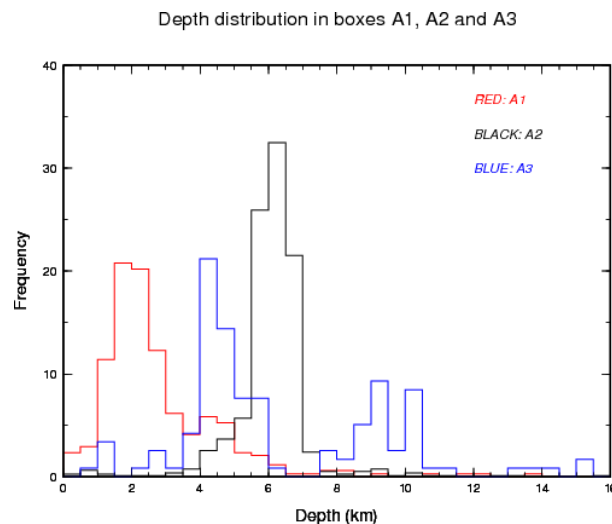
Figure 3.14. *Histograms showing different depth distribution in sub-boxes A1-A3, in the vicinity of the Geysir-geothermal system. Shallower activity is observed in the nearest vicinity of the geothermal area (red).*

3.3.2 Reykjanes Peninsula (boxes B-F)

More than 2200 microearthquakes were relocated on the Reykjanes Peninsula. In boxes C-F events recorded during the first six months of year 2000 were also analysed. During that period less than 20 earthquakes occurred within box B and therefore it was considered not necessary to include these data. In the westernmost area, in the vicinity of the low-rising table mountain Fagradalsfjall, most of the relocated seismicity took place in a swarm in November. Seismic activity is common in this area and since 1996-1997, when six new seismometers were installed on the Reykjanes Peninsula, the network's sensitivity has increased significantly (Jakobsdóttir, 1998). Nearly 5500 earthquakes were recorded near to Fagradalsfjall between 1997 and 2005, the largest two swarms occurring in 1998 and 2004. These earthquakes have been analysed and used to map nearly 30 faults and fault-segments (Hjaltadóttir and Vogfjörð, 2006), displayed as grey lines in Figure 3.15.
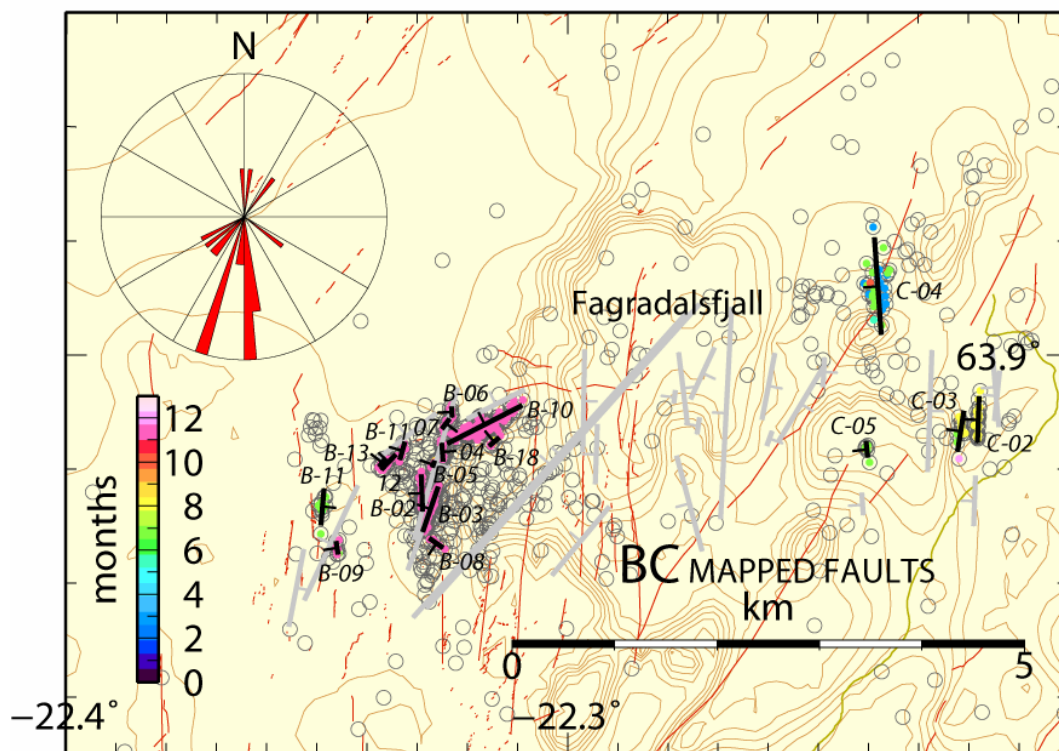
Figure 3.15. *Seismicity (grey circles) and mapped faults (black lines) in boxes B and C, Fagradalsfjall. Coloured events define faults planes. Rose diagram in upper left corner shows strike distribution. Grey lines show mapped faults based on seismicity between 1997 and 2005 (from Hjaltadóttir and Vogfjörð, 2006). Thin, red lines show mapped surface fractures (from Clifton and Kattenhorn, 2006).*

The 2000 activity reveals a system of faults beneath the southwestern slopes of Fagradalsfjall, which together form a 1500 m long lineament striking slightly east of north (B-02–B-08) and an easterly striking branch (B-10–B-13 and B-18), which extends through its northern end. Additionally two small clusters (B-9 and B-11) are observed 1 km to the west and four fault-segments (C-02–C-04) in the eastern slopes of the mountain, all striking N-S. In general the northerly striking faults show predominantly right lateral motion, whereas the more E-W-striking faults mainly exhibit left-lateral motion, but generally both are accompanied by a normal component (Figure B.2 and Figure B.3). Faults with a predominant normal component are rare but also observed, for example on

segment B-13 (normal motion and a smaller left-lateral component) and cluster B-09, which is part of a fault mapped by Hjaltadóttir and Vogfjörð (2006), which was active in July 2005. That fault also showed mainly normal displacement but mixed with a left-lateral component, and different from the mainly right-lateral motion observed on another segment just off to the south, which was active in May 2004 and has a slightly more northerly strike.
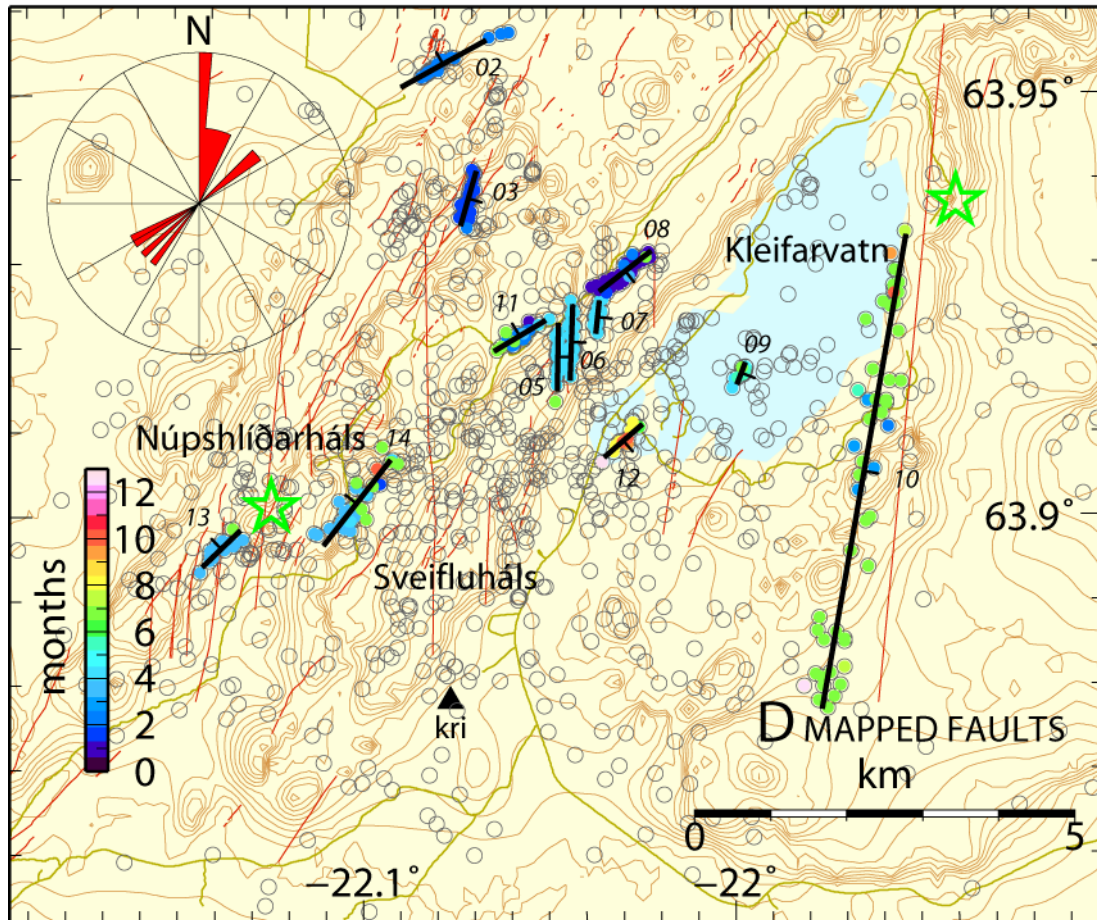
Figure 3.16. *Seismicity (grey circles) and mapped faults (black lines) in box D, in the vicinity of the Kleifarvatn lake. Coloured events define faults planes. Rose diagram in upper left corner shows strike distribution. Green stars show the location of the two M~5 earthquakes triggered at the eastern shore of Kleifarvatn and at Núpshlíðarháls within 30 s and 5 minutes respectively of the J17 mainshock. Thin, red lines show mapped surface fractures (from Clifton and Kattenhorn, 2006).*

Farther east, in box D (Figure 3.16), more activity was observed during the first six months of 2000 and several small faults active during that time are mapped, either striking SW-NE or close to north (blue events in Figure 3.16). Two small segments are seen below lake Kleifarvatn (D-09 and -12). Several mud pots are situated near to the southern segment, at the south-western shore of the lake and geothermal springs have also been observed near to the northern segment. The largest fault (D-10) mapped in Figure 3.16 is the Kleifarvatn fault, discussed above in section 3.2.

Faults mapped in boxes E and F, the Bláfjöll and Brennisteinsfjöll area, are displayed in Figure 3.17. In addition to the Hvalnúkur fault (F-25, see section 3.2), a few short

segments were also mapped in this area. Most of these strike close to N-S (Table A.2) and were active at greater depths than those farther west in box D, or between 5-9 km depth.
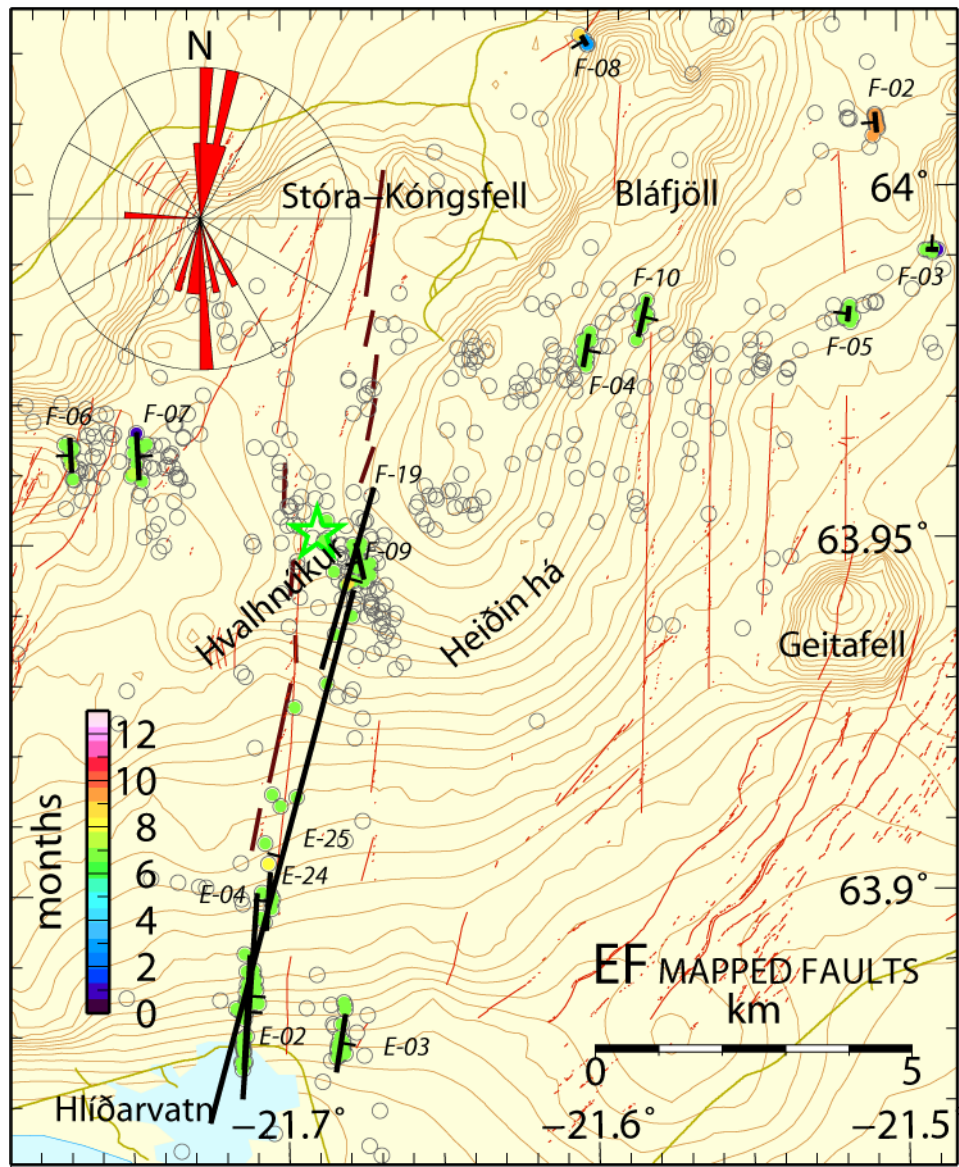
Figure 3.17. *Seismicity (grey circles) and mapped faults (black lines) in boxes E and F, in the vicinity of Bláfjöll montains and ski-area. Coloured events define faults planes. Rose diagram in upper left corner shows strike distribution. Green star shows the location of the M~5 earthquake triggered at Hvalhnúkur within 26 s of the J17 mainshock. Thin, red lines show mapped surface fractures (from Erlendsson and Einarsson, 1996, and Clifton and Kattenhorn, 2006).*

3.3.3 The Hengill area and the South Iceland seismic zone (boxes G-M)

The approximately 4400 earthquakes relocated in the SISZ and Hengill area illuminated many pre-existing fault segments. As mentioned earlier, the Hengill area experienced greatly increased seismicity during the period of magma intrusion between 1994 and 1998

(Sigmundsson et al., 1997; Rögnvaldsson et al., 1998b and 1998c; Vogfjörd et al., 2005a). The centre of uplift (marked by a red circle in Figure 3.18) was located only 3 km NNW of near-by village Hveragerði (Feigl et al., 2000). The seismicity culminated in 1998 when several M 3-M 4 and two M_L>5 events occurred (Rögnvaldsson et al., 1999; Vogfjörd et al., 2005a; Pétursson and Vogfjörð, 2009). The former large earthquake (M_L 5.5) occurred on 4 June 1998, about 5 km northwest of village Hveragerði (green star in Figure 3.18). The second event (M_L 5.2) occurred on 13 November, 9.5 km further south, only 2 km west of the seismic station at Bjarnastaðir (**bja**) (Figure 3.21). Extensive mapping of faults active during this period has revealed an overall N-S-striking fault, 15 km long cutting through nearly the entire seismic zone and which probably ruptured in the two M>5 events (filled, grey, smaller circles in Figure 3.18) (Vogfjörd et al, 2005a). The fault is composed of many left stepping segments but nearly no activity was observed on this fault 2 years later, during 2000. Only two small segments in Skálafell are observed during 2000 (Figure 3.18) but these lie west of the N-S-striking 1998 fault.
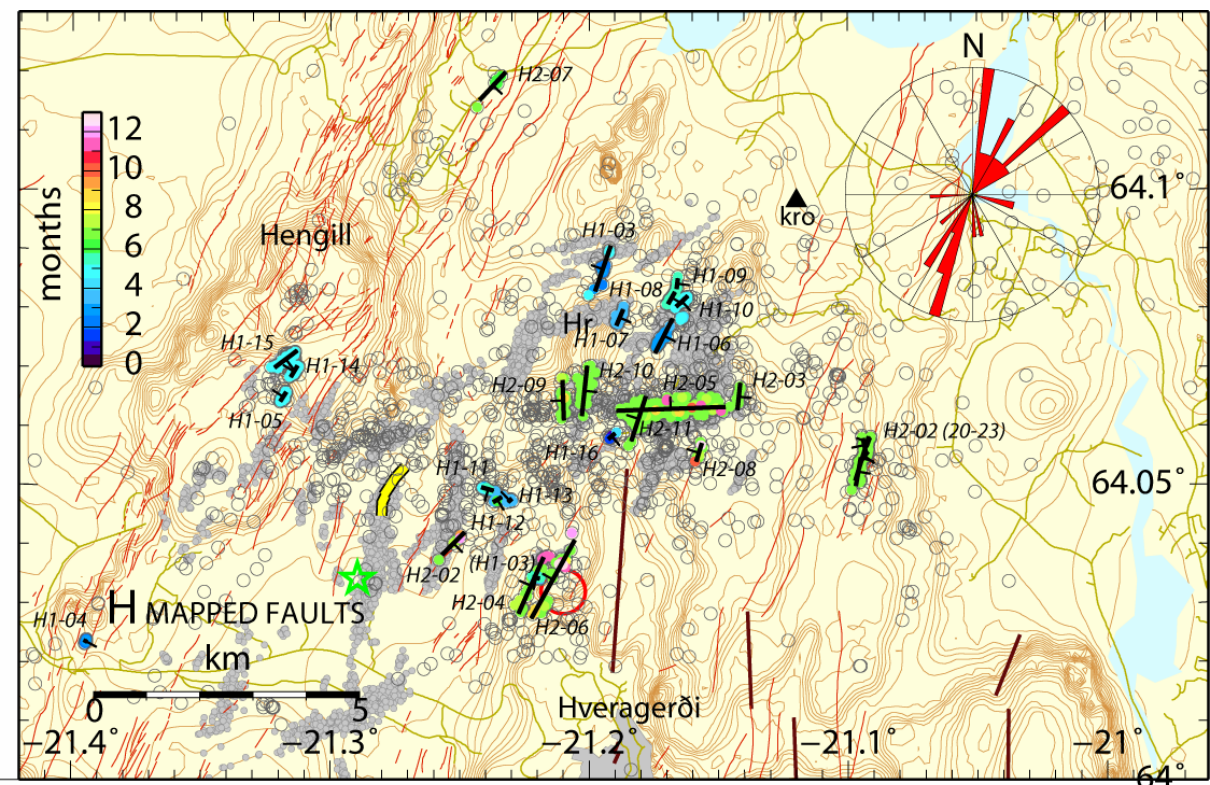
Figure 3.18. *Seismicity (open, grey circles) and mapped faults (black lines) in box H, the Hengill area. Ticks show dip direction and coloured events define the faults planes. Rose diagram in upper right corner shows strike distribution. Green star shows the location of a M_L 5.5 earthquake which occurred on June 4 1998. Red circle denotes the location of the centre of uplift detected during 1994 and 1998. Brown lines denote mapped surface faults and thin red lines mapped surface fractures and fissures (Sæmundsson, 1995). Smaller, filled, grey circles show previously mapped faults, acitve in 1997-1998 (Vogfjörð et al., 2005a). Yellow line marks surface rupture in Svínahlíð from June 1998 (from Þorbergsson and Vigfússon, 1998)*

Even though roughly 1850 earthquakes were detected in the Hengill area in 2000, it proved difficult to find clear fault traces. The largest one mapped here (H2-05) strikes E-W and was also active between 1997 and 1999 (Vogfjörd et al., 2005a). It lies in the midst of a
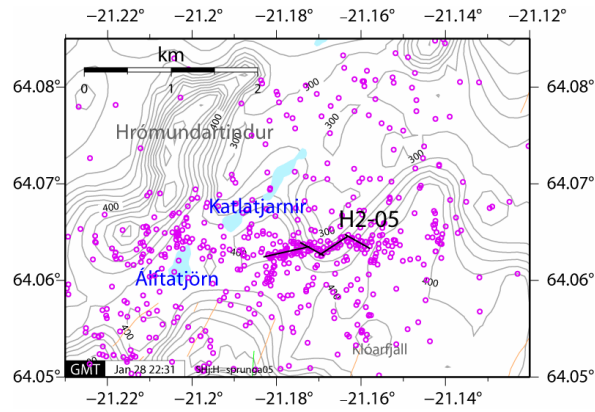
Figure 3.19. *The zigzag like structure of fault H2-05 in the Hengill area. This fault was though only interpreted as one E-W trending segment.*
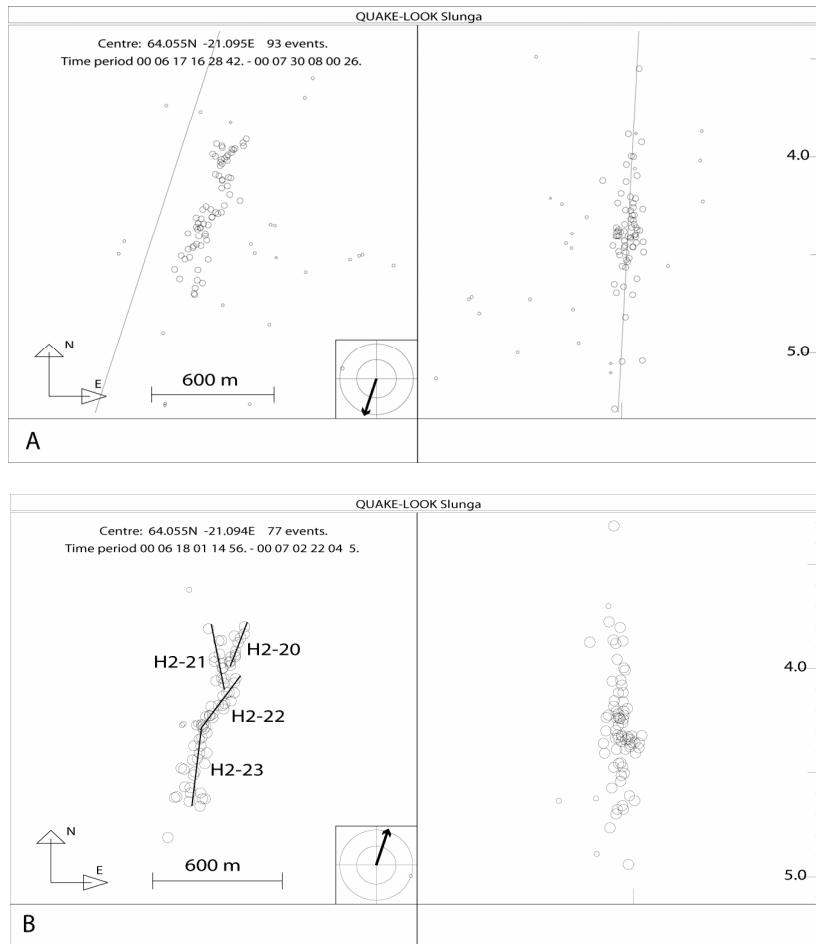
Figure 3.20. *Fault H-02 in the Hengill area after first relocation (A) and second relocation (B), where the locations in (A) were used as input. The more complicated structure of the fault becomes clearer and it seems to be composed of four segments.*

cluster of dense seismicity, located just north of the presumed 1706 and the 6 September 1896 historic faults (Figure 1.3). By further inspection one can see that the fault is made of at least four segments forming a zigzag-like pattern (Figure 3.19). Its western end is cut

through by a short N-S striking segment, H2-11. Three 1 km long faults are also seen near to this fault, two to the west (H2-09 and -10) and one 3 km to the east-southeast (H2-02). A zoom-in of the easternmost segment is displayed in Figure 3.20, which shows finer details of the fault. Two faults are visible just west of the centre of uplift (H2-04 and -06), and several very short segments are mapped around the area, with differing strikes similar to previously mapped subsurface faults in the vicinity (Rögnvaldsson, 2000).

The 1997-1999 activity also revealed a large fault striking approximately N77°E, which runs through the southern end of the 1998 N-S-striking fault and seems to be composed of many small segments with a northerly strike (Rögnvaldsson, 2000; Vogfjörd et al., 2005a). This fault is also visible in the 2000 activity, here composed of two segments (G-15 and G-16 in Figure 3.21). They are 10 km and 6 km long respectively, show predominantly left-lateral slip (Figure 3.22) and overlap north of SIL-station **bja**. This same fault also became active in May 2008, following the M_L 6.3 earthquake, which originated on a 10 km long fault beneath the western slopes of Ingjólfsfjall (hypocentre marked by a red cross in Figure 3.21) but also generated slip on a 19 km long fault 4 km farther west, running through the farm Kross, close to the village of Hveragerði (Vogfjord et al., 2009; Hreinsdóttir et al., 2009). Distributed activity is observed on the southern part of the Kross fault. Perhaps these events do not image a very obvious fault plane, but they fall within the same trace as aftershocks of the 2008 earthquake and define a 9-10 km long northerly striking fault (G-17) with a predominant right-lateral strike-slip (Figure 3.22). Two short fault segments have also been mapped in the southwestern slopes of Ingólfsfjall, where the fault slip originated on 29 May (I-19 and I-20). It is also quite possible that these events originate on the same fault plane. Segment G-05 is located just south of surface ruptures which, were formed in 1706 or in September 1896 and segments I-16 and I-07 are located beneath the surface trace of a fault which ruptured on 5 September 1896. Several short fault segments are observed close to the town of Selfoss and at least one of these segments (I-09 in Figure 3.21) showed increased activity in November 2007 (Guðmundsson et al., 2008). A 9-10 km long fault (I-21) is revealed 2 km east of the town, also mapped previously on the surface and was probably active in the earthquake on 16 August in 1784.
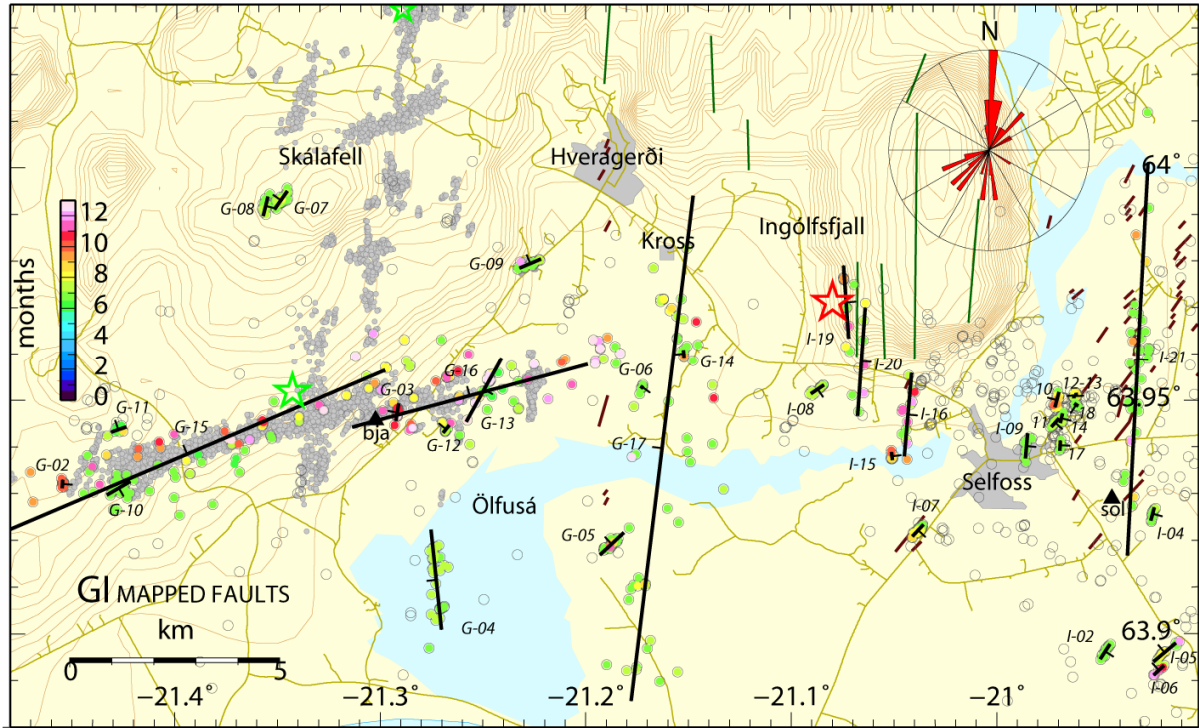
Figure 3.21. *Seismicity (grey circles) and mapped faults (black lines) in boxes G and I, Ölfus and Flói districts. Ticks show dip direction and coloured events define the faults planes. Rose diagram in upper right corner shows strike distribution. Green stars show the locations of the $M_L > 5$ earthquakes in the Hengill area on 4 June and 13 November 1998. Smaller, filled, grey circles show previously mapped faults, active in 1997-1998 (Vogfjörð et al., 2005a). Brown lines show mapped surface faults in Holocene rock and olive green lines denote faults in older formations (Einarsson and Eiríksson, 1982; Einarsson et al., 2002; Clifton and Einarsson, 2005; P. Einarsson, personal communication 2009).*
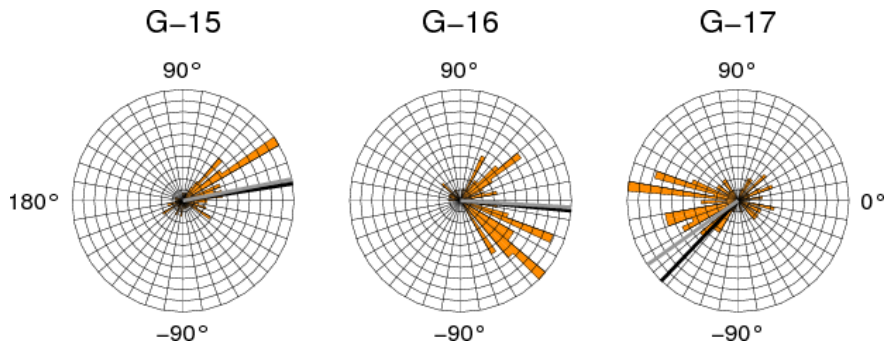
Figure 3.22. *Rake angle distribution for fault segments G-15, G-16 and G17 mapped in Ölfus district (box G). Black line shows direction of λ_{ave} (average rake vector in the common fault plane) and grey line direction of λ_{wav} (weighted average rake vector, weighted with the seismic moment of the events).*

Figure 3.23 shows a map of the few faults which were mapped south of the seismic zone (and south of the J17 and J21 faults) in box J, near to the town of Hella. Four N-S-striking fault segments are mapped 7-8 km southwest of the town and one longer NW-striking fault on the western bank of the river Þjórsá. Segments J-02–J-05 show right lateral motion accompanied by a smaller normal or thrust component (Figure B.10, Table A.3). Fault J-06, which is based on two clusters of well-located earthquakes on the western bank of river

Þjórsá, and one well located event on the eastern bank, shows an equal normal and left-lateral slip motion.
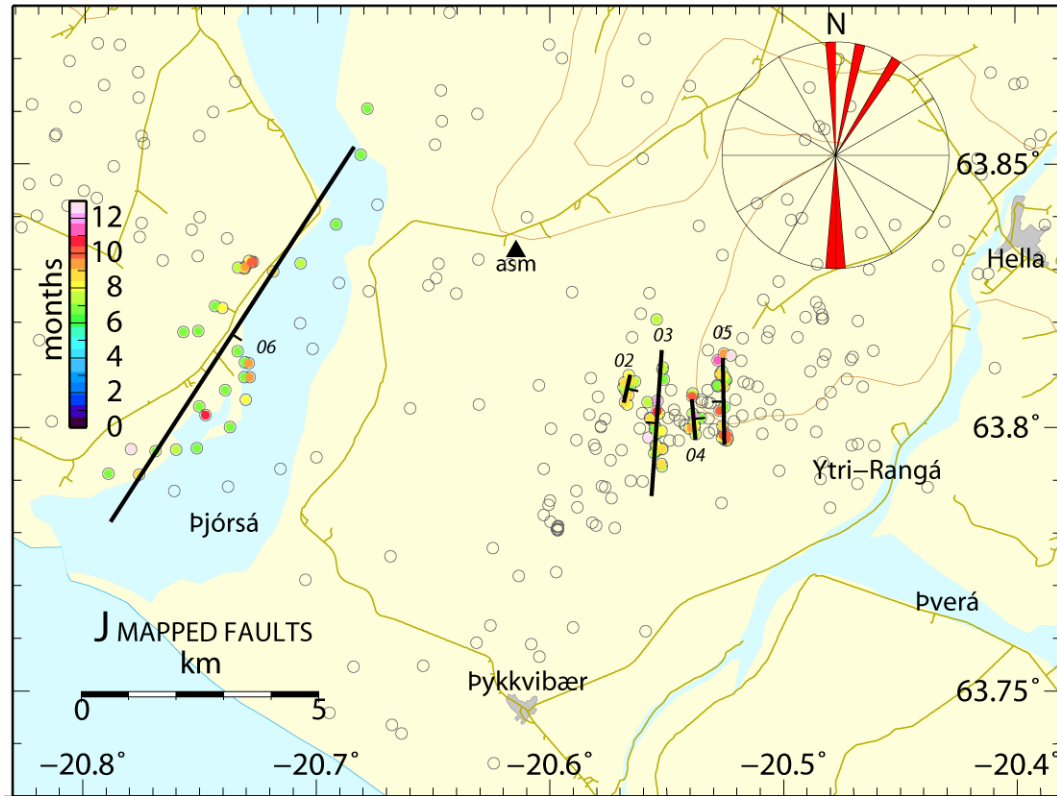
Figure 3.23. *Seismicity (grey circles) and mapped faults (black lines) in box J, near to the village of Hella. Coloured events define faults planes. Rose diagram in upper right corner shows strike distribution.*

West of the Hestvatn-fault, in box K, (Flói district, see Figure 3.24, left) several 800-1300 m long faults have been identified, some of which coincide with previously mapped surface faults. Similar to the Hengill area, this area proved quite difficult to analyse and to identify fault planes within the dense activity. Only one of the smaller clusters has been mapped (250 m long segment, K-11) but several others may also exist. An example of a mapped fault can be seen in Figure 2.2B, which shows the approximately 1.5-km-long fault section K-08 which strikes N168°E, dips 87° and has a predominant right-lateral motion (Table A.3 and Figure B.11). It is located near to a left stepping en-echelon surface rupture which was formed on 21 March in 1734. The K-10 segment, to the north, may also belong to the 1734 fault, as well as the other small fault segments mapped around the surface rupture.

Figure 3.24, right shows a map of the Skeið district (box L), which is located between the two large J17 and J21 faults (Figure 1.2). The largest lineament mapped in this box is a 6-9 km long fault (L-11 and L-12), which is also featured as a system of left-stepping en-echelon faults on the surface, extending towards Vörðufell mountain and ruptured on 5 September 1896. It is cut through by a shorter NNW-striking segment (L-02), which extends south beneath river Þjórsá. A shorter segment with a similar strike is also mapped 2 km farther west (L-03). East of the Þjórsá river a group of several northerly striking

faults are also mapped, which may show activity on the fault from the 14 August 1784 event.
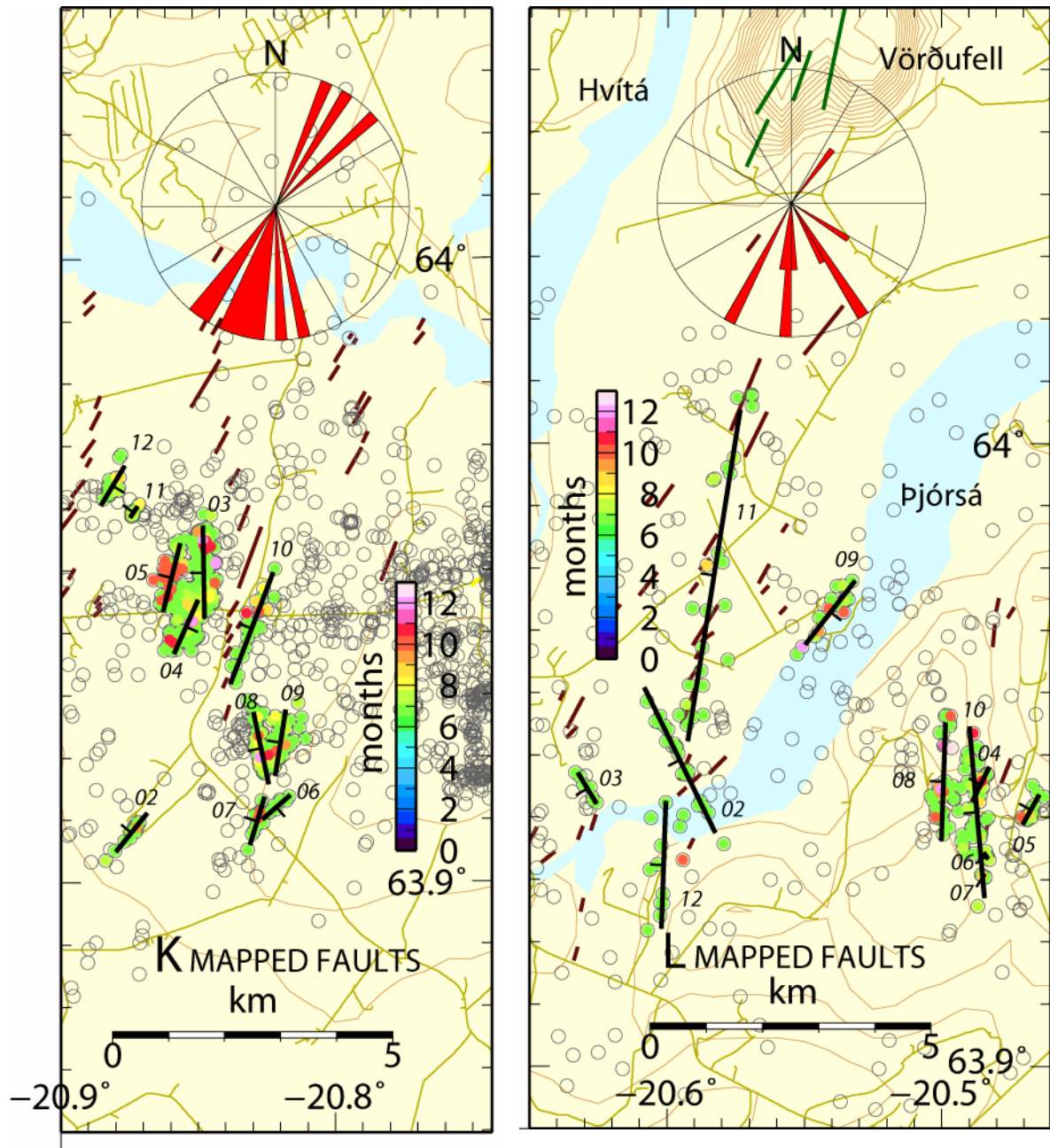
Figure 3.24. *Seismicity (grey circles) and mapped faults (black lines) in boxes K, near to Hraungerði in Flói district (left) and L, Skeið district (right). Coloured events define the mapped fault planes. Rose diagrams show strike distribution. The dense seismicity to the right of the colour scale in box K also belongs to box N (Hestvant fault) and was analysed there. For surface faults (brown and green lines) see legend for Figure 3.21.*
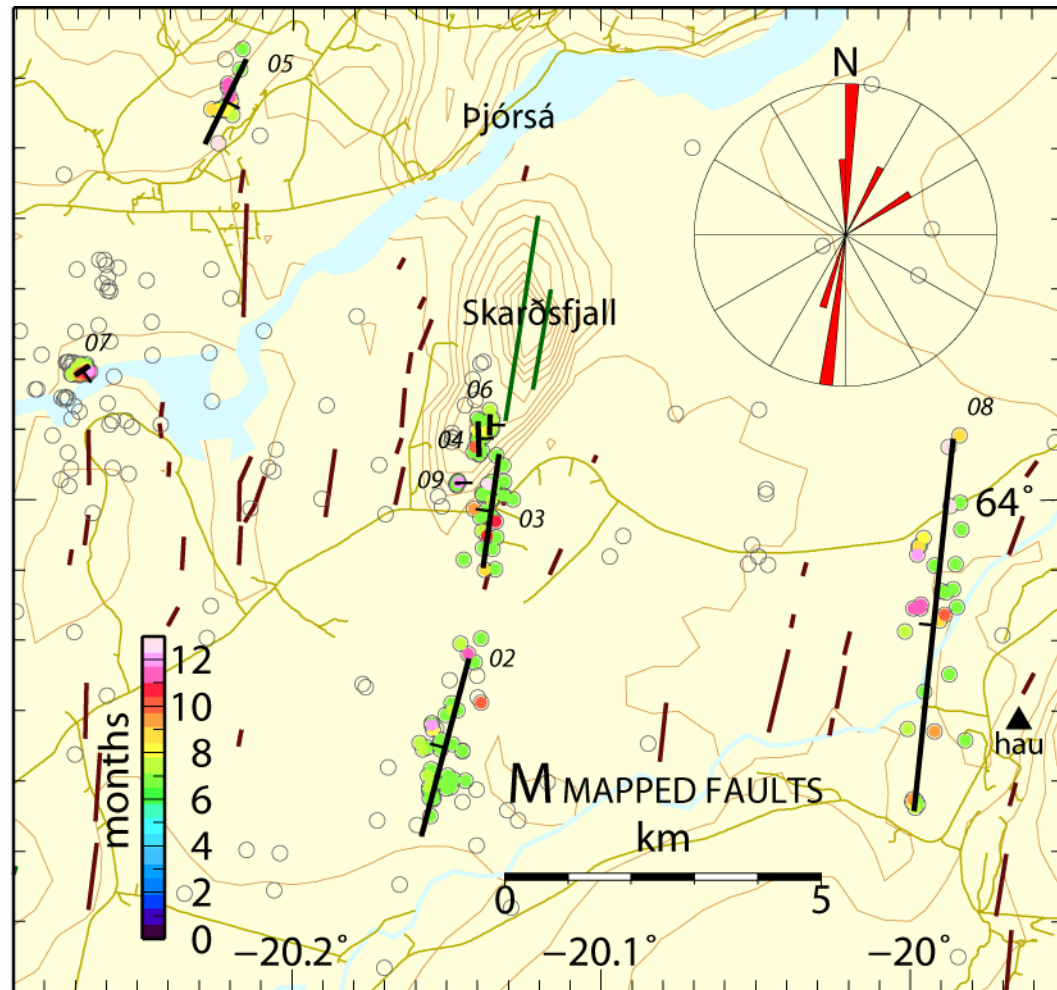
Figure 3.25. *Seismicity (grey circles) and mapped faults (black lines) in the easternmost box M, Land district. Coloured events define the mapped faults planes. Rose diagram in upper right corner shows strike distribution. For surface faults (brown and green lines) see legend for Figure 3.21.*

Only about 360 earthquakes were relocated in the Land district in box M (Figure 3.25), east of the Holt-fault. The easternmost active fault (M-08) is 6 km long and lies only 1.5 km west of the SIL-station **hau** (Haukadalur) and the mapped surface rupture (Selsund fault) of the M 7 event on 6 May 1912. The 2000 seismicity however does neither seem to occur on the Selsund fault, nor on the fault from 7 September 1732, which lies 5 km farther west. A set of faults and smaller fault segments are also visible south of mount Skarðsfjall and they probably all belong to the same fault which cuts through Skarðsfjall and ruptured on 26 August 1896. Additionally two other segments can be seen north of the river Þjórsá, presumably only illuminating a part of larger faults since both of these are situated just north of systems of mapped surface fault traces dating from February 1630 (for fault segment M-05) and from 27 August 1896 (for fault segment M-07). All the larger segments strike north or close to north and experienced predominantly right-lateral motion with a vertical component of varying size (Table A.3 and Figure B.13).

3.3.4 Active faults in 2000

During this research, about 240 faults, fault segments and small clusters, which were active during 2000, have been mapped (Figure 3.26) using relatively located earthquakes. Together the mapped fault planes form two easterly trending lineaments, one along the Reykjanes Peninsula towards the Hengill area and the other along the SISZ, and show that a large part of the plate boundary in Southwest Iceland was activated during the months following the J17 and J21 events. The seismicity in 2000 along the deactivating WVZ is restricted to the cluster near to the Geysir geothermal area, but no activity was observed southwest-wards from there. A few faults were also activated south of the transform zone, or more precisely south of the Hestfjall fault.

The average slip direction, or rake, has been determined for each mapped fault plane and is shown in Figure 3.26 by the colour of the fault. The λ_{ave} was chosen to represent the slip direction rather than the weighted average rake, λ_{wav} because it is based on fault plane solutions for several or many events, whereas one large event with incorrect phase picks can severely affect the weighted average. Faults experiencing right-lateral motion, or with a rake of ±180°, are red or purple, but faults with an average left-lateral motion, or 0° rake, are green. Also, normal faulting is shown in blue but thrust faulting in yellow-green. When average rake is examined as a function of strike, one can conclude that faults striking 350°-45° and 150°-200° have a dominant right-lateral slip component but faults striking 30°-60°, 110°-125° or 210°-275° mainly have a dominant left-lateral component. Faults with a predominant normal motion are also observed but only a few thrust-slip faults have been mapped. As expected, the largest faults in the SISZ and on the RP strike N-S and show predominantly right-lateral slip, often accompanied by a vertical component, but faults striking SW-NE to E-W and predominantly with left-lateral slip, are also found. The largest of these is located in the Ölfus district and has been mapped previously (Vogfjörd et al., 2005a), but other easterly striking faults are found for example in the Hengill area and west of the Hestfjall fault. The faults on the margin of the WVZ mostly line up along the dominant strike direction in the volcanic zone and chiefly show a combined right-lateral and normal motion.
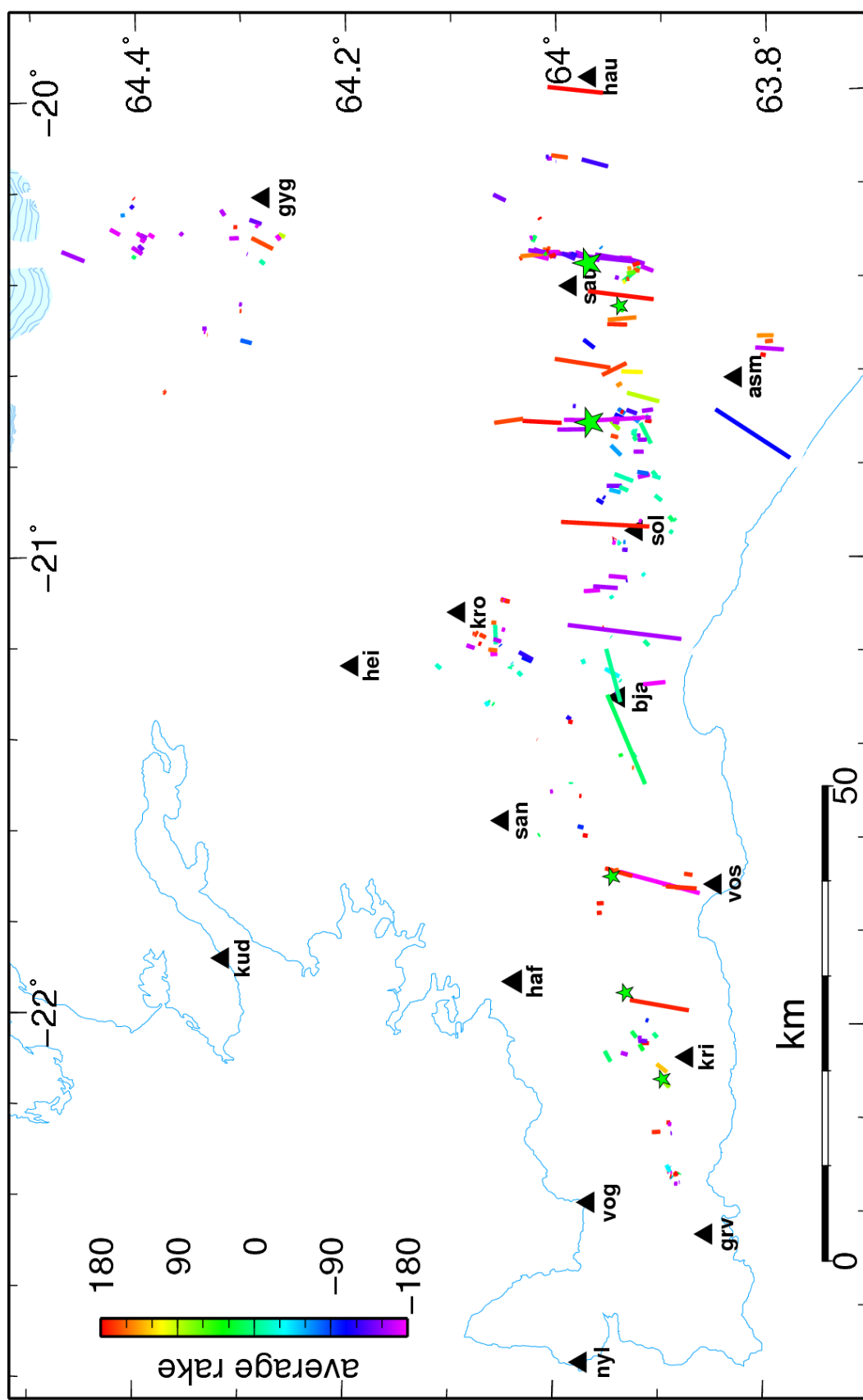
Figure 3.26. *Mapped sub-surface faults and clusters coloured according to average rake (λ_{ave}).*

57

3.4 Depth distribution, stress drop and thickness of the brittle crust

Focal depths were examined along the RP and the SISZ and were compared between different boxes. Figure 3.27 shows the relatively located events from Figure 3.1 plotted in 3D in different colours depending on their focal depth. It has been previously observed (for ex. Stefánsson et al., 1993) that earthquake activity generally extends to greater depths in the eastern part of SW-Iceland than in the west. This may both reflect increasing age and cooling of the crust as it moves farther east, away from its origin in the WVZ, and the eastward thickening of the crust, from ~15 km on the RP to ~25 km in the eastern part of the SISZ, as revealed by refraction-profiles (Weir et al., 2001; Vogfjörd et al., 2002; Bjarnason et al., 1993) and tomography (Allen et al., 2002; Tryggvason et al., 2002). However, according to the relocated data, this trend is not so obvious on the Reykjanes Peninsula, where seismicity seems to deepen westwards, in contradiction to what one would expect because of the thinning of the crust towards west. Shallower activity on the other hand is observed in areas of extensive geothermal activity, as near to Geysir (box A-A1), Kleifarvatn (box D) and Hengill (box H). The seismicity just west of the Hestvatn fault is also abnormally shallow but deepens east of the fault and from there towards south.
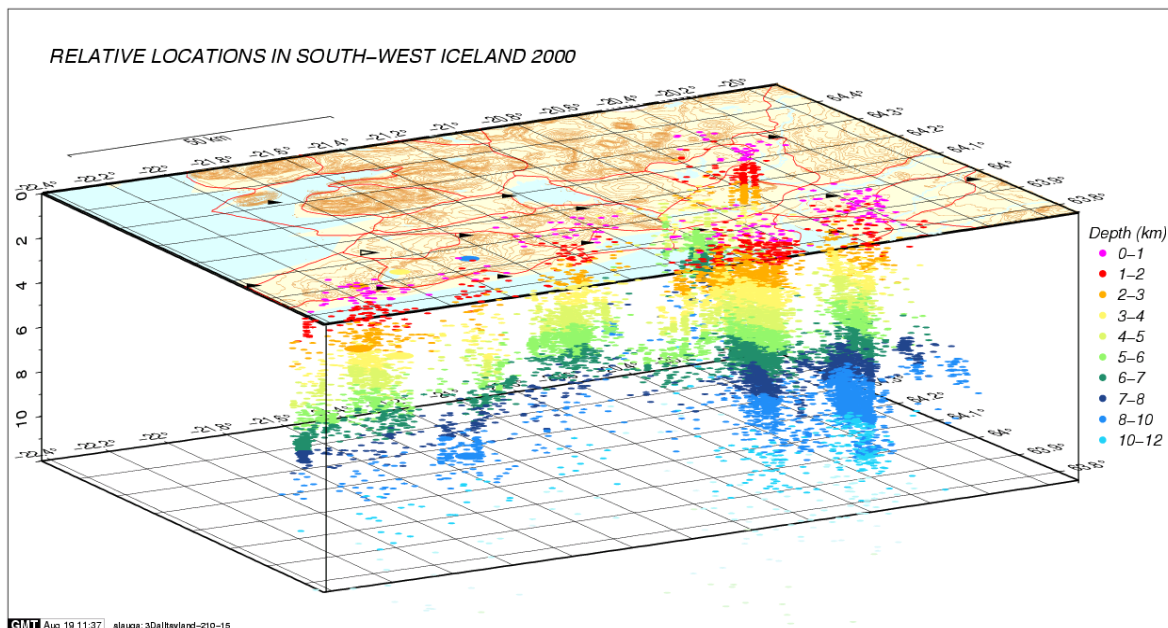
Figure 3.27. *A 3D-map showing all the relocated events. The hypocentres are colour-coded according to their focal depth. (A) A vertical N-S cross section viewed from the east. Only shows events east of 21.05°W, most recent events are plotted on top. (B) A vertical E-W cross section viewed from the south. Vertical scale is 2 times larger than horizontal scale.*

Near the end of the year seismicity on the Holt fault mainly occurred between 5 and 10 km depth, on the Kvíarholt fault between 7 and 10 km but more variable depth range was observed on the Hestvatn fault, where activity chiefly concentrated at the southern end of the fault (pink events in Figure 3.1). To investigate further the depth distribution of the

58
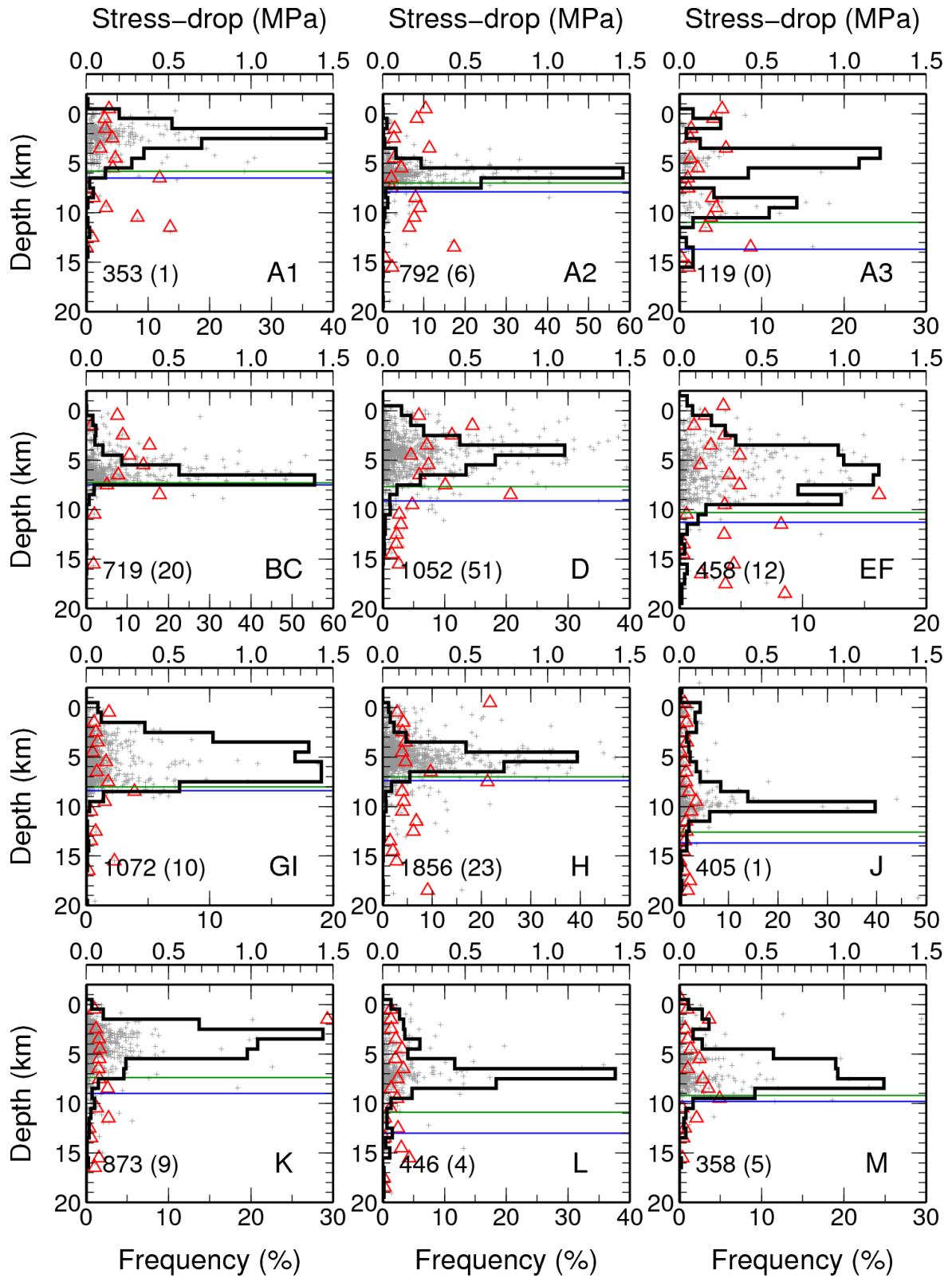
Figure 3.28. *Frequency of earthquakes in boxes A-M with respect to depth calculated in 1 km bins (black line). Stress drop vs. depth is shown as grey crosses and red triangles show average stress drop for 1 km intervals. Green and blue horizontal lines show the depth above which 95% and 97% of events occur respectively. Number of events is displayed in lower left corner. Stress drop below 1.5 MPa is only plotted. Numbers in parentheses show the number of events per each box having stress drop larger than 1.5 MPa.*
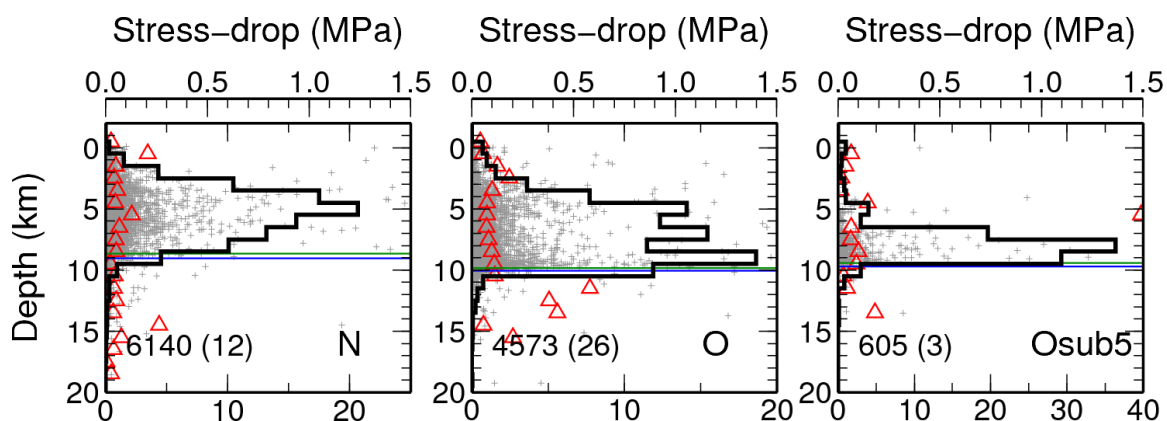
Figure 3.29. *Frequency of earthquakes on the Hestvatn fault (N), the Holt fault (O) and the Kvíarholt fault (Osub5) with respect to depth, stress drop and average stress drop, same scheme as in previous figure.*

seismicity, earthquake frequency was plotted with respect to depth in 1 km bins for boxes A-M (Figure 3.28) and the larger faults (Figure 3.29). Data were joined in boxes B and C, in E and F, G and I, Nsub1-Nsub5 and Osub1-Osub4.

The depth of maximum frequency of earthquakes is also known as the characteristic depth (Iio, 1996). As previously mentioned above, very shallow seismicity is observed near to the Geysir geothermal area (in box A1), where the characteristic depth (CD) is at 2 km but many events occur between 0 and 5 km. The activity deepens both to the north (box A2; CD=6 km) and west (box A3) where there are two frequency maxima. The shallower one (CD=4-5 km) is within approximately 10 km distance west of the geothermal area, whilst the deeper one (CD=9 km) is farther to the northwest. On the Reykjanes Peninsula, the activity is considerably deeper farthest west, below Fagradalsfjall (CD=7 km) than near to Kleifarvatn (box D), where the characteristic depth is at 4 km. In boxes E and F there are two frequency maxima, the smaller and lower one represents seismicity near to the Hvalhnúkur epicentre and in Brennisteinsfjöll a few kilometres to the west-southwest, and the larger one at 6-7 km includes seismicity in Bláfjöll and events on the southern end of the Hvalhnúkur fault, at lake Hlíðarvatn. The characteristic depth is shallower in the Hengill area (box H; DC=5) than to the south in the Ölfus-district, (box GI; DC=6-7 km), and hypocentres become shallower in the eastern part of box I, in Flói district near to Selfoss, where DC=4-5 km, similar to the Hengill seismicity. Going farther eastwards along the seismic zone, the characteristic depth near to Hraungerði in Flói (box K, west of the Hestvatn fault) is more shallow than was expected (3 km). But between the two large fault planes the previously observed deepening occurs and in box L, CD=7km is found and east of the Holt fault (box M), near to the eastern volcanic zone, CD=8 km. Even deeper value is observed south of the SISZ, in box J (CD=10).

As described earlier, the existence of the low-temperature geothermal system at Geysir has a pronounced effect on focal depths within the area. The measurably shallower activity in the vicinity of Kleifarvatn is probably also related to the geothermal activity, but geothermal manifestations are widely seen in the area, not only at the lake but also to the west in northern Núpshlíðarháls (Sog, Trölladyngja) and to the southwest, at Krýsuvík. The same also applies to the Hengill area, where two active volcanic systems, Hengill and Hrómundartindur, emit heat to associated geothermal systems (Sæmundsson, 1992). Warm

springs are also situated near to Selfoss (Sæmundsson and Einarsson, 1980), close to the fault segment I-09 beneath the town at 3-4 km depth, as well as between Ölfusá river and SIL-station **bja** (box G), near to which focal depths are mainly between 4 and 8 km depth and the shallowest fault, G-04, is active between 3 and 5.5 km depth. These results are in good agreement with previous findings of Sibson (1982) and with indications that aftershocks in "warmer" areas occur at shallower depths (Meissner and Strehlau, 1982).

Although stress drop is considered approximately constant, and is on average 3 MPa for large (M>6) interplate events (Lay and Wallace, 1995; Kanamori and Anderson, 1975), it can vary. Because higher stress drop means that larger stress is released per fault length, one can conclude that higher stress drops would occur at the depth of the maximum crustal strength. To investigate the relation between earthquake focal depths and crustal strength the stress drop was also plotted as a function of depth in Figures 3.27 and 3.28. Stress drop for earthquakes detected by the SIL-network is calculated automatically, assuming a circular fault, according to the relation

$$\Delta\sigma = \frac{7}{16}\frac{M_o}{r^3} \qquad\qquad (5)$$

by Brune (1970, 1971). The observed stress drop for most of the microearthquakes in the dataset is 1-2 orders of magnitude lower than previously observed for large events. Still stress drops above 1 MPa are observed. A trend of heightened average stress drop is observed in some areas, but over a broad depth interval, such as in GI, J, L and also possibly in D and N. In these five areas the peaks lie near the CD. This trend is however rather weak, and not as pronounced as has been observed in the thicker crust beneath the Eyjafjallajökull volcano, S-Iceland (Hjaltadóttir and Vogfjörð, 2009c) and is therefore not examined further.

A three-layered rheological model for the crust has been suggested, where the brittle-plastic transition does not occur abruptly at a certain depth but rather in a transitional or semi-brittle layer (Scholz, 1988; Strehlau, 1986). According to these models, maximum strength either increases into the semi-brittle layer (Scholz, 1988) or is assumed to be at the brittle-semi-brittle boundary (Strehlau, 1986). It has been inferred that the maximum strength of the crust occurs at the CD (Iio, 1996), making determination of the CD a way to measure the thickness of the brittle crust. Another way of estimating the thickness of the brittle crust is to find the cut-off depth, above which the majority of the seismicity occurs (for example Sibson, 1982; Tryggvason et al., 2002; Ágústsson and Flóvenz, 2005). The limits above which 95% and 97% of the seismicity occurs are also shown in Figure 3.28 and Figure 3.29 by green and blue horizontal lines respectively. In 7 out of the 15 cases the 95%-cutoff depth coincides or lies just below the peak of maximum frequency. In the other 8 the 95%-cutoff depth lies up to several kilometres below the CD. This applies e.g. for the Geysir geothermal area (A1), the geothermal Kleifarvatn area (D) and partly to Bláfjöll-Brennisteinsfjöll (EF). This however does not particularly apply to the Hengill geothermal area where the difference between the cut-off depth and the CD is only 1-2 km.

The relocated event distribution does not clearly show thinning of the brittle crust on the westernmost part of the seismically active RP. In contrast to what was expected, the westernmost cluster located beneath Fagradalsfjall, is located deeper than the activity just east of Fagradalsfjall (Figure 3.1). As mentioned earlier, the activity near Kleifarvatn and

Krýsuvík is mostly rather shallow, probably due to the geothermal activity in the region. Farther east, on the RP, deeper activity is again detected at the Hvalhnúkur fault and in Bljáfjöll, where Tryggvason et al. (2002) also observe a thickening from 6 km to 7 km of the brittle crust. A rather abrupt thickening of the brittle crust then seems to occur between 20.8°W and 20.6°W, or near to the Hestfjall fault There the majority of the seismicity west of the fault (box K) occurs between 2 and 5 km depth, while east of the fault (box L) it occurs between 6-9 km depth. These observations are in good agreement with the findings of Tryggvason et al. (2002), who observed a thickening from 7 to 9 km of the brittle crust approximately between 20.7°W and 20.5°W, and with SIL-data recorded between 1991 and 1994 (G. B. Guðmundsson and R. Stefánsson, unpublished manuscript, 2000). The two large earthquakes, J17 and J21, originated in the upper brittle crust but they caused rupture down below the normal limit of earthquake nucleation, into the semi ductile part. Hence, aftershocks on their fault planes do not correctly reflect the general depth distribution of microseismicity in the crust at their location (Strehlau, 1986; Scholz, 1988) and therefore should not be used to estimate the thickness of the brittle crust. However, the earthquakes did not induce seismicity farther eastwards near station **hau** (see Figure 3.1), where an old fault was activated at 8-9.5 km depth. An estimation of a ~10 km thick brittle crust in the easternmost SISZ is in good agreement with the previous estimation of Tryggvason et al. (2002). Similar to Ágústsson and Flóvenz (2005) a thickening is also observed south of the seismic zone, in box J, where cut-off depth is approximately at 13 km depth.

4 Discussion

Although the nature of the South Iceland seismic zone is left-lateral motion on an E-W trending transform zone, it is now widely accepted that rupturing along this transform zone takes place on a series of approximately N-S-striking faults (Einarsson et al., 1981). It has though been argued that they must both be longer and more densely spaced than previously revealed by mapped surface ruptures to account for the moment release rate expected for an E-W fault through the seismic zone (Hackman et al., 1990). The map of sub-surface faults presented in this thesis (Figure 3.26) shows that the aftershock activity on the two June 2000 faults indicates longer fault planes for large earthquakes than surface ruptures have hitherto revealed. Furthermore, many small segments and clusters are observed, both near previously mapped surface ruptures as well as between them. Although only small segments are illuminated by the 2000 aftershock activity, these segments are considered to be manifestations of old and much larger fault planes which only show partial activity. This type of fault mapping at Fagradalsfjall, RP (Hjaltadóttir and Vogfjörð, 2006) and near Prestahnúkur, WVZ (Hjaltadóttir and Vogfjörð, 2009a), using 10-17 years of seismological data, has for example shown that different parts of faults can be activated during different swarms. Here, spacing between mapped fault segments can range from a few kilometres down to less than one kilometre. Thus, the data presented here support the hypothesis that the bookshelf-structured SISZ can indeed act as an E-W transform fault.

Despite the fact that major earthquakes take place on N-S-striking faults, easterly striking surface ruptures have previously been identified within the seismic zone. The most recent events are from 2000, the conjugate Bitra segments which extended westwards from the Holt fault (Angelier and Bergerat, 2002; Clifton and Einarsson, 2005). Older conjugate surface ruptures are also found, for example at ~20.83°W, where a N62°E and N90°E striking conjugate fault extends at least 600 m eastwards from the main fault, which probably ruptured in 1734 (P. Einarsson, personal communication 2009) (not shown on map in Figure 3.24, but approximately at location of segment K-10). In this study we have observed several westerly striking sub-surface faults. The largest one, located in Flói district (also mapped by Vogfjörd et al., 2005a) is made of two offset segments (G-15 and G-17) with a combined length of 14 km and strike ~N75°E (box GI, Figure 3.21). A set of conjugate faults extending WSW from the Hestvatn fault have also been mapped (box Nsub1, Figure 3.9), as well as a roughly 2-km-long N268°E striking fault in the Hengill area (also mapped by Vogfjörd et al., 2005a) (box H, Figure 3.18). Mechanisms for events on these westerly striking faults indicate predominantly left-lateral displacement (Figure B.6, Figure B.14 and Figure B.8 respectively).

The previously mapped surface faults are structured in a series of *en echelon* segments, many of which align along the observed sub-surface faults in the upper crust. The relocated event distribution shows a complicated fault pattern at depth on different scales which are similar to those previously mapped on the surface. As an example, the Holt fault shows a left stepping *en echelon* pattern on a scale of several kilometres (Figure 3.3). Also, the parallel surface ruptures observed on the surface at the northern end of the 1912 Selssund

fault (Einarsson and Eiríksson, 1982; Bjarnason et al., 1993) are comparable to the parallel fault pattern at the northern end of the Holt fault at depth, as well as observed at the surface.

The average slip direction on the central part of the Hestfjall fault, estimated from joint interpretations of aftershock mechanisms and mapping of the fault, is -165° (Table A.4 and Figure B.14) indicating a small normal component. This agrees with the -167° slip direction of the major double couple in the Global CMT solution. However, the only surface evidence that indicates that normal slip may have occurred on the J21 fault were found at the Dælarétt segment, 6-7 km south of the epicentre (Clifton and Einarsson, 2005). No subsidence was observed on the surface near the epicentre of the Holt fault, but average slip direction on the fault's centre patch and at its bottom, as estimated from the aftershock mechanisms, indicates a slip angle of -151° to -152°. This suggests a slightly larger normal component than indicated by -164° slip direction of the major double couple in the Global CMT solution, but is approximately within acceptable error ranges. These results therefore show, that mechanisms of large events can be estimated from focal mechanisms of aftershocks located around the hypocentre of the large events.

The fault plane solutions used in this research are double-couple solutions and hence do not assume a volumetric change. Therefore, it is not possible to estimate a volumetric component of the motion on a fault, but by examining the relative size of the vertical component of slip in the double-couple solutions, or the orientation of the P- and T-axes, an estimate of an extensional- or compressional factor can be obtained.

The aftershock distribution is generally sparse where slip models show maximum slip on the faults. The trend of the aftershocks on the faults seems to follow the edges of the slip plane inferred from the geodetic data inversion. Away from the faults the aftershocks concentrate in areas of positive changes in CFS (Árnadóttir et al., 2003). Since only data from 2000 is analysed in this study, the decay of aftershocks is not investigated, nor the change in aftershock distribution in the long term. The post-seismic deformation observed by GPS and on short-scale radar interferograms is explained by different dominating processes in different time scales: For the first 1-2 months following the earthquakes the poro-elastic rebound model agrees well with the compressional- and extensional quadrants- type pattern observed by InSAR, and also fits well to observed changes in boreholes in the vicinity, in both water-level (Jónsson et al., 2003) and radon (Einarsson et al., 2008) during the postseismic period. In the terms of 1-4 years the smaller scale deformation observed by GPS can be explained by either afterslip or viscoelastic relaxation of the lower crust and upper mantle (Árnadóttir et al., 2005). While the modelled afterslip between 2000 and 2001 is mainly at 8-14 km depth on both faults, the afterslip during 2001-2004 extends deeper into the crust.

To some extent the relocation method decreases location errors caused by the difference between the real velocity structure of the Earth and the applied velocity model. However, recent fault mapping in Hellisheiði (Hengill area), where the effect of different velocity models were tested, have shown that different velocity structures can move source depths by up to a few kilometres and horizontal location of faults by a few hundred meters (Vogfjörð and Hjaltadóttir, 2007; Hjaltadóttir and Vogfjörð, 2009a). So, the knowledge of the velocity structure is even more important than was previously assumed. The comparison of different velocity models in section 1.4 showed that crustal velocities on the

Reykjanes Peninsula are somewhat higher beneath 3 km depth than in the SIL velocity model. The effect of a slower velocity model on the relocation process would be to move earthquakes deeper into the crust to account for the observed travel times. With the majority of earthquakes on the peninsula occurring below 3 km depth, actual focal depths may be somewhat shallower than this study indicates. Thus, more extensive fault mapping in SW-Iceland must not only make use of all available seismological data, but also include testing of the effect of different velocity models available for the area.

5 Conclusions

The use of a double-difference relative relocation method to improve location accuracy of the aftershocks following the two $M_L{\sim}6.5$ June 2000 earthquakes in the SISZ has revealed sub-surface fault patterns in Southwest Iceland, most of which have hitherto not been mapped. Many of the large historical faults in the SISZ experienced localised but distributed activity, but generally not enough to map their outlines, since in most cases only small sections on each were activated. However, taking advantage of the surface mapping already performed, many can be inferred. The two fault planes of the 29 May 2008 earthquake are also observed in the dataset.

Similar to what has been observed on the surface, the activity reveals in many cases more complicated sub-surface fault patterns at different scales, varying from several hundred metres to several kilometres. These finer details can be attained by re-applying the relocation procedure on selected faults. In agreement with previous findings, the largest mapped faults in the SISZ trend N-S, and several smaller segments form N-S trending, *en echelon* lineaments. But this study has also shown that at least three several kilometres long ENE-WSW striking faults exist in the SISZ and one of these has shown repeated activity during the ongoing sequence of major earthquakes in the seismic zone.

The mapping reveals the finer structural details of the two main faults, J17 and J21, and shows an interesting difference in character between the two. The Holt fault, of the J17 event, is approximately 12.5 km long and 10 km deep. It is nearly vertical, has an overall strike of 7°E and is broken up into three main sections, with each section striking a few degrees east of the overall fault strike. The trace of the 15.5-km-long Hestfjall fault, on the other hand, is more linear, even though the fault is made up of two differently dipping sections, which form a wedge approximately 1 km north of the hypocentre. At the northern end the fault is about 7 km deep but deepens to 10 km at the southern end. Its strike is 179°E and the southern section dips ~88° to the west, while the dip on the northern section is ~77° to the east. Furthermore, large conjugate faults were active west of the J21 fault, extending as far as 2-3 km to the west. Both faults bend slightly westwards at their southern tip. Teleseismic waveforms of the two large events reflect the difference between their fault structures. The estimation of focal mechanisms for the two large events, using joint interpretation of event distribution and aftershock mechanisms, is comparable to the major double couple part of the Global CMT solution.

Many smaller faults in the SISZ, the RP and at the eastern margin of the WVZ have also been mapped. These show predominantly right lateral motion on north- or north-easterly striking faults, often accompanied by a smaller vertical component. However, a deviation from this trend is seen in some areas, where WSW-ENE striking faults with a left-lateral movement are also observed. Faults which were mapped near to the WVZ (Geysir region) are generally more SW-NE trending compared to faults further south in the SISZ. Furthermore, this trend is in agreement with previously mapped surface faults in this region.

Aftershock activity on the fault planes of the two S-wave triggered earthquakes on Reykjanes Peninsula has given valuable information for estimating the fault sizes of the two events. The earthquakes, which occurred within the first minute after the J17 event, were obscured and distorted by the previous event, making estimation of their size and mechanism problematic by other means. The Kleifarvatn fault is vertical, roughly 6 km long and nearly 7 km wide. The majority of the aftershocks are concentrated along the bottom of the fault up to approximately 5.5 km depth. Seismicity on the Hvalhnúkur fault is more uneven but its estimated length is 10 km and its width increases from 4-5 km at the southern end to about 9 km at the northern end, where the rupture initiated.

Near the end of 2000, seismicity on the Holt fault mainly occurred between 5 and 10 km depth, on the Kvíarholt fault between 7 and 10 km but more a variable depth range is observed on the Hestvatn fault, where activity chiefly concentrated on the southern end of the fault. Shallower focal depths are generally observed in areas of extensive geothermal activity, as near to Geysir, Kleifarvatn-Krýsuvík and Hengill. The seismicity just west of the Hestvatn fault is surprisingly shallow but deepens east of the fault and also from there to the south. An abrupt thickening of the brittle crust occurs where the Hestfjall fault cuts through the crust, or between 20.8°W and 20.6°W. The depth distribution of the relocated seismicity shows that the brittle crust is 7-8 km thick on the western RP, about 10 km thick in the easternmost seismic zone, but 13 km thick south of the seismic zone. Focal depths on the RP might be overestimated because of use of the SIL-model for relocation, which is slow below 3 km, compared to velocity models derived for the RP.

In general, the research presented in this thesis shows that high-precision event locations based on waveform correlations is an excellent tool to map the finer details of active sub-surface faults in the brittle crust. Such mapping requires a dense network with a low detection threshold and a high clock accuracy, like the **SIL** network. A well-known velocity model also helps improve the results. This study reveals the detailed structure of two major faults in the SISZ, as well as numerous other smaller fault sections and clusters, many of which are probably manifestations of larger faults which show localised but distributed activity. Further mapping, which makes use of the whole SIL-catalogue, spanning several years of data, will illuminate larger parts of active faults. In this manner the whole tectonic structure of the SISZ can be mapped.

References

Allen, R. M., G. Nolet, W. J. Morgan, K. Vogfjörd, M. Nettles, G. Ekström, B. H. Bergsson, P. Erlendsson, G. Foulger, S. Jakobsdóttir, B. Julian, M. Pritchard, S. Ragnarsson, and R. Stefánsson, 2002. Plume driven plumbing and crustal formation in Iceland, *J. Geophys. Res.*, 107 (B8) 101029/2001JB000584.

Angelier, J., and F. Bergerat, 2002. Behaviour of a rupture of the 21 June 2000 earthquake in south Iceland as revealed in an asphalted car park. *J. Struct. Geol.*, 24, 1925-1936.

Antonioli, A., M. E. Belardinelli, A. Bizzari, and K. S. Vogfjord, 2006. Evidences of instantaneous triggering during the seismic sequence of year 2000 in south Iceland. *J. Geophys. Res.*, 111, doi:10.1029/2005JB003935.

Ágústsson, K., 2006. Mat á næmni SIL jarðskjálftamælinetsins. Hugmyndir um framtíðaruppbyggingu. *Icelandic Meteorological Office Report* 06014, VÍ-ES-08.

Ágústsson, K., and Ó. G. Flóvenz, 2005. The Thickness of the Seismogenic Crust in Iceland and its Implications for Geothermal Systems. *Proceeding World Geothermal Congress*, Antalya, Turkey, 24-29 April 2005.

Ármannsdóttir, S, 2008. Endurstaðsetning jarðskjálfta á Hengilssvæðinu 1. apríl 1955 út frá jarðskjálftaáhrifum. BS-thesis submitted to science department of University of Iceland, faculty of geology and geography (in Icelandic), *Icelandic Meteorological Office Report* 08010, VÍ-ES-05.

Árnadóttir, T., S. Rögnvaldsson, S., K. Ágústsson, R. Stefansson, S. Hreinsdóttir, K. Vogfjörð, and G. Thorbergsson, 1999. Seismic swarms and surface deformation in the Hengill area, SW Iceland. *Seismol. Res. Lett. 70*, 269.

Árnadóttir, T., S. Hreinsdóttir, G. Guðmundsson, P. Einarsson, M. Heinert, C. Völksen, 2001. Crustal deformation measured by GPS in the South Iceland Seismic Zone due to two large earthquakes in June 2000. *Geophys. Res. Lett., 28*, 4031-4033.

Árnadóttir, T., S. Jónsson, R. Pederssen, and G. B. Guðmundsson, 2003. Coulomb stress changes in the South Iceland Seismic Zone due to two large earthquakes in June 2000. *Geophys. Res. Lett.*, 30(5), 1205, doi:10.1029/2002GL016495.

Árnadóttir, T., H. Geirsson, and P. Einarsson, 2004. Coseismic stress changes and crustal deformation on the Reykjanes Peninsula due to triggered earthquakes on June 17, 2000. *J. Geophys. Res., 109*, B09307, doi:10.1029/2004JB003130.

Árnadóttir, T., S. Jónsson, F. F. Pollitz,W. Jiang, and K. L. Feigl, 2005. Postseismic deformation following the June 2000 earthquakes sequence in the south Iceland seismic zone. *J. Geophys. Res.*, 110, B12309, doi:10.1029/2005JB003701.

Árnadóttir, T., W. Jiang, K. L. Feigl, H. Geirsson, and E. Sturkell, 2006. Kinematic models of plate boundary deformation in southwest Iceland derived from GPS observations. *J. Geophys. Res.*, 111, B07402, doi:10.1029/2005JB003907.

Bergerat, F., and J Angelier, 2000. The south Iceland seismic zone: tectonic and seismotectonic analyses revealing the evolution from rifting to transform motion. *Journal of Geodynamics*, 29, 211-231.

Bjarnason, I., and P. Einarsson, 1991. Source mechanism of the 1987 Vatnafjöll earthquake in South Iceland. *J. Geophys. Res.,* 96, 4313-4324.

Bjarnason, I. Th., P. Cowie, M. H. Anders, L. Seeber, and C. H. Scholz, 1993. The 1912 Iceland earthquake rupture: Growth and development of a nascent transform system. *Bull. Seismol. Soc. Am.*, 83, 416-435.

Bjarnason, I. Th., W. Menke, Ó. G. Flóvenz, and D. Caress, 1993. Tomographic image of the Mid-Atlantic Plate Boundary in southwest Iceland. *J. Geophys. Res.*, 98, 6607-6622.

Brune, J. N., 1970. Tectonic Stress and the Spectra of Seismic Shear Waves from Earthquakes. *J. Geophys. Res.*, 75, 4997-5009.

Brune, J. N., 1971. Correction. *J. Geophys. Res.*, 76, 5002.

Böðvarsson, R., S. Th. Rögnvaldsson, S. S. Jakobsdóttir, R. Slunga and R. Stefánsson, 1996. The SIL Data Acquisition ans Monitoring System. *Seism. Res. Lett.*, 67, 5, 35-46.

Böðvarsson, R., S. Th. Rögnvaldsson, R. Slunga, and E. Kjartansson, 1998. The SIL data acquisition system – at present and beyond year 2000. *Icelandic Meteorological Office Rit* VÍ-R98005-JA04.

Clifton, A. E., F. Sigmundsson, K. L. Feigl, G. Guðmundsson, and T. Árnadóttir, 2002. Surface effects of faulting and deformation resulting from magma accumulation at the Hengill triple junction, SW Iceland, 1994-1998. *Journal of Volcanology and Geothermal Research*, 115, 233-255.

Clifton, A. E., C. Pagli, J. F. Jónsdóttir, K. Eythorsdóttir, and K. Vogfjörð, 2003. Surface effects of triggered fault slip on Reykjanes Peninsula, SW Iceland. *Tectonophysics,* 369, 145-154.

Clifton, A., and P. Einarsson, 2005. Styles of surface rupture accompanying the June 17 and 21, 2000 earthquakes in the South Iceland Seismic Zone. *Tectonophysics,* 396, 141-159.

Clifton, A. E., and S. Kattenhorn, 2006. Structural architecture of a highly oblique divergent plate boundary segment. *Tectonophysics*, 419, 27-40.

Darbyshire, F. A., K. F. Priestley, R. S. White, R. Stefánsson, G. B. Gudmundsson and S. S. Jakobsdóttir, 2000. Crustal strucure of central and northern Iceland from analysis of teleseismic receiver functions, *Geophys. J. Int.*, 143, 163-184.

DeMets, C. G., R. G. Gordon, D. F. Argus, and S. Stein, 1990. Current plate motions, *Geophys. J. Int., 101*, 425-478.

DeMets, C., R. G. Gordon, D. F. Stein, 1994. Effect of recent revisions to the geomagnetic reversal time scale on estimates of current plate motions. *Geophys. Res. Lett., 21*, 2191-2194.

Du, Z. and G. R. Foulger, 2001. Variation in the crustal structure across central Iceland, *Geophys. J. Int.,* 145, 246-264.

Dubois, L., K. L. Feigl, D. Komatitsch, T. Árnadóttir, and F. Sigmundsson, 2008. Three-dimensional mechanical models for the June 2000 earthquake sequence in the south-Iceland seismic zone. *Tectonophysics*, 457, 12-29.

Einarsson, P., 1985. Jarðskjálftaspár. (in Icelandic, English abstract: Earthquake prediction). *Náttúrufræðingurinn*, 55(1), 9-25.

Einarsson, P. Earthquakes and present-day tectonism in Iceland, 1991. *Tectonophysics*, 189, 261-279.

Einarsson, P, 2008. Plate boundaries, rifts and transforms in Iceland. *Jökull*, 58, 35-58.

Einarsson, P., S. Björnsson, G. Foulger, R. Stefánsson, and Þ. Skaftadóttir, 1981. Seismicity pattern in the South Iceland seismic zone, in: Earthquake Prediction - An International Review (eds. D. Simpson and P. Richards). *American Geophys. Union, Maurice Ewing Series* 4, 141-151.

Einarsson, P., and J. Eiríksson, 1982. Earthquake fractures in the districts Land and Rangárvellir in the South Iceland Seismic Zone. *Jökull*, 32, 113-120.

Einarsson, P. and K. Sæmundsson, 1987. Earthquake epicentres 1982-1985 and volcanic systems in Iceland (map). In Þ. I. Sigfússon (editor), *Í hlutarins eðli*. Festchrift for Þorbjörn Sigurgeirsson, Menningarsjóður, Reykjavík.

Einarsson, E., M. Böttger, and S. Þorbjarnarson, 2002. Faults and fractures of the South Iceland Seismic Zone near Þjórsá. The Icelandic Power Company, Landsvirkjun, Report LV-2002/090, 8 pp.

Einarsson, P., P. Theodórsson, Á. R. Hjartardóttir, and G. I. Guðjónsson, 2008. Radon anomalies associated with the earthquakes sequence in June 2000 in the South Iceland Seismic Zone, *Pure appl. geophys.* 165, 63-74. PAGEOPH. Topical. "Terrestrial fluids, earthquakes and volcanoes: The Hiroshi Wakita Volume II", eds. Nemesio Perez, Sergio Gurrieri, Chi-Yu King and Yuri Taran, doi:10.1007/s00024-007-0292-6.

Erlendsson, P., and P. Einarsson, 1996. The Hvalhnúkur fault, a strike-slip fault mapped within the Reykjanes Peninsula oblique rift, Iceland. In *Seismology in Europe, XXV ESC General Assembly*, September 9-14, 1996, Reykjavík, Iceland, edited by B. Thorkelsson, pp. 498-505, Icelandic Meteorological Office, Ministry for the Environment, University of Iceland, Reykjavík.

Feigl, K., J. Gasperi, F. Sigmundsson, and A. Rigo, 2000. Crustal deformation near Hengill volcano, Iceland 1993-1998: Coupling between magmatic activity and faulting inferred from elastic modeling of satellite radar interferograms. *J. Geophys. Res.*, 105, 25,655-25,670.

Flóvenz, Ó. G. and K. Gunnarsson, 1991. Seismic crustal structure in Iceland and surrounding area, *Tectonophysics*, 189, 1-17.

Foulger, G. R., 1988. Hengill triple junction, SW Iceland: 1. Tectonic structure and spatial and temporal distribution of local earthquakes. *J. Geophys. Res.*, 93, 13493-13506.

Geirsson, H., T. Árnadóttir, C. Völksen, W. Jiang, E. Sturkell, T. Villemin, P. Einarsson, F. Sigmundsson, and R. Stefánsson, 2006. Current plate movements across the Mid-Atlantic Ridge determined from 5 years of continuous GPS measurements in Iceland. *J. Geophys. Res.,* 111, B09407, doi: 1029/2005JB003717.

Got, J. L., J. Fréchet and F. W. Klein, 1994. Deep fault plane geometry inferred from multiplet relative relocation beneath the south flank of Kilauea. *J. Geophys. Res.*, 99, 15375-15386.

Guðmundsson, Á., and S. Brynjólfsson, 1993. Overlapping rift zone segments and the evolution of the South Iceland Seismic Zone. *Geophys. Res. Lett.,* 20, 1903-1906.

Guðmundsson, G. B., B. S. Þorbjarnardóttir, and M. J. Roberts, 2008. Seismicity in Iceland 2007 (in Icelandic: Jarðskjálftavirkni á Íslandi 2007). *Geoscience Society of Iceland, Spring meeting* 2008, p. 30.

Hackman, M. C., G. C. P. King, and R. Bilham, 1990. Mechanics of the South Iceland Seismic Zone. *J. Geophys. Res.,* 95, 17,339-17,351.

Halldórsson, P., 2004. Historical earthquakes M>4 in 1706-1990. Retrieved 26 August 2009 from *http://hraun.vedur.is/ja/ymislegt/storskjalf.html*.

Hjaltadóttir, S., K. S. Vogfjörð, Þ. Árnadóttir, P. Einarsson, 2005. A model of the release of the two June 2000 earthquakes based on all observations. Icelandic Meteorological Office Report, 05020, VÍ-ES-09.

Hjaltadóttir, S., K. S. Vogfjörð, 2005. Subsurface fault mapping in Southwest Iceland by relative location of aftershocks of the June 2000 earthquakes. *Icelandic Meteorological Office, Rit* 21.

Hjaltadóttir, S., and K. S. Vogfjörð, 2006. Kortlagning sprungna í Fagradalsfjalli á Reykjanesskaga með smáskálftum. Kortlagning jarðhita í gosbeltum Íslands – Fyrsti áfangi, 2006. *Icelandic Meteorological Office Report* 06001, VÍ-ES-01.

Hjaltadóttir, S. and K. S. Vogfjörð, 2009a. Bitrusprunga á Hellisheiði kortlögð við gamla þjóðveg með endurstaðsettum smáskjálftum. *Icelandic Meteorological Office Report*, VÍ 2009-005 .

Hjaltadóttir, S. and K. S. Vogfjörð, 2009b. Kortlagning sprungna í nágrenni Prestahnúks með smáskjálftum. Kortlagning jarðhita í gosbeltum Íslands - Annar áfangi, unnið fyrir Orkustofnun (in Icelandic, abstract in English). *Icelandic Meteorological Office Report*, VÍ 2009-011.

Hjaltadóttir, S. and K. S. Vogfjörð, 2009c. Seismic Signs of Magma Pathways through the Crust in the Eyjafjallajökull Volcano, South Iceland. *Icelandic Meteorological Office Report*, VÍ- 2009-013.

Hreinsdóttir, S., P. Einarsson, F. Sigmundsson, 2001. Crustal deformation at the oblique spreading Reykjanes Peninsula, SW Iceland: GPS measurements from 1993 to 1998, *J. Geophys. Res.*, 106, 13,803-13,816.

Hreinsdóttir, S., T. Árnadóttir, J. Decriem, H. Geirsson, A. Tryggvason, R. A. Bennet, and P. LaFemina, 2009. A complex earthquake sequence captured by the continuous GPS network in Iceland. *Geophys. Res. Lett.*, 36, L12309, doi:10.1029/2009GL038391, 5 pp.

Iio, Y, 1996. Depth-dependent change in the focal mechanism of shallow earthquakes: Implications for brittle-plastic transition in a seismogenic region. *J. Geophys. Res.*, 101, 11209-11216.

Jakobsdóttir, S. S., 1998. Uppsetning SIL-kerfisins. *Icelandic Meteorological Office Report* VÍ-G98012-JA01.

Jakobsdóttir, S. S., G. B. Guðmundsson, and R. Stefánsson, 2002. Seismicity in Iceland 1991-2000 monitored by the SIL-system. *Jökull* 51, 87-94.

Jóhannesson, H., S. P. Jakobsson, and K. Saemundsson, 1990. Geological map of Iceland, sheet 6, South-Iceland, third edition. –*Icelandic Museum of Natural History and Icelandic Geodetic Survey*, Reykjavík.

Jóhannesson, H., and K. Saemundsson, 1998. Geological Map of Iceland. 1:500 000. Tectonics. *Icelandic Institute of Natural History*, Reykjavík (1st edition).

Jónsson, S., P. Segall, R. Pederssen, and G. Björnsson, 2003. Post-earthquake ground movements correlated to pore-pressure transients. *Nature*, 424, 179-183.

Kanamori, H., and D. L. Anderson, 1975. Theoretical basis of some empirical relations in seismology. *Bull. Seism. Soc. Am.*, 65, 1073-1095.

Karlsdóttir, R., 2004. TEM-mælingar á Geysissvæði. Unnið fyrir Auðlindadeild Orkustofnunar. *Iceland Geosurvey Report* ÍSOR-2004/029.

Keiding, M., T. Árnadóttir, E. Sturkell, H. Geirsson, and B. Lund, 2008. Strain accumulation along an oblique plate boundary: the Reykjanes Peninsula, southwest Iceland. *Geophys. J. Int.*, 172, 861-872.

Lay, T., and T. C. Wallace, 1995. *Modern Global Seismology*, Academic Press.

LaFemina, P. C., T. H. Dixon, R. Malservisi, T. Árnadóttir, E. Sturkell, F. Sigmundsson, and P. Einarsson, 2005. Geodetic GPS measurements in south Iceland: Strain accumulation

and partitioning in a propagating ridge system. *J. Geophys. Res.*, 110, B11405, doi:10.1029/2005JB003675, 21 pp.

Meissner, R., and J. Strehlau, 1982. Limits of stresses in continental crusts and their relation to the depth-frequency distribution of shallow earthquakes, *Tectonics*, 1,73-89.

Menke, W., B. Brandsdóttir, P. Einarsson, and I. Th. Bjarnason, 1996. Reinterpretation of the RRISP-77 Iceland shear-wave profiles. *Geophys. J. Int.*, 126, 166-172.

Pagli, C., R. Pedersen, F. Sigmundsson, and K. L. Feigl, 2003. Triggered fault slip on June 17, 2000 on the Reykjanes Peninsula, SW-Iceland captured by radar interferometry, *Geophys. Res. Lett.*, 30(6), 1273, doi:10.1029/2002GL015310, 2003.

Pedersen, R., S. Jónsson, Þ. Árnadóttir, F. Sigmundsson, and K.L. Feigl, 2003. Fault slip distribution of two June 2000 Mw 6.5 earthquakes in South Iceland estimated from joint inversion of InSAR and GPS measurements. *Earth and Planet. Sci. Lett.*, 213, 487-502.

Pétursson, G. G., and K. S. Vogfjörð, 2009. Attenuation relations for near and far field peak ground motion (PGV, PGA) and new magnitude estimate for large earthquakes in SW-Iceland. *Icelandic Meteorological Office Report*, VÍ-2009-012.

Roth, F., 2004. Stress Changes Modelled for the Sequence of Strong Earthquakes in the South Iceland Seismic Zone Since 1706. *Pure & Applied Geophysics*, 161, 1305-1327.

Rögnvaldsson, S. Th., 2000. Kortlagning virkra misgengja með smáskjálftamælingum-yfirlit, summarized by Þóra Árnadóttir and Kristín S. Vogfjörð. *Icelandic Meteorological Office Rit*, VÍ-R00001-JA01.

Rögnvaldsson, S. Th., and R. Slunga, 1993. Routine fault plane solutions for local networks: A test with synthetic data. *Bull. Seismol. Soc. Am.*, 83, 1232-1247.

Rögnvaldsson, S. Th., and R. Slunga, 1994. Single and joint fault plane solutions for miqroearthquakes in South Iceland. *Tectonophysics*, 237, 73-80.

Rögnvaldsson, S. Th., A. Guðmundsson, and R. Slunga, 1998a. Seismotectonic analysis of the Tjörnes Fracture Zone, an active transform fault in north Iceland. *J. Geophys. Res.*, 103, B12, 30117-30129.

Rögnvaldsson, S. Th., G. B. Guðmundsson, K. Ágústsson, S. S. Jakobsdóttir, R. Slunga, R. Stefánsson, 1998b. Overview of the 1993-1996 seismicity near Hengill. *Icelandic Meteorological Office Research Report* VÍ-R98006-JA05.

Rögnvaldsson, S. Th., Þ. Árnadóttir, K. Ágústsson, Þ. Skaftadóttir, G. Guðmundsson, G. Björnsson, K. Vogfjörð, R. Stefánsson, R. Böðvarsson, R. Slunga, S. S. Jakobsdóttir, B. Thorbjarnardóttir, P. Erlendsson, B. Bergsson, S. Ragnarsson, P. Halldórsson, B. Thorkelsson, and M. Ásgeirsdóttir, 1998c. Skjálftahrina í Ölfusi í nóvember. *Icelandic Meteorological Office Report*, VÍ-G98046-JA09 (In Icelandic, English summary).

Rögnvaldsson, S. Th., K. S. Vogfjörð, and R. Slunga, 1999. Kortlagning brotflata á Hengilssvæði með smáskjálftum. *Icelandic Meteorological Office Rit*, VÍ-R99002-JA01.

Sandron, D., 2006. Inversion of strong motion data for slip on extended faults: The case of the two M6.5 Iceland earthquakes of June 2000. *Doctor's thesis*, Department of Earth Science, University of Trieste, Italy.

Scholz, C. H., 1988. The brittle-plastic transition and the depth of seismic faulting. *Geologische Rundschau*, 77, 319-328.

Sibson, R. H., 1982. Fault zone models, heat flow, and the depth distribution of earthquakes in the continental crust of the United States. *Bull. Seism. Soc. Am.*, 72, 151-163.

Sigmundsson, F., P. Einarsson, R. Bilham, E. Sturkell, 1995. Rift-transform kinematics in south Iceland: Deformation from Global Positioning System measurements, 1986 to 1992. *J. Geophys. Res.*, 100, 6235-6248.

Sigmundsson, F., P. Einarsson, S. Rögnvaldsson, G. R. Foulger, K. M. Hodgkinson, and G. Thorbergsson, 1997. The 1994-1995 seismicity and deformation at the Hengill triple junction, Iceland: Triggering of earthquakes by minor magma injection in a zone of horizontal shear stress. *J. Geophys. Res.,* 102, 15,151-15,161.

Slunga, R., S. Th. Rögnvaldsson, and R. Bödvarsson, 1995. Absolute and relative locations of similar events with application to microearthquakes in southern Iceland. *Geophys. J. Int.*, 123, 409-419.

Staples, R. K., R. S. White, B. Brandsdóttir, W. Menke, P. K. H. Maguire, and J. H. McBride, 1997: Faroe-Iceland Ridge Experiment. 1. Crustal structure of northeastern Iceland, *J. Geophys. Res.*, 102, 7849-7866.

Stefánsson, R., 1979. Catastrophic earthquakes in Iceland. *Tectonophysics*, 53, 273-278.

Stefánsson, R., and P. Halldórsson, 1988. Strain release and strain build-up in the south Iceland seismic zone. *Tectonophysics*, 152, 267-276.

Stefánsson, R., R. Böðvarsson, R. Slunga, P. Einarsson, S. Jakobsdóttir, H. Bungum, S. Gregersen, J. Havskov, J. Hjelme, and H. Korhonen, 1993. Earthquake prediction research in the South Iceland seismic zone and the SIL project, *Bull. Seismol. Soc. Am.,* 83, 696-716.

Stefánsson, R., G. B. Guðmundsson, and P. Halldórsson, 2000. The two large earthquakes in the South Iceland seismic zone on June 17 and 21, 2000. *Icelandic Meteorological Office – Report* G00010.

Strehlau, J., 1986. A discussion of the depth extent of rupture in large continental earthquakes. In: Eds. S. Das, J. Boatwright and C. Scholz, *Earthquake Source Mechanics*, AGU Geophys. Mono. 37, Washington, D.C., 131-146.

Sæmundsson, K., and S. Einarsson, 1980. Geological map of Iceland, sheet 3, SW-Iceland, second edition. – *Museum of Natural History and the Iceland Geodetic survey*, Reykjavík.

Sæmundsson, K., 1992. Geology of the Thingvallavatn area. *Oikos*, 64, 40-68. In ed. P. M. Jónasson, Ecology of oligotrophic, subarctic Thingvallvatn. *The Icelandic Lit. Soc., Copenhagen*.

Sæmundsson, K., 1995. Hengill geological map (bedrock) 1:50 000. *Orkustofnun, Hitaveita Reykjavíkur, Landmælingar Íslands.*

Thoroddsen, Th., 1899 and 1905. Landskjálftar á Íslandi, *The Icelandic Lit., Soc.*, Copenhagen, 269 pp.

Torfason, H., and I. Davíðsson, 1985. *The Great Geysir*, the Geysir Conservation Committee, Reykjavík, 23 pps.

Tryggvason, E., 1973. Seismicity, earthquake swarms and plate boundaries in the Iceland region. *Bull. Seismol. Soc. Am.*, 63, 1327-1348.

Tryggvason, A., S. Th. Rögnvaldsson, and O. G. Flovenz, 2002. Three-dimensional imaging of the P- and S-wave velocity structure and earthquake locations beneath southwest Iceland, *Geophys. J. Int.*, 151, 848-866.

Vogfjörð, K. S., 2000. Kortlagning brotflata með smáskjálftum í nágrenni Grændals. *National Energy Autority – Report* OS-2000/031

Vogfjörd, K. S., G. Nolet, W. J. Morgan, R. M. Allen, R. Slunga, B. H. Bergsson, P. Erlendsson, G. Foulger, S. Jakobsdóttir, B. Julian, M. Pritchard, S. Ragnarsson, 2002. Crustal profiling in Iceland using earthquake source arrays, *AGU Fall meeting, Abstract* S61C-1161, San Francisco, California, 6-10 December, 2002.

Vogfjord, K. S., 2003. Triggered seismicity in SW Iceland after the June 17, Mw=6.5 earthquake in the South Iceland Seismic Zone: The first five minutes. *Geophysical Research Abstracts*, Vol. 5, 11251.

Vogfjörð, K. S., H., Geirsson and E. Sturkell, 2004. Krísuvíkurhrinan í ágúst 2003: kortlagning brotflata með eftirskjálftum og GPS mælingum. *Geoscience Society of Iceland, Spring Meeting 2004*, p. 41.

Vogfjörd, K. S., S. Hjaltadóttir and R. Slunga, 2005a. Volcano-tectonic Interaction in the Hengill Region, Iceland during 1993-1998. *Geophysical Research Abstracts*, 7, 09947.

Vogfjörd, K. S., Sigurlaug Hjaltadóttir og R. Slunga, 2005b. The M~5 triggered events in the South Iceland Seismic Zone of June 17, 2000: Determination of fault plane, magnitude and mechanism. *Geophysical Research Abstracts,* 7, EGU-A-10274.

Vogfjörð, K. S., and S. Hjaltadóttir, 2007. Kortlagning skjálftavirkni við Hverahlíð á Hellisheiði í Febrúar 2006. Unnið fyrir Orkuveitu Reykjavíkur (in Icelandic). *Icelandic Meteorological Office Report*, 07010, VÍ-ES-04.

Vogfjord, K. S., S. Hjaltadottir, H. Geirsson and R. Slunga, 2009. Fault Interaction in the South Iceland Seismic Zone: The May 2008, M6.3 earthquake. *Geophysical Research Abstracts*, Vol. 11, EGU2009-11748-1.

Waldhauser, F., W. L. Ellsworth, and A. Cole: Slip-Parallel Seismic Lineations on the Northern Hayward Fault, California, 1999. *Geopys. Res. Lett.*, 26, 3525-3528.

Waldhauser, F., and W. L. Ellsworth, 2000. A double-difference earthquake algorithm: Method and application to the northern Hayward Fault, California. *Bull. Seismol. Soc. Am.,* 90, 1353-1368.

Waldhauser, F., and W. L. Ellsworth, 2002. Fault structure and mechanics of the Hayward Fault, California, from double-difference earthquake locations. *Geophys. Res.*, 107, 10.1029/2000JB000084.

Weir, N. R. W., R. S. White, B. Brandsdóttir, P. Einarsson, H. Shimamura, H. Shiobara, and the RISE Fieldwork Team, 2001. Crustal structure of the northern Reykjanes Ridge and Reykjanes Peninsula, southwest Iceland, *J. Geophys. Res.,* 106, 6347-6368.

Wessel, P. and W. H. F. Smith, 1998. New improved version of generic mapping tools released. *EOS Trans*. AGU, 79(47), 579.

Wyss, M., and R. Stefánsson, 2006. Nucleation Points of Recent Mainshocks in Southern Iceland, Mapped by b-values. *Bull. Seism. Soc. Am.,* 96, 599-608.

Þorbergsson, G., and G. H. Vigfússon, 1998. Nesjavallaveita. Fallmælingar og GPS-mælingar á Hengilssvæði 1998. *Icelandic Energy Authority Report* OS-98060.

APPENDIX A –List of fault parameters

Parameters for the mapped faults and fault segments in boxes A-O are listed in tables A1-A5. These parameters are: strike (ϕ), dip (δ), average rake (λ_{ave}), average rake weighted with moment (λ_{wav}), length of fault, average latitude and longitude (Y, X) of the events used to define the fault plane, number of events and rms distance of events from the average fault plane.

Table A.1. *Fault parameters for mapped fault segments and clusters in the Geysir region (boxes A1-A3).*

Fault segment	φ (°)	δ (°)	λave (°)	λwav (°)	Length (km)	X (°E)	Y (°N)	#events	rms (m)
A2-01	202.0	90.0	-154.57	-164.04	2.621	64.4627	-20.3385	21	64.4
A2-02	29.0	86.0	-173.24	-156.79	1.200	64.4223	-20.2858	133	40.8
A2-03	224.0	76.0	-159.03	-168.85	0.433	64.3594	-20.2921	32	15.9
A1-04	27.0	88.0	160.10	173.83	2.574	64.2827	-20.3150	121	66.4
A1-05	177.0	89.0	-167.04	-159.73	1.072	64.3090	-20.3030	7	34.5
A2-06	34.0	86.0	-164.70	-163.88	1.300	64.4017	-20.3275	51	17.1
A2-07	33.0	89.0	-172.16	-167.07	0.769	64.3989	-20.2934	70	14.5
A1-08	25.0	73.0	91.27	102.45	0.791	64.2641	-20.2979	19	20.4
A1-09	233.0	46.0	-174.24	177.44	0.681	64.2671	-20.3030	13	19.2
A1-10	182.0	78.0	169.99	149.33	0.438	64.3077	-20.2785	7	15.3
A3-11	181.0	87.0	-151.70	-130.68	0.514	64.3383	-20.4992	10	8.8
A1-12	56.0	84.0	-160.20	-160.44	0.779	64.3200	-20.2458	17	50.0
A1-13	19.0	80.0	-150.04	-160.29	0.122	64.2972	-20.3373	7	5.2
A1-14	219.0	85.0	-10.56	-107.85	0.635	64.2825	-20.3556	10	46.6
A1-15	200.0	85.0	-139.34	-153.13	1.394	64.2886	-20.2678	10	21.3
A1-16	216.0	88.0	-170.26	-94.76	0.397	64.2871	-20.2772	5	6.8
A2-17	42.0	63.0	-120.23	-127.72	0.414	64.4062	-20.2318	17	20.2
A2-18	219.0	89.0	176.95	-168.82	0.166	64.4042	-20.2142	7	11.4
A2-19	259.0	76.0	-67.27	-93.24	0.438	64.4148	-20.2498	14	25.0
A2-20	43.0	77.0	-144.33	-136.09	0.707	64.3981	-20.3212	22	32.1
A2-21	31.0	88.0	-177.68	-167.27	0.727	64.3883	-20.2952	15	21.9
A2-22	301.0	88.0	6.01	12.77	0.426	64.4049	-20.3417	7	22.5
A2-23	210.0	89.0	169.75	163.44	0.525	64.3952	-20.2986	22	13.4
A2-24	32.0	82.0	-168.79	-165.64	0.590	64.3955	-20.3023	39	11.1
A2-25	28.0	82.0	-171.15	-170.10	0.523	64.3963	-20.3053	62	24.1
A2-26	26.0	81.0	-158.87	-142.64	0.769	64.3955	-20.2961	19	14.3
A3-27	187.0	73.0	-171.06	-167.81	0.213	64.3378	-20.5069	4	0.5
A3-28	179.0	85.0	148.89	137.40	0.129	64.3356	-20.5136	4	4.5
A3-29	15.0	85.0	-80.95	-140.67	1.281	64.2990	-20.5294	9	18.8
A3-30	192.0	87.0	-152.01	-157.03	0.309	64.3038	-20.4478	15	8.5
A3-31	186.0	84.0	167.22	151.62	0.237	64.3037	-20.4619	7	28.2
A3-32	214.0	88.0	166.51	145.65	0.255	64.3766	-20.6391	7	10.0
A3-33	231.0	76.0	167.97	172.24	0.125	64.3772	-20.6350	3	0.3

Table A.2. *Fault parameters for mapped fault segments and clusters on the Reykjanes Peninsula (boxes B-F).*

Fault segment	φ (°)	δ (°)	λave (°)	λwav (°)	Length (km)	X (°E)	Y (°N)	#events	rms (m)
B-02	178.0	88.0	162.39	-171.02	0.366	63.8879	-22.3290	32	6.2
B-03	199.0	90.0	177.46	-109.98	0.472	63.8865	-22.3273	44	10.5
B-04	356.0	86.0	-176.06	-168.86	0.188	63.8915	-22.3249	13	4.6
B-05	198.0	86.0	-178.56	-127.83	0.080	63.8904	-22.3267	6	1.7
B-06	177.0	90.0	171.13	170.41	0.115	63.8950	-22.3231	8	5.3
B-07	37.0	89.0	-156.73	-117.82	0.130	63.8940	-22.3242	9	5.8
B-08	125.0	90.0	14.13	17.07	0.174	63.8835	-22.3261	6	5.5
B-09	171.0	85.0	-151.02	-141.75	0.137	63.8831	-22.3459	8	8.5
B-10	243.0	84.0	-37.86	-51.57	0.829	63.8939	-22.3165	80	37.1
B-11	5.0	89.0	-160.71	178.85	0.365	63.8867	-22.3489	9	17.5
B-12	224.0	88.0	-11.68	-33.33	0.215	63.8906	-22.3357	13	10.2
B-13	217.0	77.0	-72.39	-72.73	0.112	63.8906	-22.3370	5	2.0
B-14	196.0	88.0	177.38	173.99	0.190	63.8916	-22.3329	8	7.0
B-18	230.0	88.0	-50.90	-150.57	0.137	63.8924	-22.3147	5	4.4
C-02	182.0	88.0	172.31	-178.60	0.465	63.8943	-22.2181	22	5.8
C-03	189.0	85.0	-167.22	-161.81	0.406	63.8933	-22.2216	11	13.8
C-04	176.0	87.0	168.41	-176.75	0.960	63.9060	-22.2381	29	48.0
C-05	174.0	49.0	-145.07	-171.62	0.166	63.8917	-22.2403	6	3.3
D-02	241.0	90.0	5.22	7.79	1.296	63.9536	-22.0778	21	19.6
D-03	16.0	84.0	-160.49	158.30	0.759	63.9377	-22.0712	24	26.4
D-05	1.0	84.0	178.97	-60.41	0.918	63.9189	-22.0473	21	8.9
D-06	2.0	89.0	-142.16	-156.34	1.013	63.9206	-22.0436	28	19.8
D-07	6.0	88.0	-155.70	-75.13	0.452	63.9236	-22.0365	19	16.9
D-08	52.0	87.0	11.96	36.96	0.880	63.9290	-22.0291	33	45.9
D-09	21.0	89.0	-99.32	-130.76	0.323	63.9169	-21.9979	11	16.2
D-10	10.0	87.0	170.64	165.17	6.379	63.9052	-21.9651	50	103.0
D-11	239.0	90.0	22.75	48.22	0.807	63.9214	-22.0575	16	39.7
D-12	49.0	85.0	-0.65	4.54	0.674	63.9089	-22.0298	12	25.6
D-13	226.0	87.0	79.56	1.90	0.713	63.8962	-22.1380	14	54.0
D-14	218.0	88.0	125.61	83.36	1.451	63.9016	-22.1015	30	77.4
E-02	3.0	82.0	143.70	148.83	1.826	63.8834	-21.7133	42	34.6
E-03	9.0	85.0	165.89	-173.82	0.949	63.8789	-21.6832	21	18.1
E-04	184.0	79.0	149.57	166.35	0.930	63.8991	-21.7061	7	37.6
E-25	195.0	88.0	-179.03	-166.66	8.770	63.9054	-21.7016	78	114.9
E-24	4.0	81.0	167.44	157.39	3.285	63.8857	-21.7123	45	40.9
F-02	175.0	88.0	-165.29	-167.40	0.331	64.0090	-21.5070	12	11.3
F-03	272.0	88.0	-0.20	-32.17	0.201	63.9908	-21.4894	7	10.8
F-04	10.0	86.0	178.95	167.24	0.537	63.9771	-21.6017	12	27.3
F-05	186.0	90.0	178.30	-140.01	0.258	63.9818	-21.5166	10	30.1
F-06	177.0	87.0	172.28	-173.89	0.554	63.9628	-21.7687	9	25.5
F-07	357.0	88.0	172.83	164.30	0.768	63.9626	-21.7472	10	57.8
F-08	150.0	84.0	11.61	-22.51	0.194	64.0211	-21.6011	4	2.4
F-10	13.0	89.0	-95.76	-77.90	0.648	63.9817	-21.5831	8	27.0
F-19	16.0	89.0	168.63	148.38	3.004	63.9450	-21.6795	24	180.4
F-09	167.0	85.0	155.06	-171.29	0.603	63.9473	-21.6755	11	40.2

Table A.3. *Fault parameters for mapped fault segments and clusters in the Hengill area and the South Iceland seismic zone (boxes G-I).*

Fault segment	φ (°)	δ (°)	λ_ave (°)	λ_wav (°)	Length (km)	X (°E)	Y (°N)	#events	rms (m)
G-02	4.0	81.0	151.26	151.96	0.210	63.9321	-21.4550	13	9.7
G-03	189.0	87.0	-149.45	-155.21	0.424	63.9476	-21.2919	20	8.4
G-04	174.0	84.0	-176.38	175.35	2.412	63.9118	-21.2728	32	75.6
G-05	227.0	88.0	-5.66	-11.48	0.797	63.9195	-21.1874	47	19.1
G-06	36.0	84.0	-12.71	88.26	0.094	63.9531	-21.1725	7	4.7
G-07	215.0	89.0	-117.35	-128.36	0.549	63.9932	-21.3490	37	32.5
G-08	14.0	84.0	179.10	172.96	0.489	63.9920	-21.3565	12	35.8
G-09	247.0	85.0	-22.83	-29.28	0.570	63.9797	-21.2271	15	18.7
G-10	60.0	88.0	-5.43	-6.94	0.665	63.9313	-21.4277	20	19.2
G-11	251.0	82.0	23.05	20.85	0.398	63.9438	-21.4280	11	28.1
G-12	219.0	87.0	-17.02	-18.86	0.240	63.9440	-21.2681	9	15.3
G-13	29.0	89.0	-38.19	-151.15	1.758	63.9525	-21.2496	17	30.1
G-14	175.0	89.0	177.51	162.92	0.189	63.9603	-21.1523	5	13.9
G-15	247.0	84.0	8.72	11.24	10.277	63.9386	-21.3944	98	302.1
G-16	255.0	88.0	-5.17	-3.39	5.845	63.9512	-21.2566	85	289.1
G-17	187.0	89.0	-156.53	176.62	12.185	63.9400	-21.1628	65	397.4
H1-02	102.0	81.0	-75.33	-49.69	0.157	64.0343	-21.2204	10	8.8
H1-03	199.0	89.0	-164.70	-152.63	0.927	64.0866	-21.1947	18	27.1
H1-04	28.0	70.0	175.54	-153.62	0.079	64.0235	-21.3944	9	2.0
H1-05	213.0	86.0	5.73	-29.68	0.219	64.0649	-21.3183	12	15.8
H1-06	27.0	74.0	164.03	162.33	0.744	64.0753	-21.1710	48	10.0
H1-07	23.0	81.0	178.13	175.01	0.347	64.0784	-21.1882	33	14.6
H1-08	30.0	76.0	166.92	-167.13	0.271	64.0817	-21.1681	27	6.4
H1-09	7.0	84.0	168.97	160.41	0.212	64.0841	-21.1660	5	3.6
H1-10	47.0	85.0	162.26	166.43	0.313	64.0811	-21.1641	16	13.1
H1-11	106.0	87.0	-6.49	13.41	0.256	64.0493	-21.2391	10	10.0
H1-12	59.0	89.0	-12.98	38.17	0.206	64.0476	-21.2354	9	9.7
H1-13	226.0	69.0	-53.69	-24.58	0.111	64.0474	-21.2307	8	12.4
H1-14	211.0	84.0	2.46	2.61	0.262	64.0692	-21.3141	14	13.8
H1-15	53.0	84.0	-34.68	-7.18	0.545	64.0713	-21.3173	28	18.5
H1-16	49.0	74.0	-92.66	-37.15	0.181	64.0583	-21.1913	5	1.9
H2-02	17.0	88.0	170.73	166.11	0.883	64.0545	-21.0944	69	28.5
H2-03	6.0	88.0	153.28	158.67	0.524	64.0650	-21.1421	9	9.6
H2-04	204.0	90.0	-103.55	-123.36	1.181	64.0330	-21.2225	18	38.1
H2-05	268.0	87.0	-11.16	-0.95	2.075	64.0629	-21.1684	165	66.1
H2-06	209.0	85.0	-120.02	-18.12	1.704	64.0340	-21.2139	24	49.3
H2-07	43.0	88.0	-20.44	20.04	0.736	64.1176	-21.2372	5	17.3
H2-08	197.0	90.0	-169.66	-148.33	0.378	64.0555	-21.1576	9	19.2
H2-09	178.0	88.0	-177.48	-162.53	0.776	64.0643	-21.2100	17	28.0
H2-10	6.0	87.0	149.88	156.35	0.964	64.0660	-21.2018	31	47.3
H2-11	198.0	90.0	-160.37	-178.02	0.904	64.0612	-21.1809	20	18.9
H2-12	45.0	86.0	-19.36	-13.62	0.615	64.0401	-21.2524	5	6.9
H2-20	201.0	90.0	-166.33	-167.03	0.196	64.0572	-21.0922	12	7.2
H2-21	168.0	90.0	161.30	157.84	0.270	64.0567	-21.0937	13	14.1
H2-22	36.0	88.0	-178.59	166.41	0.228	64.0549	-21.0935	17	12.7
H2-23	10.0	87.0	169.15	159.13	0.561	64.0523	-21.0960	32	22.8
I-02	33.0	76.0	-10.02	8.80	0.437	63.8963	-20.9471	13	8.3
I-04	15.0	88.0	-171.62	174.20	0.334	63.9257	-20.9237	10	9.9
I-05	230.0	86.0	7.06	8.13	0.707	63.8960	-20.9183	15	14.2
I-06	227.0	90.0	0.86	2.96	0.342	63.8922	-20.9210	6	3.5

I-07	43.0	86.0	-26.28	-32.95	0.399	63.9223	-21.0380	36	17.7
I-08	56.0	89.0	-18.88	-19.12	0.391	63.9526	-21.0869	13	16.1
I-09	5.0	86.0	-138.33	-168.09	0.609	63.9403	-20.9851	11	31.3
I-10	195.0	89.0	-176.88	160.54	0.387	63.9501	-20.9701	20	22.2
I-11	42.0	88.0	-4.32	23.78	0.285	63.9453	-20.9710	20	15.6
I-12	173.0	89.0	176.27	169.83	0.096	63.9512	-20.9607	12	5.3
I-13	357.0	79.0	-139.74	-127.28	0.095	63.9509	-20.9620	8	4.7
I-14	13.0	86.0	-36.62	-57.94	0.243	63.9462	-20.9680	13	13.9
I-15	353.0	65.0	-133.84	-131.95	0.201	63.9382	-21.0508	8	6.5
I-16	5.0	89.0	-165.92	-159.85	2.007	63.9471	-21.0429	14	65.6
I-17	3.0	89.0	-70.16	-54.82	0.252	63.9404	-20.9686	8	11.1
I-18	124.0	90.0	174.48	-170.35	0.120	63.9490	-20.9608	8	10.1
I-19	356.0	87.0	-172.45	-173.54	1.765	63.9714	-21.0729	12	32.2
I-20	4.0	89.0	-155.86	-162.03	2.621	63.9586	-21.0654	7	53.2
I-21	3.0	88.0	172.53	-177.68	9.417	63.9589	-20.9306	36	111.7
J-02	13.0	87.0	176.15	149.38	0.608	63.8076	-20.5669	18	40.1
J-03	184.0	84.0	-162.18	141.59	3.096	63.8010	-20.5542	27	69.5
J-04	355.0	86.0	156.63	157.55	0.867	63.8018	-20.5383	15	34.5
J-05	179.0	85.0	139.50	142.30	1.839	63.8051	-20.5256	25	51.9
J-06	33.0	73.0	-107.79	-141.95	9.456	63.8178	-20.7364	33	420.1
K-02	219.0	87.0	-11.90	-5.58	0.909	63.9080	-20.8739	15	17.1
K-03	179.0	89.0	-144.41	179.89	1.673	63.9497	-20.8470	132	83.7
K-04	24.0	77.0	-9.59	-18.48	1.063	63.9410	-20.8535	81	91.5
K-05	194.0	87.0	-56.12	-133.94	1.268	63.9489	-20.8587	48	78.4
K-06	49.0	75.0	-7.53	-6.69	0.666	63.9120	-20.8209	9	18.5
K-07	197.0	90.0	-16.01	-31.48	0.919	63.9098	-20.8280	13	15.9
K-08	168.0	88.0	-163.94	-168.45	1.335	63.9214	-20.8264	68	46.3
K-09	189.0	83.0	-80.63	-92.57	1.206	63.9223	-20.8193	50	87.1
K-10	201.0	90.0	-13.74	-3.24	2.154	63.9407	-20.8295	24	67.7
K-11	31.0	86.0	-113.36	-96.64	0.842	63.9637	-20.8800	21	32.6
K-12	214.0	90.0	-110.61	-23.19	0.251	63.9594	-20.8724	13	12.9
L-02	154.0	89.0	162.64	157.82	2.901	63.9492	-20.5954	21	35.4
L-03	149.0	87.0	140.02	126.49	0.657	63.9446	-20.6291	7	16.7
L-05	209.0	88.0	40.94	89.16	0.618	63.9412	-20.4675	14	41.3
L-08	182.0	89.0	168.46	168.37	2.134	63.9457	-20.4993	35	71.6
L-09	38.0	81.0	-110.72	-136.92	1.467	63.9729	-20.5405	15	77.2
L-10	175.0	85.0	144.23	154.96	3.092	63.9408	-20.4872	60	117.6
L-11	189.0	90.0	164.42	-51.15	6.013	63.9788	-20.5830	25	139.8
L-12	182.0	89.0	110.05	45.78	2.297	63.9323	-20.6013	13	138.0
M-02	195.0	78.0	-125.56	-120.18	2.931	63.9648	-20.1506	40	141.0
M-03	188.0	82.0	157.78	-172.29	1.826	63.9985	-20.1357	28	102.3
M-04	358.0	86.0	-160.27	-156.48	0.574	64.0088	-20.1398	19	21.0
M-05	26.0	85.0	-143.34	-164.32	1.506	64.0567	-20.2218	20	49.1
M-06	2.0	75.0	-129.05	-135.87	0.345	64.0108	-20.1360	10	19.4
M-07	56.0	56.0	177.98	174.03	0.284	64.0184	-20.2682	56	10.9
M-08	186.0	90.0	177.82	-165.34	5.947	63.9822	-19.9922	31	206.3
M-09	0.0	82.0	-114.97	-130.05	0.064	64.0025	-20.1466	7	5.3

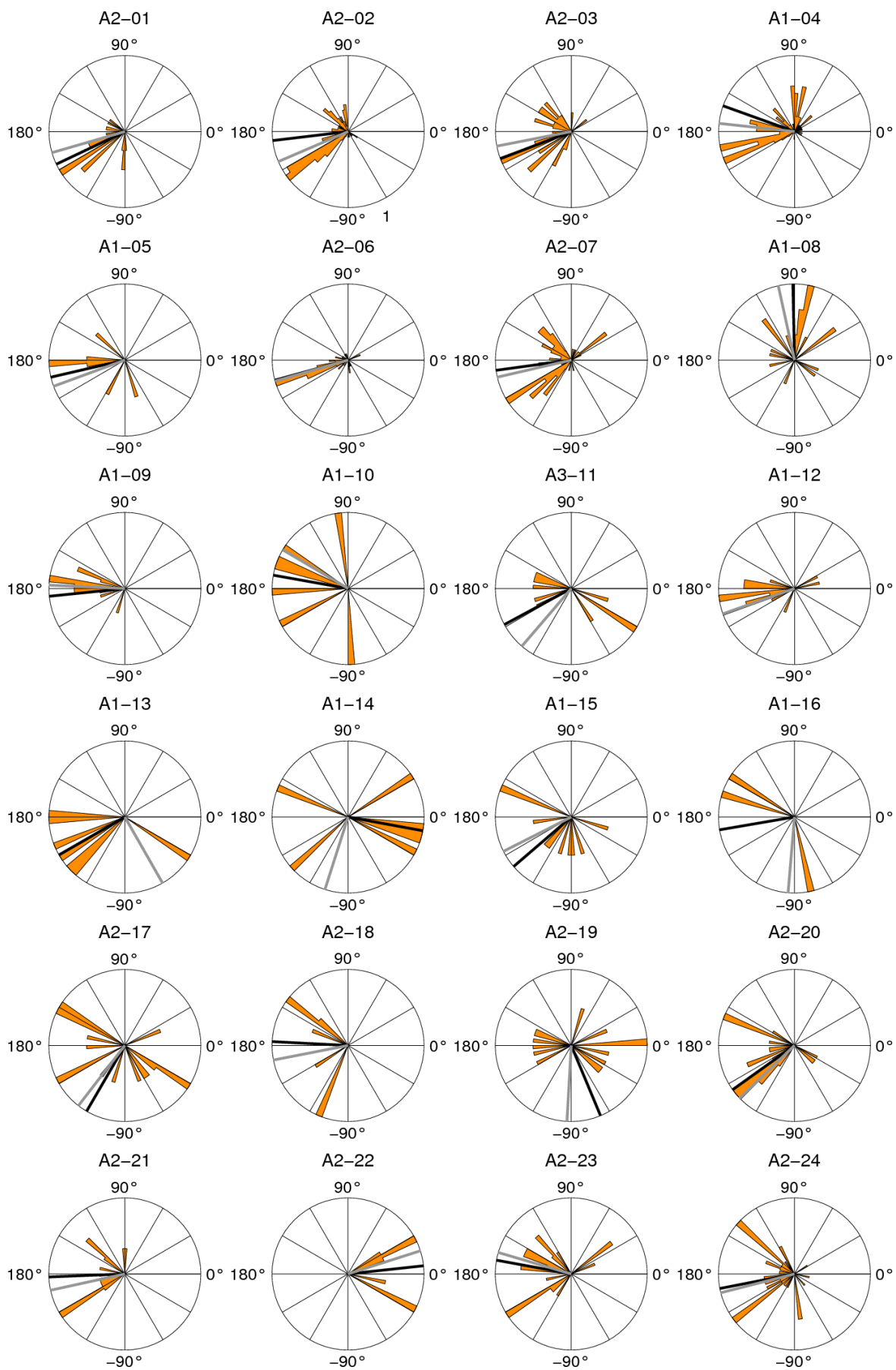**Table A.4.** *Fault parameters for mapped fault segments on the Hestvatn fault (J-21) (box N).*

Fault segment	φ (°)	δ (°)	λ$_{ave}$ (°)	λ$_{wav}$ (°)	Length (km)	X (°E)	Y (°N)	#events	rms (m)
Nsub1-02	243.0	89.0	-1.72	-7.75	2.460	63.9196	-20.7347	134	108.8
Nsub1-03	359.0	89.0	-158.01	-162.89	1.126	63.9270	-20.7743	12	21.0
Nsub1-04	225.0	88.0	-5.02	-11.95	0.658	63.9305	-20.7372	44	21.2
Nsub1-05	43.0	84.0	-7.47	28.61	0.254	63.9293	-20.7280	30	23.4
Nsub1-06	195.0	87.0	161.41	178.23	0.798	63.9492	-20.7407	40	17.4
Nsub1-07	1.0	89.0	-151.32	-146.90	0.402	63.9266	-20.7385	21	24.1
Nsub1-08	237.0	90.0	-3.11	2.72	0.571	63.9295	-20.7466	37	46.7
Nsub1-09	221.0	89.0	-16.58	-21.50	0.571	63.9304	-20.7319	18	25.5
Nsub1-10	359.0	89.0	-152.54	-155.34	0.991	63.9231	-20.7483	25	48.9
Nsub1-11	225.0	89.0	-63.11	-10.43	1.564	63.9478	-20.7714	36	70.6
Nsub1-4-01	226.0	88.0	77.05	159.72	1.309	63.9487	-20.7170	52	72.1
Nsub2-03	172.0	88.0	-153.94	-144.81	1.233	63.9174	-20.6849	108	72.4
Nsub2-04	189.0	90.0	176.28	146.35	0.739	63.9167	-20.7074	254	32.7
Nsub2-3-5-01	25.0	89.0	-107.77	-102.94	1.055	63.9452	-20.6969	37	29.9
Nsub2-3-5-02	356.0	89.0	-169.07	-164.13	0.804	63.9480	-20.7025	53	73.8
Nsub2-3-5-03	192.0	89.0	-162.04	-161.12	0.717	63.9477	-20.7095	35	46.6
Nsub2-3-5-04	35.0	89.0	-74.72	-85.55	0.959	63.9428	-20.6864	17	41.1
Nsub2-3-5-05	36.0	87.0	-63.37	-32.45	0.962	63.9295	-20.7046	81	83.5
Nsub2-3-5-06	20.0	81.0	-126.31	-117.90	1.187	63.9329	-20.6875	24	27.0
Nsub2-3-5-07	236.0	90.0	-2.01	2.16	0.555	63.9183	-20.7005	74	14.8
Nsub2-3-5-08	4.0	89.0	-161.77	-173.15	0.685	63.9177	-20.7004	171	21.4
Nsub2-3-5-09	188.0	90.0	-177.27	172.62	0.373	63.9218	-20.7006	70	18.1
Nsub4-04	198.0	90.0	178.56	-175.67	0.306	63.9418	-20.6884	26	11.4
Nsub4-5-02	3.0	74.0	178.03	171.19	4.187	64.0185	-20.7083	167	123.1
Nsub4-5-04	359.0	77.0	-156.81	-153.19	3.290	63.9892	-20.7249	35	93.5
Nsub4-5-05	1.0	85.0	-165.15	-175.18	3.371	63.9824	-20.7049	497	155.6
Nsub4-5-07	352.0	79.0	160.50	159.15	3.137	64.0498	-20.7053	74	214.0
Nsub4-5-10	177.0	89.0	-169.09	-172.21	4.928	63.9453	-20.7031	1162	138.4
Nsub5-06	8.0	89.0	-128.24	-121.21	0.322	63.9878	-20.6752	16	3.2

Table A.5. *Fault parameters for mapped fault segments on the Holt fault (J-17) and the Kvíarholt fault (box O).*

Fault segment	φ (°)	δ (°)	λ_ave (°)	λ_wav (°)	Length (km)	X (°E)	Y (°N)	#events	rms (m)
Osub1-02	14.0	88.0	-173.52	-170.47	1.690	64.0177	-20.3521	218	116.2
Osub1-03	184.0	90.0	151.05	160.20	0.674	64.0128	-20.3369	46	27.9
Osub1-04	200.0	89.0	160.19	163.02	0.386	64.0103	-20.3341	22	22.9
Osub1-05	115.0	88.0	8.45	-7.79	0.743	64.0241	-20.3119	29	67.8
Osub1-06	162.0	90.0	-169.77	165.12	0.324	64.0266	-20.3098	17	45.8
Osub1-07	19.0	89.0	-154.68	165.88	2.547	64.0142	-20.3430	218	97.0
Osub1-08	155.0	90.0	166.24	-174.91	0.328	64.0367	-20.3545	11	22.2
Osub1-10	174.0	90.0	145.34	175.05	4.290	64.0177	-20.3463	679	312.8
Osub2-03	226.0	81.0	-69.92	-75.06	0.212	63.9601	-20.3331	15	19.1
Osub2-11	192.0	90.0	-150.98	170.36	3.384	63.9764	-20.3534	569	102.0
Osub3-04	201.0	90.0	-164.43	-164.18	1.420	63.9169	-20.3796	79	58.9
Osub3-05	195.0	88.0	-148.80	173.72	0.424	63.9458	-20.3986	32	16.9
Osub3-06	319.0	89.0	5.39	137.77	2.369	63.9321	-20.3925	221	107.8
Osub3-07	342.0	89.0	108.30	152.22	0.350	63.9391	-20.4075	25	19.9
Osub3-08	349.0	89.0	161.81	167.26	0.345	63.9356	-20.4021	25	17.1
Osub3-09	14.0	89.0	157.70	154.89	0.711	63.9271	-20.3828	80	43.6
Osub3-10	167.0	90.0	134.76	136.58	0.445	63.9338	-20.3784	12	25.1
Osub3-11	169.0	88.0	63.71	83.70	0.951	63.9320	-20.3876	25	39.2
Osub3-12	196.0	81.0	-128.43	-168.67	1.195	63.9261	-20.3643	83	37.4
Osub3-13	181.0	89.0	-171.98	15.16	1.555	63.9377	-20.3562	58	52.9
Osub3-14	194.0	83.0	-156.60	-177.96	2.760	63.9306	-20.3618	73	61.7
Osub4-03	6.0	75.0	-151.52	-158.01	11.877	63.9768	-20.3518	1188	280.6
Osub4-04	162.0	87.0	172.21	165.06	0.801	63.9270	-20.3701	36	56.5
Osub4-05	9.0	80.0	-153.08	-139.01	4.074	63.9486	-20.3545	172	147.1
Osub4-06	199.0	88.0	-160.06	-173.13	2.365	63.9747	-20.3509	290	106.1
Osub4-07	23.0	89.0	-120.09	-131.04	0.737	63.9867	-20.3470	60	64.9
Osub4-08	23.0	89.0	-129.28	-117.16	1.530	63.9917	-20.3510	103	119.5
Osub4-09	178.0	90.0	-171.90	-161.03	1.032	64.0045	-20.3418	38	43.6
Osub4-10	159.0	87.0	176.18	-165.68	0.710	64.0064	-20.3492	36	56.8
Osub4-11	166.0	90.0	-177.63	-153.02	0.372	64.0147	-20.3531	14	33.2
Osub4-12	215.0	90.0	39.00	128.58	0.327	64.0133	-20.3459	19	16.0
Osub4-13	357.0	87.0	179.57	-175.56	0.291	64.0116	-20.3397	18	27.0
Osub5-03	187.0	88.0	175.75	-172.31	7.023	63.9419	-20.4368	407	92.6

APPENDIX B –Rake angle distribution

Distribution of rake angles on all mapped faults/clusters plotted in orange on rose diagrams. Black line shows direction of the component of average slip vector which lies in the common fault plane (defined by the event distribution), and grey line shows the component of weighted average slip vector which lies in the plane (weighted with M_0).
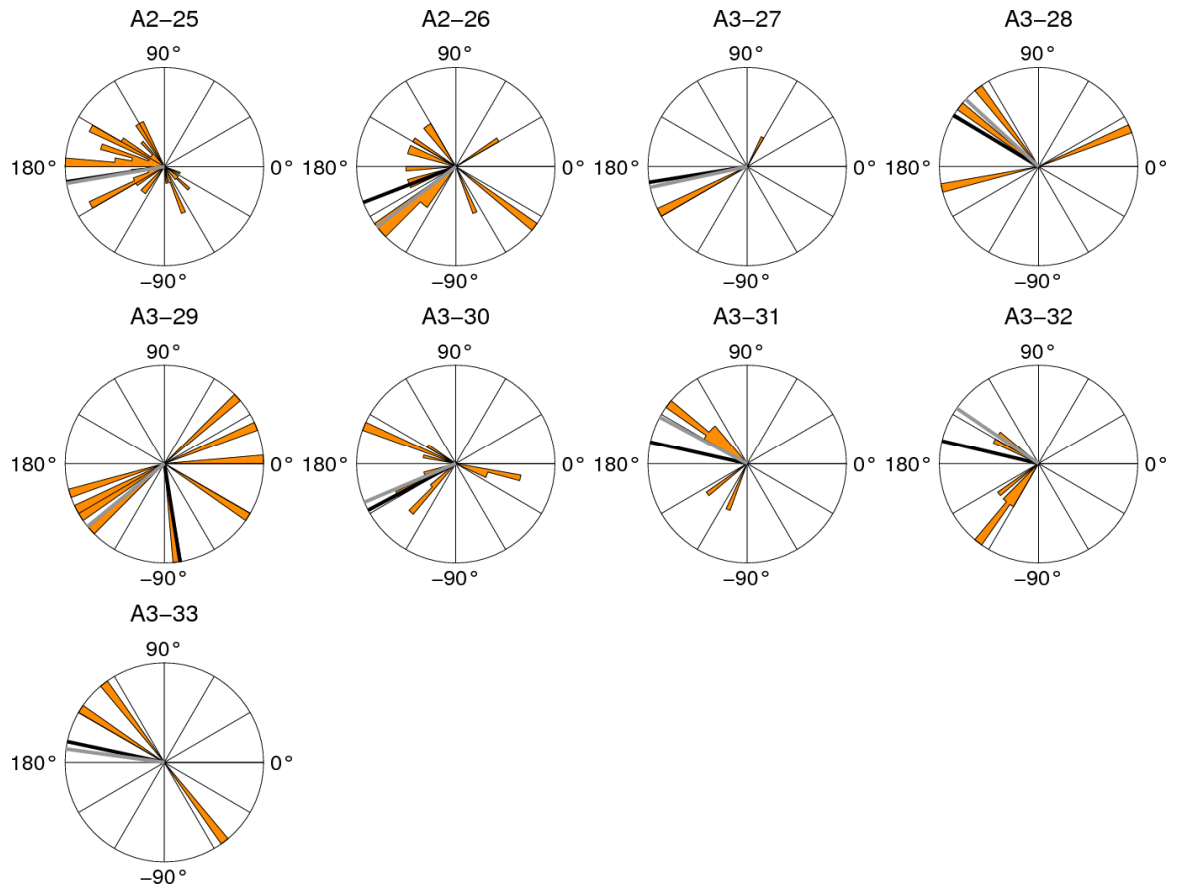
A2–01 A2–02 A2–03 A1–04
A1–05 A2–06 A2–07 A1–08
A1–09 A1–10 A3–11 A1–12
A1–13 A1–14 A1–15 A1–16
A2–17 A2–18 A2–19 A2–20
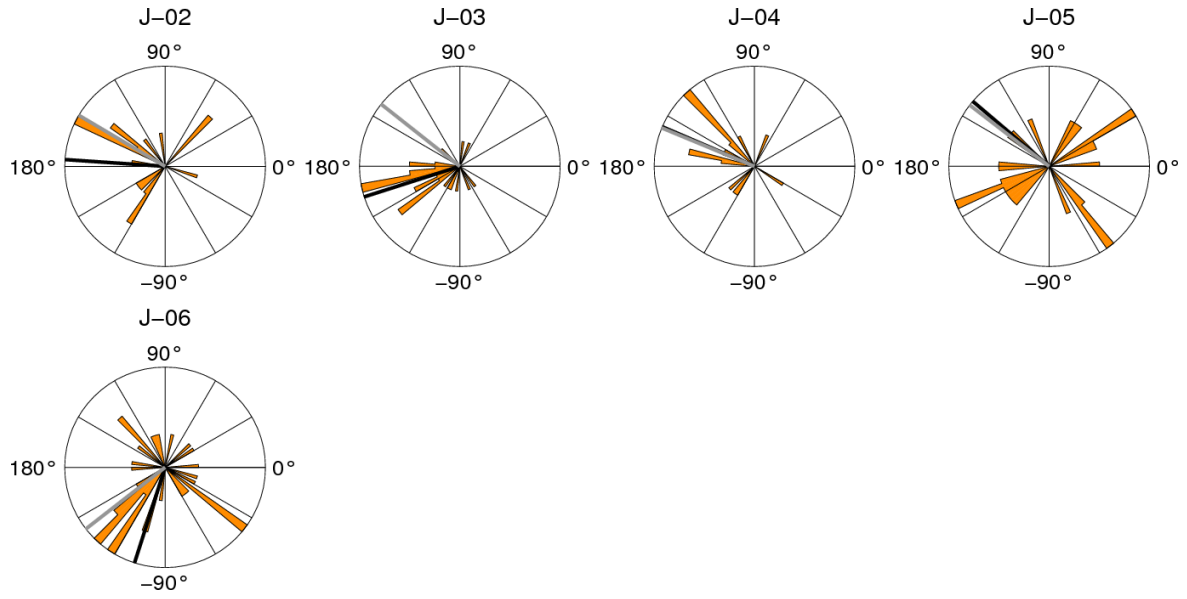A2–21 A2–22 A2–23 A2–24

88

Figure B.1. *This and previous page: Rake distribution for mapped faults/clusters in box A (A1, A2, A3).*
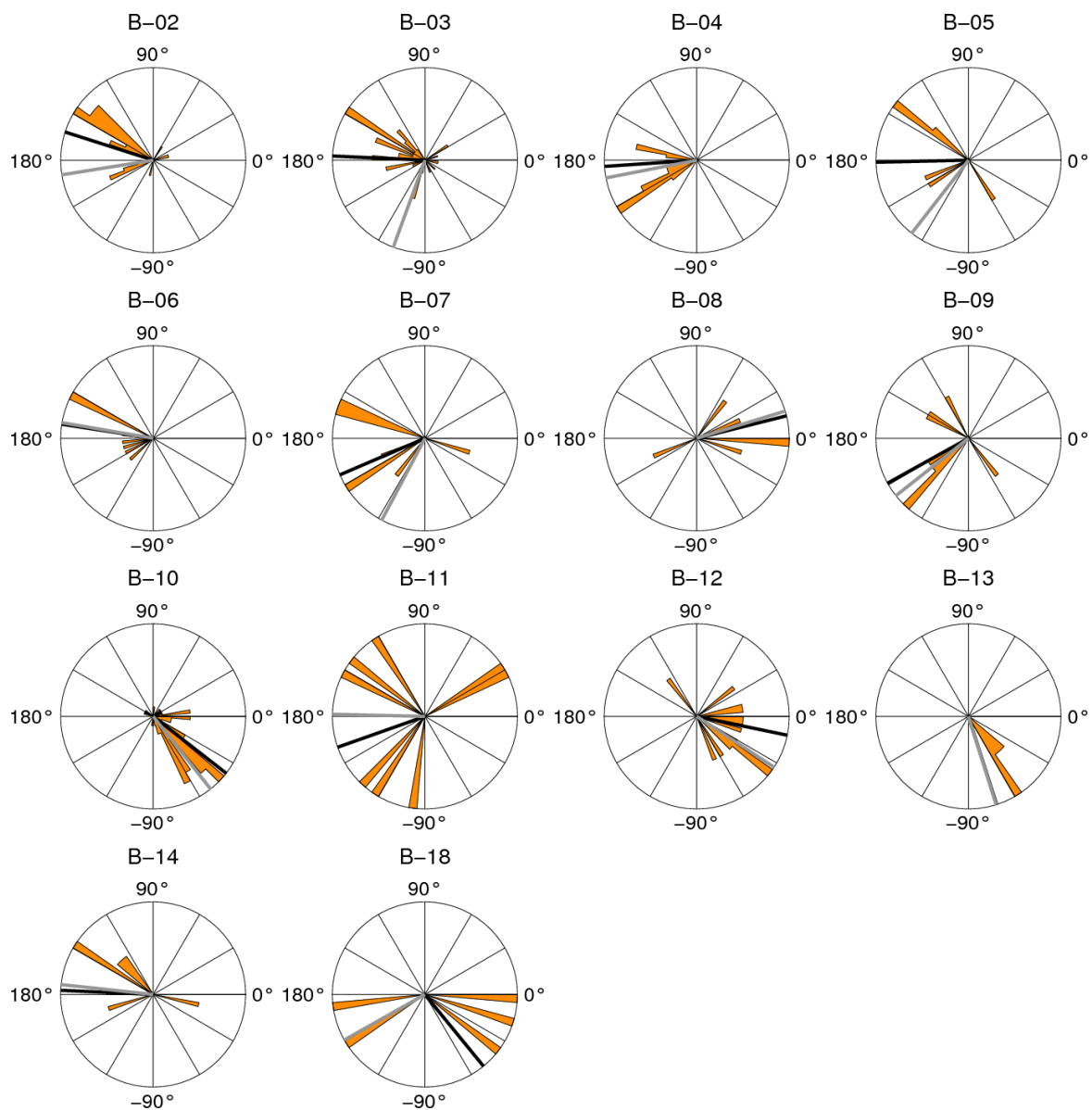
Figure B.2. *Rake distribution for mapped faults/clusters in box B, Fagradalsfjall-W.*
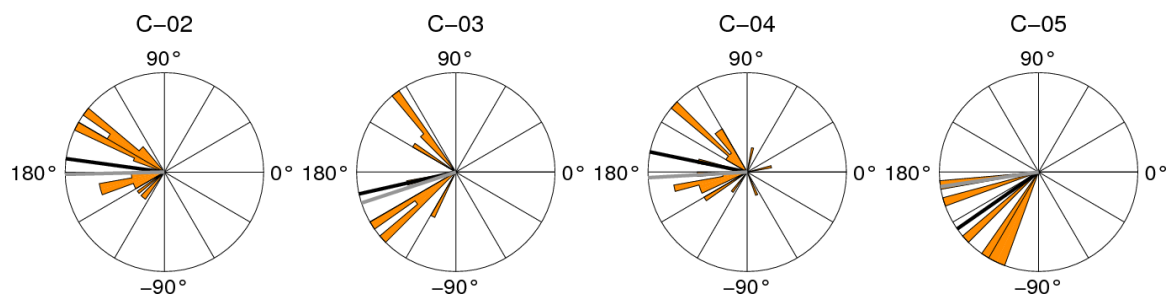
Figure B.3. *Rake distribution for mapped faults/clusters in box C, Fagdaralsfjall-E.*
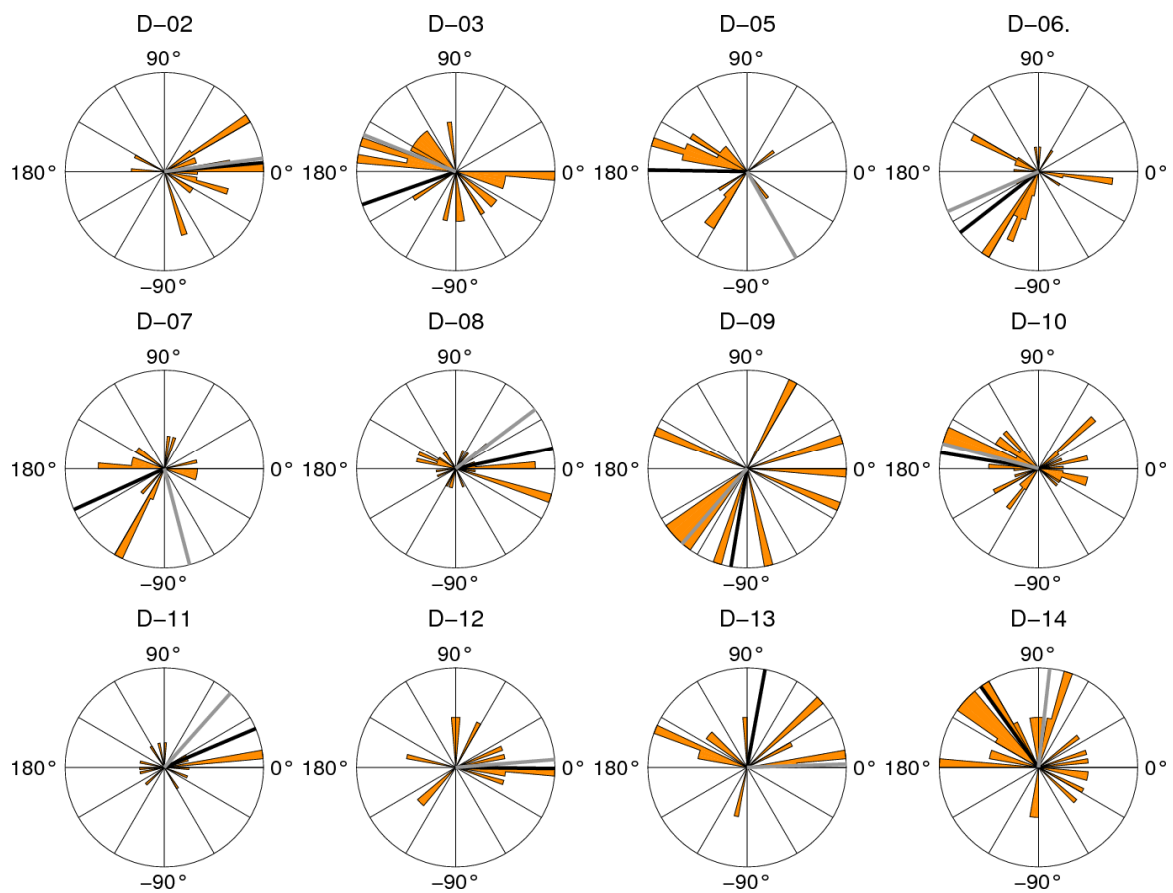
Figure B.4. *Rake distribution for mapped faults/clusters in box D, Kleifarvatn.*
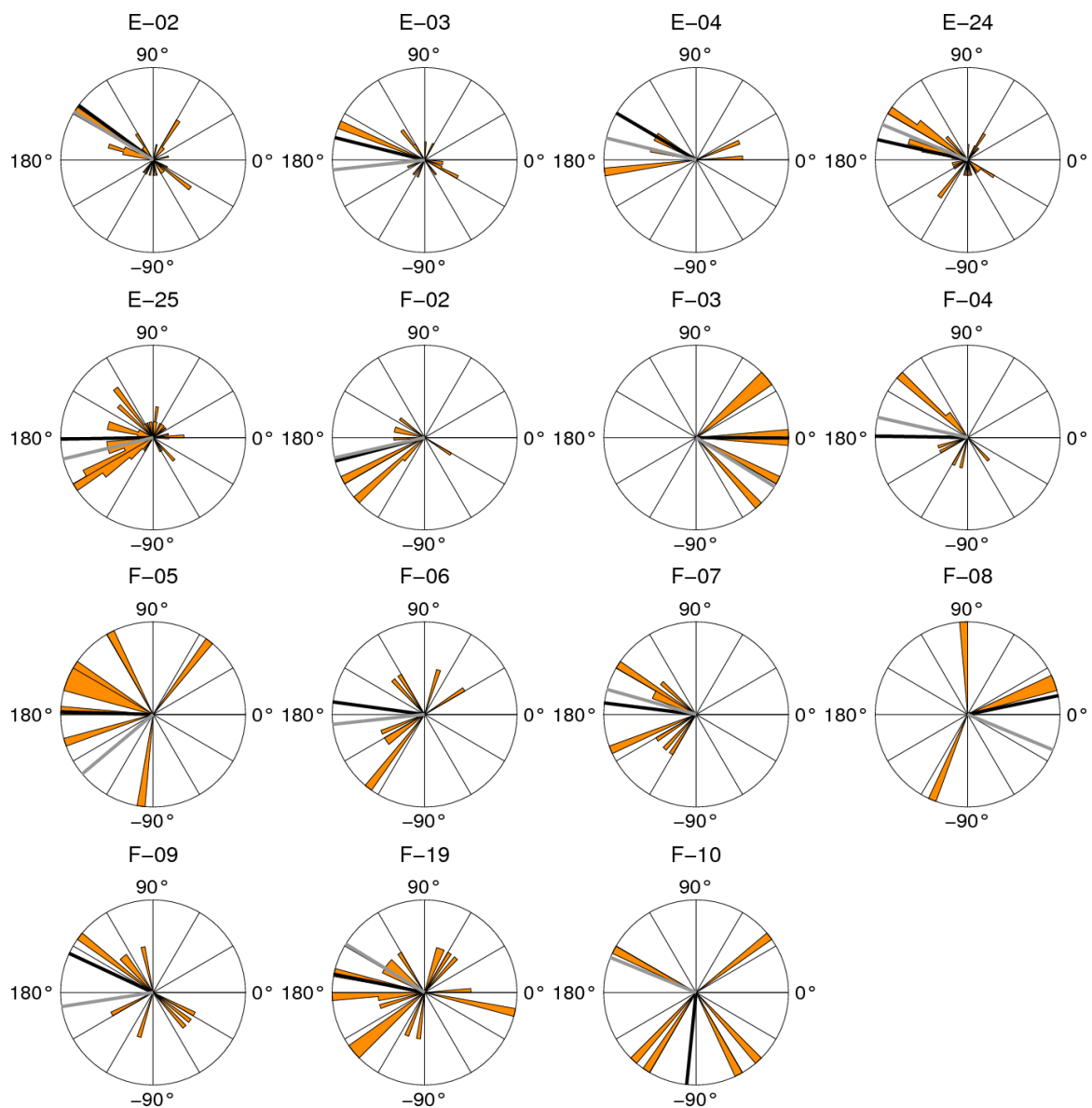
Figure B.5. *Rake distribution for mapped faults/clusters in boxes E and F, Brennisteinsfjöll-Bláfjöll.*
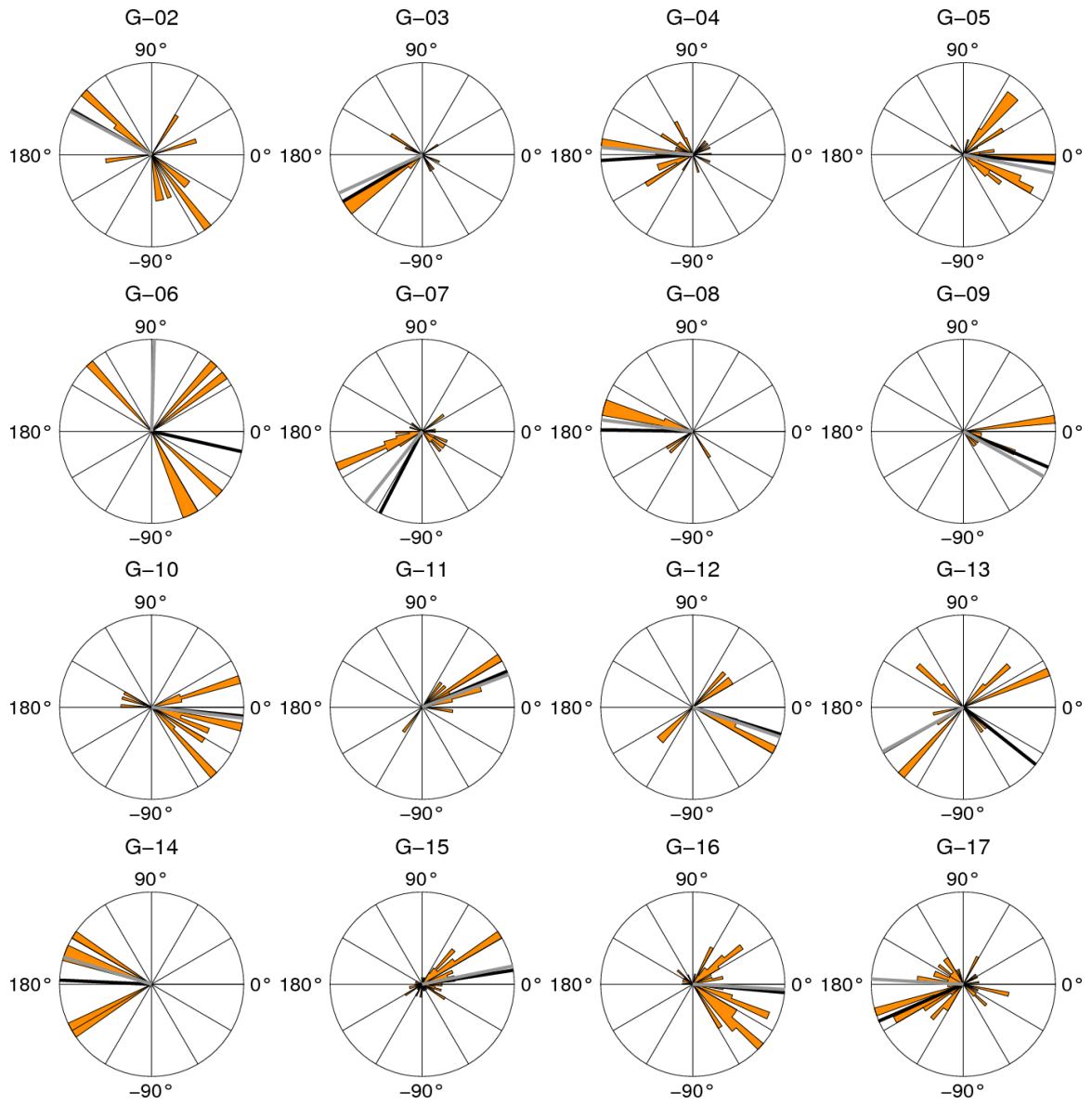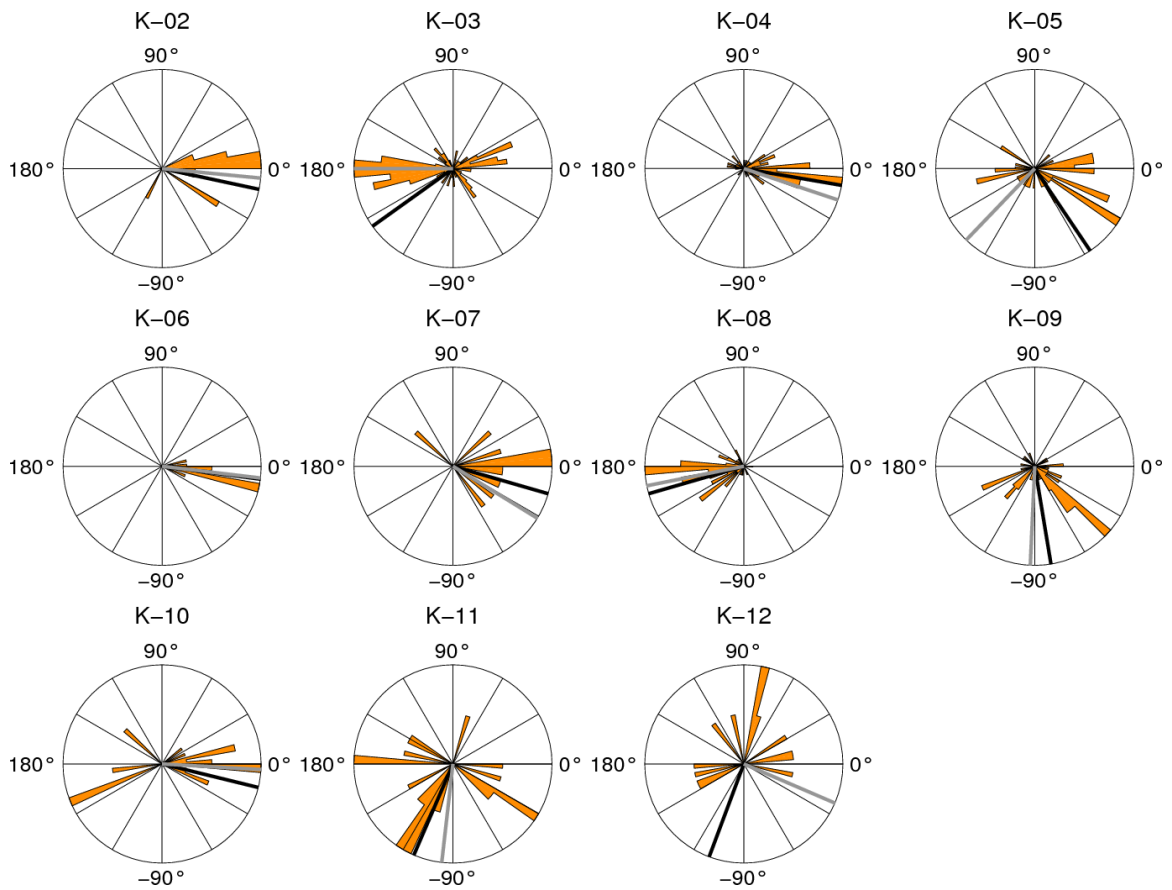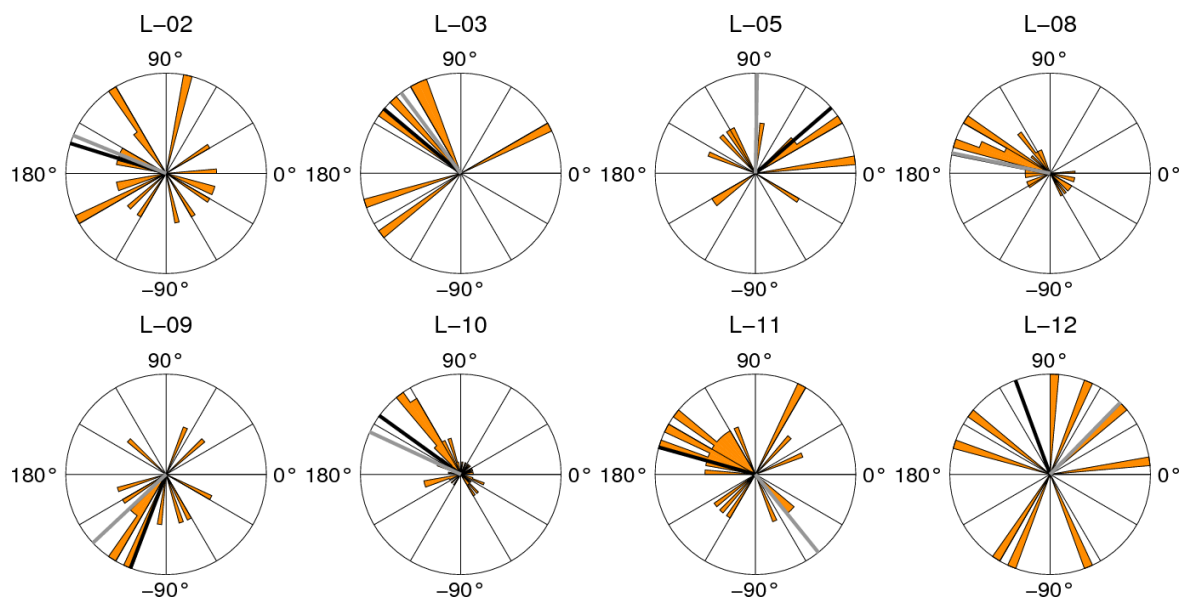
Figure B.6. *Rake distribution for mapped faults/clusters in box G, Ölfus.*
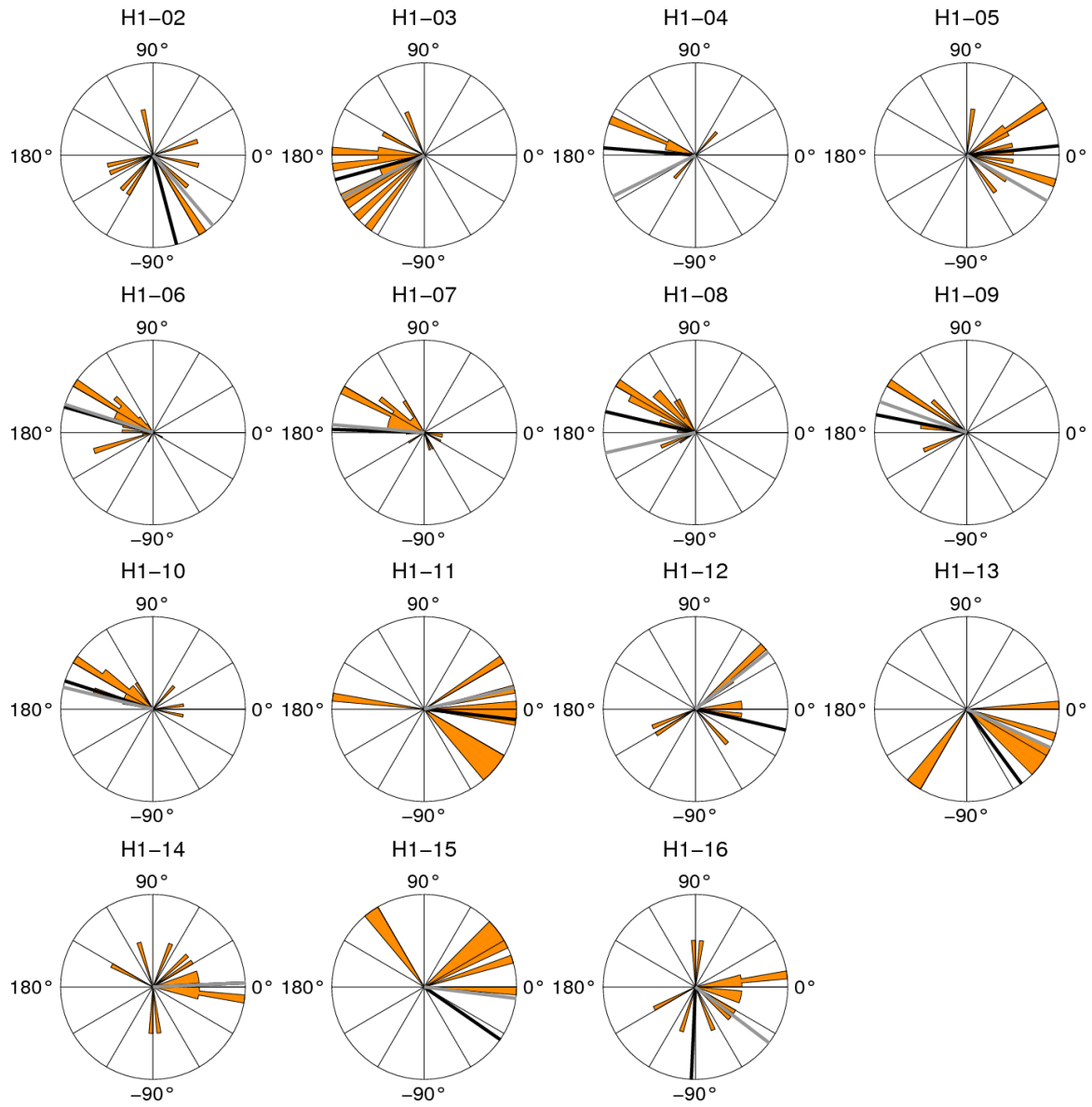
Figure B.7. *Rake distribution for mapped faults/clusters in box H, Hengill, active between January and May.*
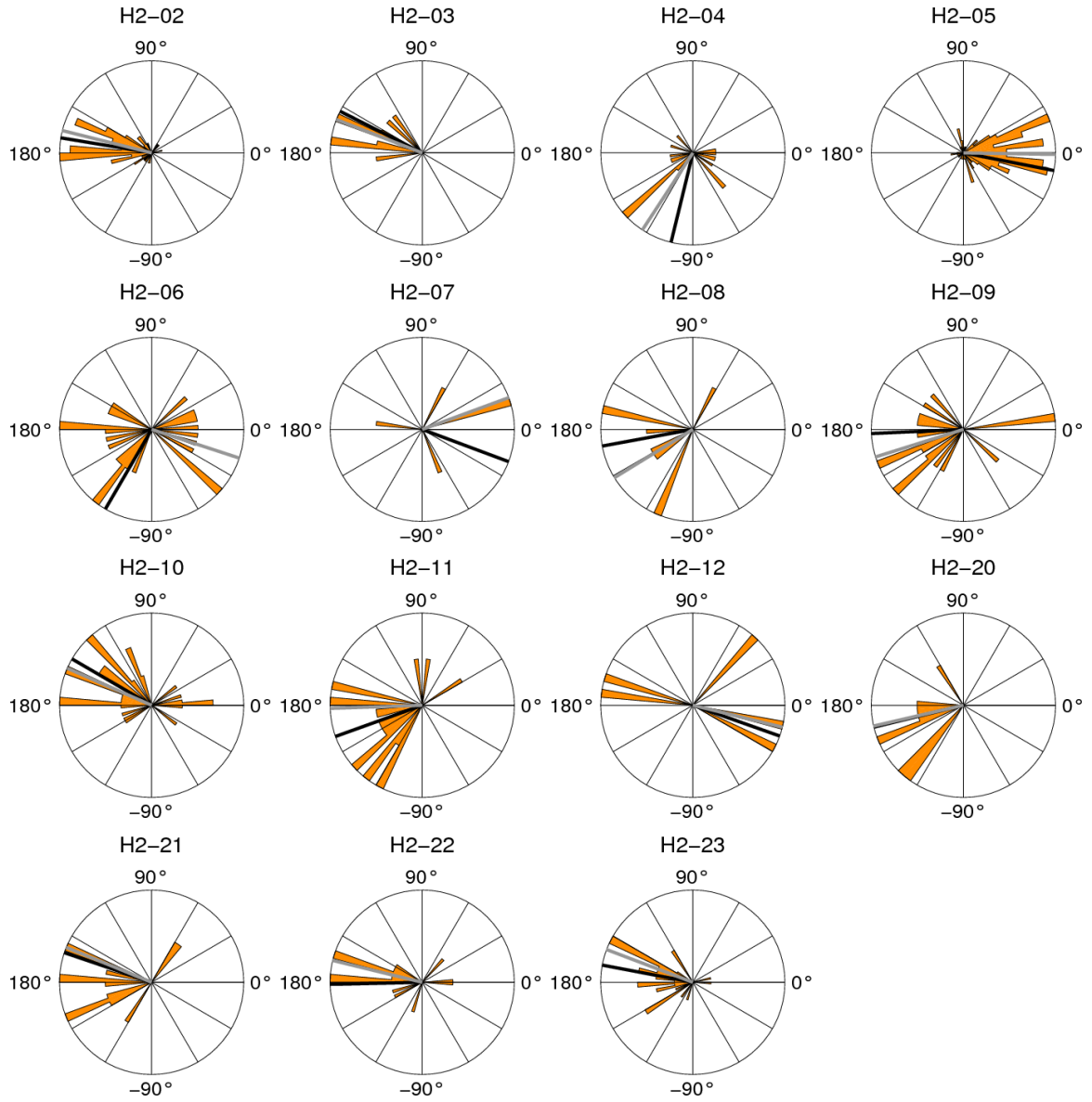
Figure B.8. *Rake distribution for mapped faults/clusters in box H, Hengill, active between June and December.*
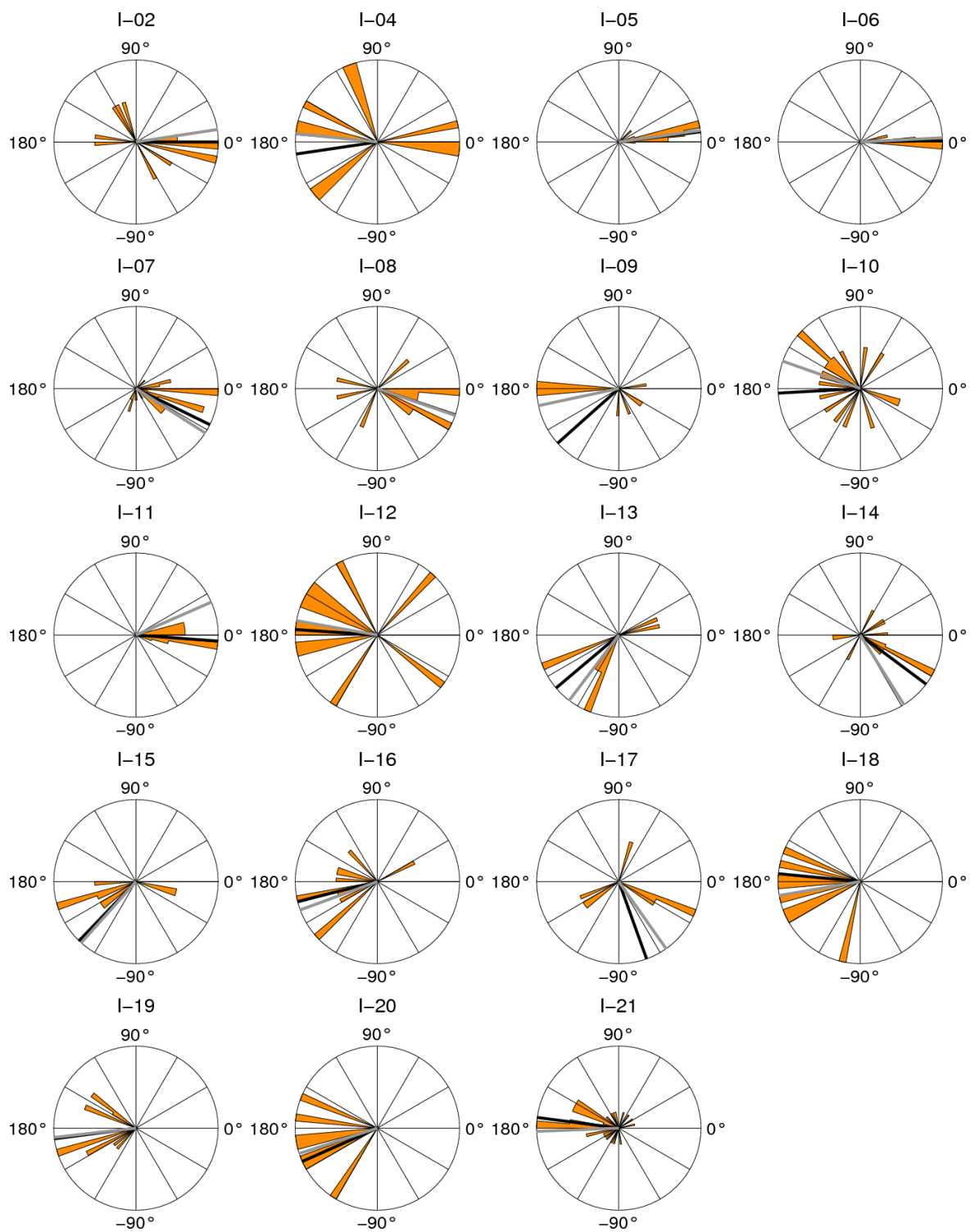
Figure B.9. *Rake distribution for mapped faults/clusters in box I, Flói.*

Figure B.10. *Rake distribution for mapped faults/clusters in box J, Hella.*

Figure B.11. *Rake distribution for mapped faults/clusters in box K, Hraungerði.*

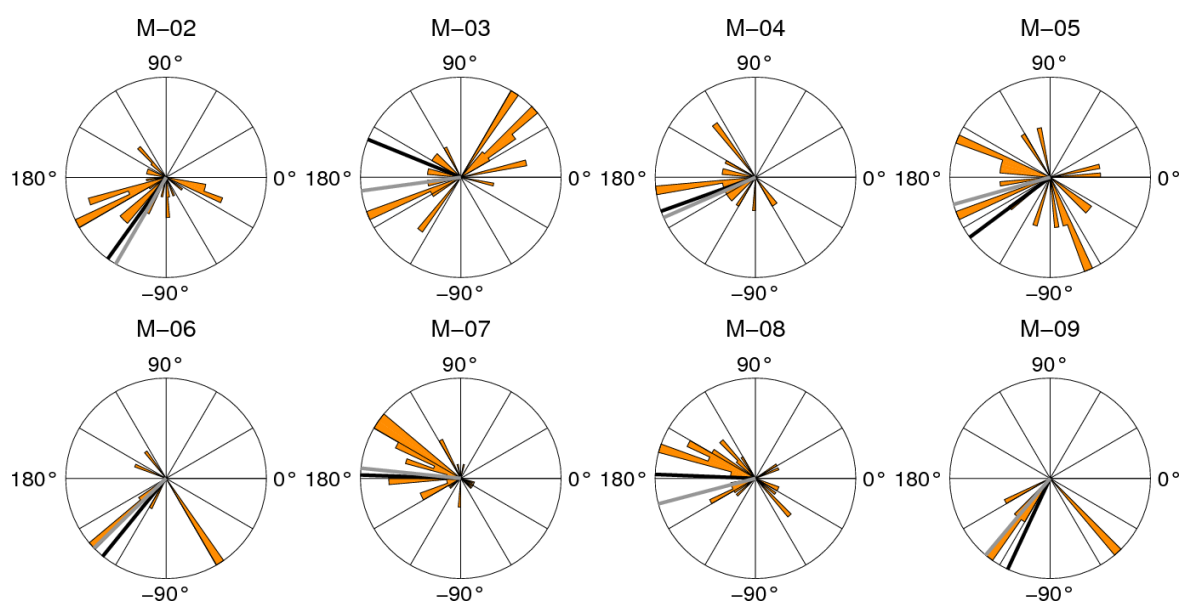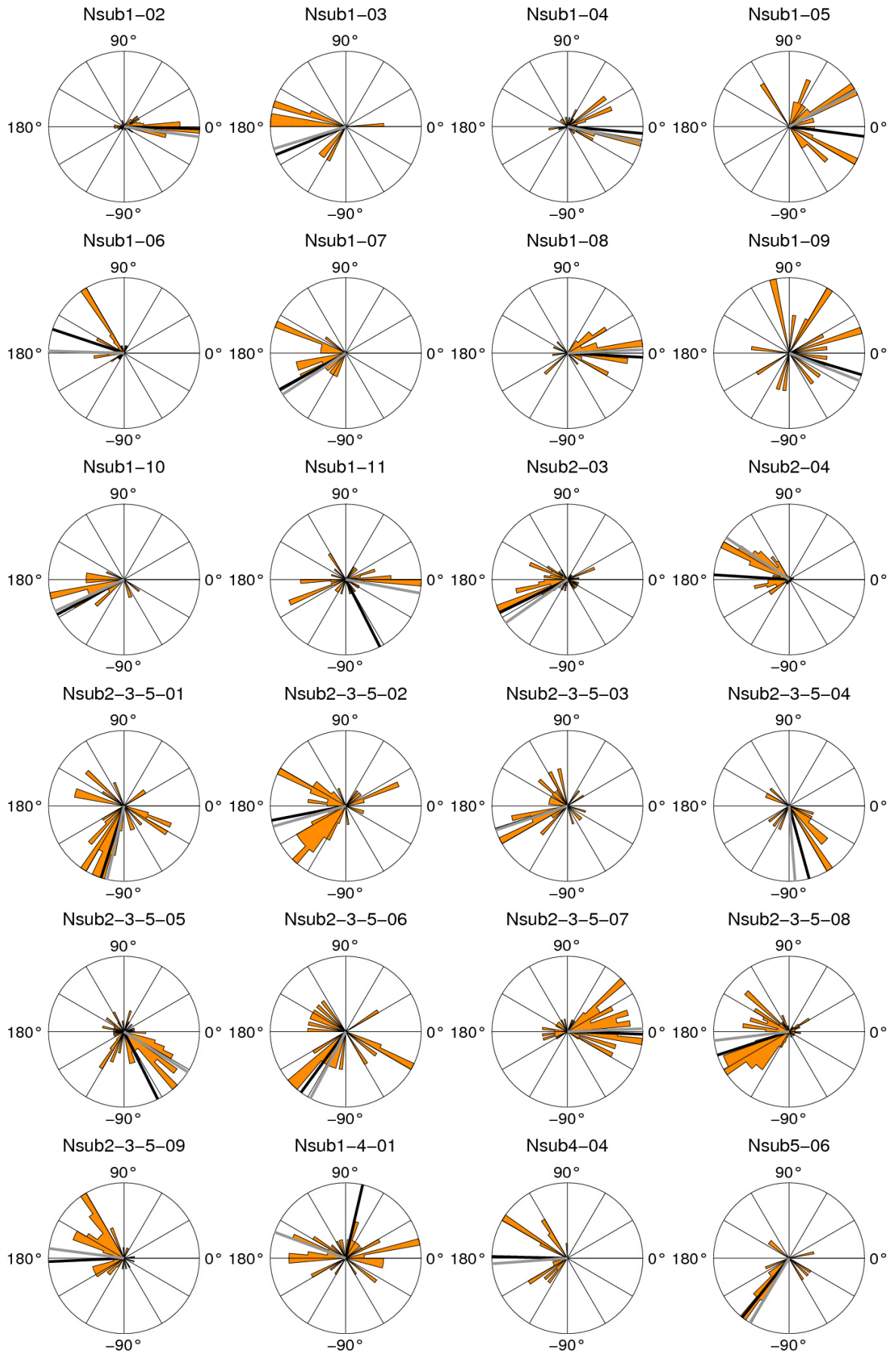**Figure B.12.** *Rake distribution for mapped faults/clusters in box L, Skeið.*

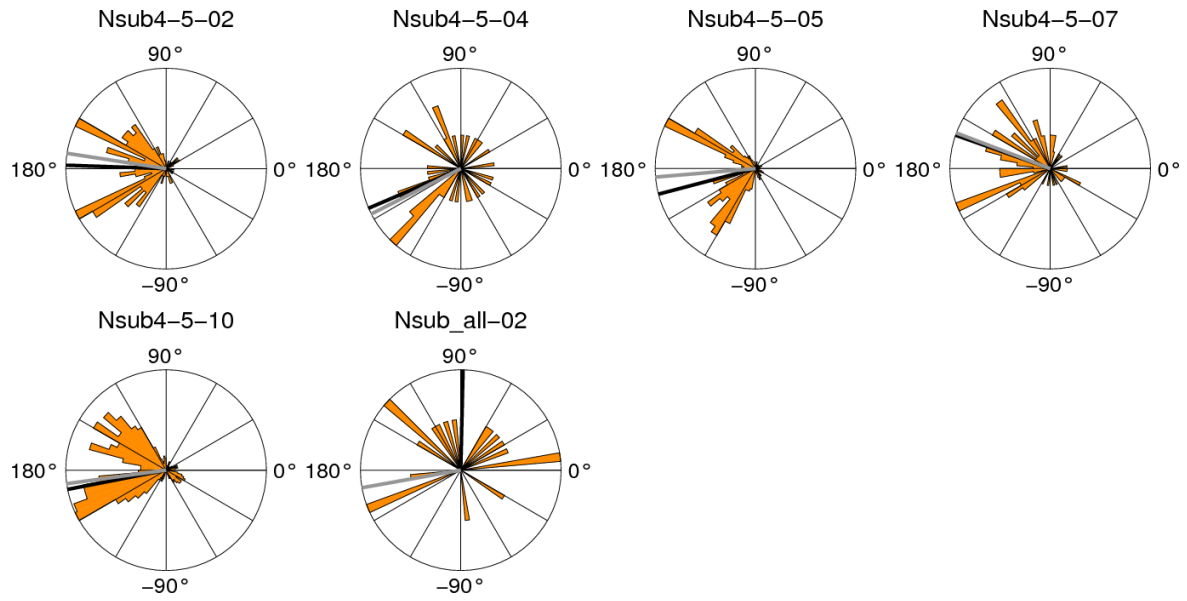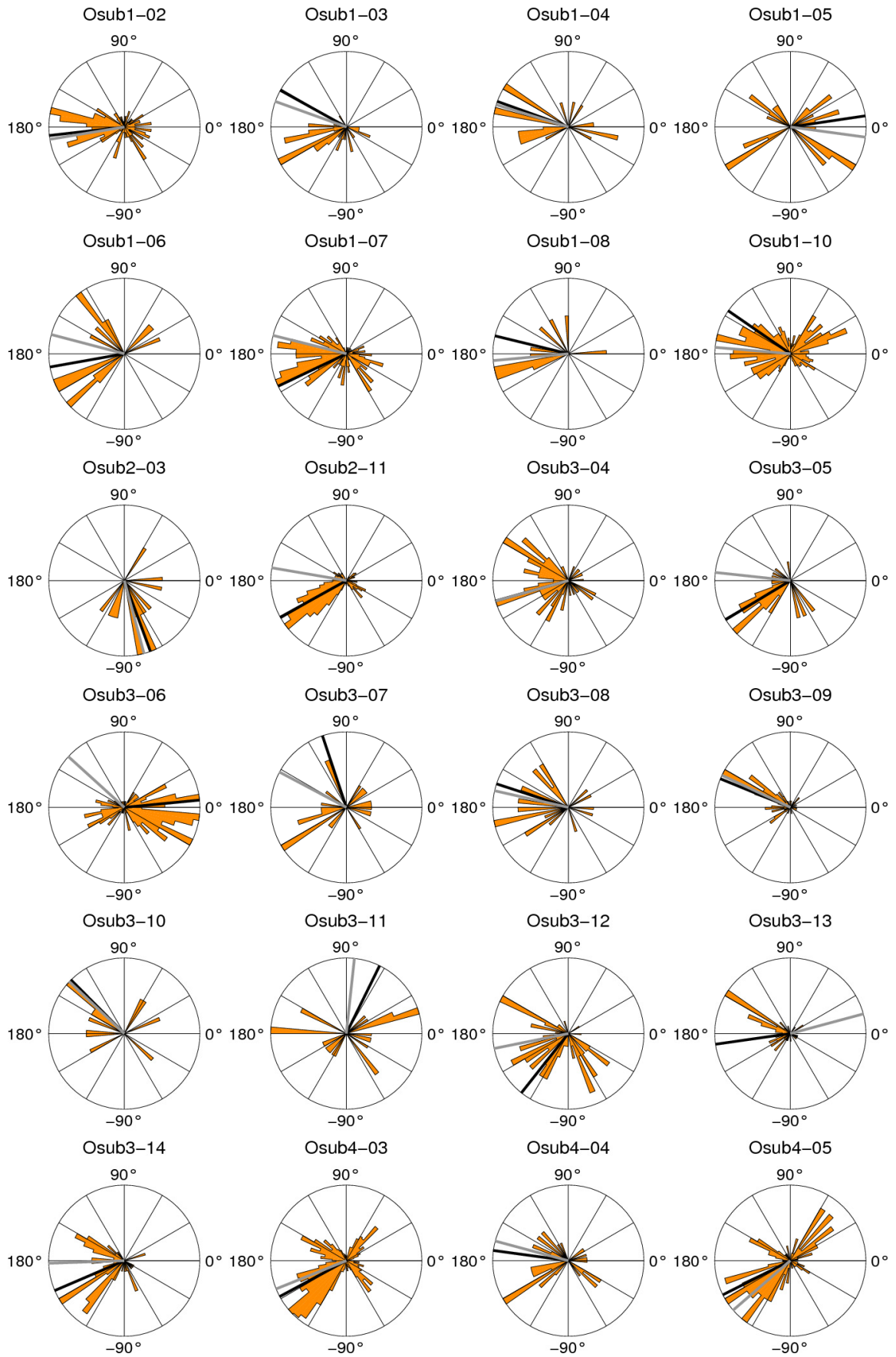**Figure B.13.** *Rake distribution for mapped faults/clusters in box M, Land.*

Figure B.14. *This and previous page: Rake distribution for mapped faults/clusters in box N, Hestvatn fault. Division of fault is as follows: sub1-conjugate faults west of main fault (west of 20.714°W, north of 63.913 and south of 63.97); sub2- southern part (south of 63.926 and north of 63.913); sub3- southernmost part (south of 63.913); sub4- events above the bottom (north of 63.926) ; sub5- bottom of fault (north of 63.926).*
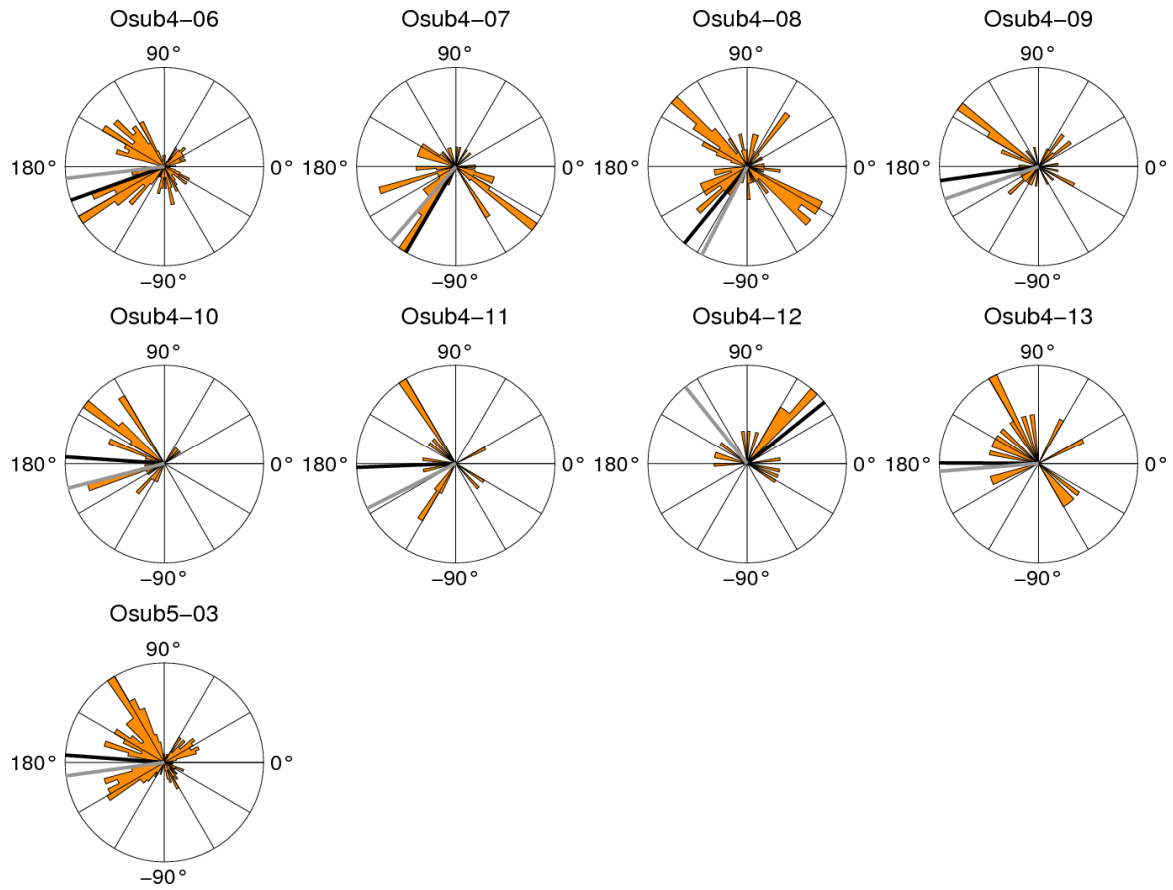
Figure B.15. *This and previous page: Rake distribution for mapped faults/clusters in box O, Holt-fault. Division of fault is as follows: sub1-north patch (north of 63.9975); sub2- centre patch; sub3- south patch (south of 63.95) ; sub4- bottom of fault (below 8.3 km depth); sub5- Kvíarholt fault.*

APPENDIX C –List of presentations, posters and reports

Hjaltadóttir, S., K. S. Vogfjörð and R. Slunga, 2003. Relative locations of earthquakes in SW-Iceland. Summer school on Tectonic-Magmatic Interaction, 31 August – 8 September, 2003, Geysir, South-Iceland, p.18, *Nordic Volcanological Institute report* 0303, Reykjavík, Iceland. (Poster.)

Hjaltadóttir, S. Mapping of subsurface faults in southwestern Iceland with the microearthquakes induced by the June 17 and June 21 earthquakes. *PREPARED mid-term meeting in Reykjavík*, 30-31 January 2004. (Presentation.)

Hjaltadóttir, S., 2004. Mapping of subsurface faults in SW-Iceland using relatively located events. Friday seminar at NORVOL, 23 April 2004. (Presentation.)

Hjaltadóttir, S., K. S. Vogfjörð, R. Slunga, 2004. Upptakagreinig smáskjálfta og kortlagning sprungna á Suðvesturlandi. *Geoscience Society of Iceland, Spring meeting 2004,* p. 54. (Presentation.)

Hjaltadóttir, S., K. S. Vogfjörð, R. Slunga, R. Stefánsson, and P. Einarsson, 2004. Upptakagreining smáskjálfta og kortlagning sprunguflata á Suðvesturlandi. *Raunvísindaþing í Háskóla Íslands*, 16-17 April 2004. (Poster.)

Hjaltadóttir, S., 2004. Upptakagreining smáskjálfta og kortlagning sprunguflata á Suðvesturlandi. Rannsóknadagur í HÍ 12. nóvember 2004. (Poster, same as above and a text published in *Stúdentablaðið, November 2004.*)

Hjaltadóttir, S., K. S. Vogfjörð, 2005. Subsurface fault mapping in Southwest Iceland by relative location of aftershocks of the June 2000 earthquakes. *Icelandic Meteorological Office, Rit* 21. (Report.)

Hjaltadottir, S., K. S. Vogfjord, R. Slunga, 2005. Mapping Subsurface Faults in Southwest Iceland Using Relatively Located Microearthquakes. *Geophysical Research Abstracts,* 7, A-06664. (Poster.)

Hjaltadóttir, S, 2005. Brotfletir stórskjálfta kortlagðir með eftirskjálftum. Published in: *Rannís-blaðið*, fimmtudagur 20. október 2005. (Newspaper article.)

Hjaltadóttir, S., K. S. Vogfjörð, Þ. Árnadóttir, and P. Einarsson, 2005. A model of the release of the two June 2000 earthquakes based on all observations. Icelandic Meteorological Office Report, 05020, VÍ-ES-09. (Report.)

Hjaltadóttir, S., K. S. Vogfjörð, and R. Slunga, 2005. Fault-Patterns in the South Iceland Seismic Zone Revealed by Double-Difference Mapping of Earthquakes. Eos Trans. *AGU, 86 (52), Fall Meet. Suppl., Abstract* S32B-03. (Presentation.)

Hjaltadóttir, S., K. S. Vogfjörð, and R. Slunga, 2006. Subsurface Faults in Southwestern Iceland Mapped by Relatively Located Microearthquakes. An Overview. Nordic Seminar on Detection Seismology, Nesjavellir, 21 August 2006. (Presentation.)

Hjaltadóttir, S., K. S. Vogfjörð, G. B. Guðmundsson, M. J. Roberts, and S. S. Jakobsdóttir, 2008. Notkun endurstaðsettra smáskjálfta til kortlagningar (e. The use of relocated microearthquakes for mapping). *Geoscience Society of Iceland, Fall meeting*, 27 November 2008. (Presentation.)